НАЦІОНАЛЬНА АКАДЕМІЯ НАУК УКРАЇНИ
ІНСТИТУТ ЗАГАЛЬНОЇ ТА НЕОРГАНІЧНОЇ ХІМІЇ імені В. І. ВЕРНАДСЬКОГО
КИЇВСЬКИЙ НАЦІОНАЛЬНИЙ УНІВЕРСИТЕТ імені ТАРАСА ШЕВЧЕНКА

УКРАЇНСЬКИЙ ХІМІЧНИЙ ЖУРНАЛ

№ 06
Том 87 / Vol. 87
2021
https://ucj.org.ua

UKRAINIAN CHEMISTRY JOURNAL

Зміст

ФІЗИЧНА ХІМІЯ

В. С. Фарафонов, О. В. Лебідь, М. О. Мчедлов-Петросян
КОНТИНУАЛЬНО-ЕЛЕКТРОСТАТИЧНЕ ДОСЛІДЖЕННЯ ЙОННИХ МІЦЕЛ ІЗ ВИКОРИСТАННЯМ АТОМІСТИЧНИХ МОДЕЛЕЙ 55

І. А. Новоселова, С. В. Кулешов, А. О. Омельчук, В. М. Биков, О. М. Фесенко
ОСОБЛИВОСТІ ЕЛЕКТРОВІДНОВЛЕННЯ Li_2CO_3 В ЕКВІМОЛЯРНОМУ РОЗПЛАВІ ХЛОРИДІВ НАТРІЮ ТА КАЛІЮ 70

В. А. Діамант
СУЧАСНІ МЕТОДИ ДОСЛІДЖЕННЯ ФІЗИКО-ХІМІЧНИХ І ЕЛЕКТРОХІМІЧНИХ ВЛАСТИВОСТЕЙ ЕЛЕКТРОЛІТІВ У ЛІТІЙ-ЙОННИХ АКУМУЛЯТОРАХ ТА ГІБРИДНИХ СУПЕРКОНДЕНСАТОРАХ. 82

НЕОРГАНІЧНА ХІМІЯ

О. С. Бережницька, А. Е. Горбенко, О. О. Роговцов, С. С. Смола, Я. В. Федоров, О. Е. Чигиринець, О. К. Трунова
КООРДИНАЦІЙНІ СПОЛУКИ Gd^{3+} та Dy^{3+} З ДЕЯКИМИ β-ДИКЕТОНАМИ. 97

Contents

PHYSICAL CHEMISTRY

V. S. Farafonov, A. V. Lebed, N. O. Mchedlov-Petrossyan
CONTINUUM ELECTROSTATICS INVESTIGATION OF IONIC MICELLES USING ATOMISTIC MODELS 55

I. A. Novoselova, S. V. Kuleshov, A. O. Omel'chuk, V. M. Bykov, O. M. Fesenko
PECULIARITIES OF ELECTROREDUCTION OF Li_2CO_3 IN THE EQUIMOLAR MELT OF SODIUM AND POTASSIUM CHLORIDES 70

V. A. Diamant
MODERN RESEARCH METHODS OF PHYSICOCHEMICAL AND ELECTRO CHEMICAL PROPERTIES OF ELECTROLYTES FOR Li-ION BATTERIES AND HYBRID SUPERCAPACITIES 82

INORGANIC CHEMISTRY

O. S. Berezhnytska, A. E. Horbenko, O. O. Rohovtsov, S. S. Smola, Ya. V. Fedorov, O. E. Chygyrynets, O. K. Trunova
THE COORDINATION COMPOUNDS Gd (III) AND Dy(III) WITH SOME β-DIKETONES . . 97

ISSN 2708-129X. Укр. хім. журн., 2020

УДК 544.77.022.532+537.213+537.222.1+537.226.1+004.942 doi: 10.33609/2708-129X.87.06.2021.55-69

CONTINUUM ELECTROSTATICS INVESTIGATION OF IONIC MICELLES USING ATOMISTIC MODELS

V. S. Farafonov,* A. V. Lebed, N. O. Mchedlov-Petrossyan

V. N. Karazin Kharkiv National University, Svobody sq., 4, Kharkiv, 61022, Ukraine
**e-mail: farafonov@karazin.ua*

The key parameter related to the structure of the electric double layer of ionic surfactant micelles – electrostatic potential – is considered. A brief overview of experimental methods and theoretical models for estimating electrostatic potential is given. The calculating method for the electrostatic potential based on a numerical solution of the Poisson-Boltzmann equation using an atomistic model of anionic surfactant micelle is proposed. The parameters necessary for the construction of atomistic models are obtained from molecular dynamic modeling. The electrostatic potentials for the micelles of sodium dodecyl sulfate and cetyltrimethylammonium bromide at different ionic strengths were calculated by this method. The results are discussed in comparison with the values calculated in the simplified model, the Ohshima – Healy – White equation.

Keywords: surfactant micelle, Stern layer, electrostatic potential, Poisson – Boltzmann equation, solvent-accessible surface.

INTRODUCTION. Micelles of colloidal surfactants are widely used in different fields of chemistry and related sciences and technologies [1–3]. Aqueous micellar solutions are almost transparent and thermodynamically stable (*i.e.*, reversible) liquid systems [3–5]. They may be considered as the most simple and at the same time most important and unique representatives of the so-called organized solutions [6, 7]. Hereafter, we shall consider ionic surfactants, which are diphilic molecules consisting of a hydrophobic portion and ionic group. In fact, they are colloidal electrolytes with a hydrocarbon chain containing from 8 to 18 carbon atoms.

Micelles of a given colloidal surfactant are formed in aqueous solutions upon reaching a certain concentration, the so-called critical micelle concentration (CMC) and at a temperature equal or above the so-called Krafft point. The driving force of micellization in water is the hydrophobic interaction [3–5]. The hydrophilic parts of the surfactants are directed towards the bulk (aqueous) phase, while the hydrophobic tails form the internal hydrocarbon core. According to the generally accepted model, these surfactant aggregates are highly porous, highly hydrated, disordered clusters in a state of dynamic equilibrium with monomers in the bulk phase. In the concentration range

about the CMC, the micelles are several nm-sized and practically sphere-shaped.

Although many models of the structure of micelles of ionic surfactants can be found in the literature, they all agree on the main point. Namely, an electric double layer (EDL) appears at the micelle-water interface. The ionic head groups form the inner layer characterized by surface electrostatic potential Ψ_0. It attracts the counterions from solution, which form the outer layer. Different approaches were proposed for its description, starting from the Goüy – Chapman model, where the counterions are considered size-less and adopting Boltzmann distribution of concentration immediately after the inner layer, and then the Stern model, where some portion of counterions is assumed to adsorb strongly and form a thin dense layer (subsequently called Stern layer), while Boltzmann distribution starts from its outer boundary. The thickness of the Stern layer is usually denoted as δ, and the electrostatic potential at its boundary is hence denoted as Ψ_δ. Various departures from this model were developed beginning with the classical papers by Stigter [8, 9]. For the counterions in the Stern layer, mobile and localized adsorption models were considered by Rathman and Scamehorn [10]. Treating micelle formation by small system thermodynamics, Gilányi suggested a diffuse monolayer structure instead of the idealized Goüy – Chapman model [11]. This listing can be continued up to the latest works utilizing molecular dynamics (MD) simulations [12–14].

In many cases, the electrostatic potential is considered as a key parameter governing the properties of the micellar solutions of ionic surfactants, affecting their behavior in photophysical and analytical processes, chromatography, shifting of equilibrium states and acceleration of a variety of reactions, binding various compounds, in synthesis of nanoparticles, *etc*. [1–4,7,15]. Consequently, there are many approaches to determine its value for ionic micelles.

Among the experimental methods, the most popular and universal one is based on the application of colored or fluorescent acid-base indicators [3,15–20]. There, Ψ is determined using the so-called apparent dissociation constant, K_a^{app}, of the indicator bound to the micelle and the so-called intrinsic constant, K_a^i, Eq. 1.,

$$\Psi = \frac{RT\ln 10}{F} \times (\mathrm{p}K_a^i - \mathrm{p}K_a^{app}) \qquad (1)$$

Here R, T, F have their usual meanings.

The apparent constant is in fact a two-phase equilibrium constant because the pH value is determined in the bulk phase, whereas the acid-base couple of the indicator dye is located in the micellar palisade. As the $\mathrm{p}K_a^i$ value, the $\mathrm{p}K_a^{app}$ value of the same indicator in micelles of nonionic surfactant is usually used. Some more sophisticated assumptions to determine these values are also used [3, 15, 16, 19, 20]. A similar approach is based on using acid-base equilibria of stable free radicals and the electronic spin resonance method [21]. A method of monitoring the fluorescence changes along with electrostatic potential alterations was developed for membranes and vesicles [22]. Utilization of the small-angle neutron scattering method for determination of the surface electrical charge and potential of surfactant micelles is also reported [23].

Yet, all these experimental methods are based on the use of molecular probes, which makes their results depending on the chosen

probe. One of the reasons is the variation of the probe location in the micelle. In general, the probes are considered to be located within the Stern layer, which implies the Ψ in Eq. 1 should be somewhere between Ψ_0 and Ψ_δ. Another reason is the possibility of specific interactions between the probe and surfactant. In total, for sodium dodecyl sulfate (SDS) micelles the variation of Ψ, as found using Eq. 1, reaches about 200 mV [15].

This makes the demand for approaches that consider the sole micelles and, hence, are free from this issue. In this connection, the most relevant approach is the electrophoretic measurement of the electrokinetic (or ζ-) potential of colloid particles. No foreign probes are required, and the obtained ζ values characterize solely the particles and the solution. However, ζ-potential is *a priori* of a lesser magnitude than Ψ because corresponds not to the surface, but to some slipping plane located ~1 nm far from it. Hence it is just a lower estimate of $|\Psi_0|$. It was supposed that the rough and dynamical character of the micelle surface due to monomer motion reduces the potential fade near the surface smearing the difference between the Ψ and ζ values [24]. However, this assumption was later considered improbable because the slipping plane is located about 0.8 nm farther than the Stern layer [25].

So that, at present, only theoretical methods to the stated problem are available. The mostly used ones are based on solving the Poisson – Boltzmann (PB) equation, Eq. 2. This equation establishes the relation between the charge density of the system and the electrostatic potential created by it. The density is represented as a sum of two contributions: the fixed one, which is constant and belongs to the solute, and the mobile one, which depends on the electrostatic potential distribution in a self-consistent manner and represents the coions and counterions in the solution [26]. It is this equation that grounds the Goüy – Chapman model of EDL, as well as the Debye – Hückel theory of strong electrolytes.

$$\nabla \cdot (\varepsilon(x,y,z)\nabla\psi(x,y,z)) = -\frac{\rho(x,y,z)}{4\pi\varepsilon_0} = -\frac{\rho_f(x,y,z)}{4\pi\varepsilon_0} + \frac{Fc}{2\pi\varepsilon_0}\sinh\left(-\frac{F\psi(x,y,z)}{RT}\right) \qquad (2)$$

Here $\psi(x, y, z)$ is the electrostatic potential, ε_0 has its usual meaning, $\rho(x, y, z)$ is total charge density, $\varepsilon(x, y, z)$ is the relative permittivity (in the general case it is a function of coordinates, too), ρ_f is the fixed charge density, c is the total concentration of the electrolyte (assumed here to consist of single-charged ions).

Overall, the solvent is treated here as a continuum characterized with uniform relative permittivity, thus, disregarding the discrete nature of solvent molecules and ions. The solute is also treated as a continuum with some other value of relative permittivity. The ions are originally considered to be point charges occupying no volume. Nevertheless, by adjusting boundary conditions the ions may be attributed with a radius R_i for interaction with the solute making them unable to approach it tightly, as is assumed in the Stern model of EDL.

The PB equation is a non-linear differential equation of the second order, which makes its analytical solving possible just for the simplest geometries of charge distribution like uniformly charged planes, spheres, or cylinders. It can be linearized to facilitate solving, but this procedure is correct for relatively weakly

charged solutes only. The approximate analytical solution of this equation in its non-linear form for a uniformly charged spherical particle with radius r was deduced by Ohshima, Healy, and White, Eq. 3 [27]. It will be called Ohshima – Healy – White (OHW) equation further in the text.

The authors also derived the formula for cylindrical particles [27]. If the q_s value is known, Ψ_0 can be calculated and *vice versa*. In summary, there are two parameters for a micelle represented as a homogeneously charged sphere: radius and molecular area of a head group. In this respect, it is worth to mention the work by Lukanov and Firoozabadi who numerically solved the PB equation modified to incorporate non-electrostatic solute – ions interactions for similar geometry [28].

In principle, Eq. 3 may be used to predict the potential of Stern layer Ψ_δ instead of the surface potential Ψ_0. In such a case, the surface charge density is reduced due to the presence of adsorbed counterions. Hence, the q_s value must be multiplied by $(1 - \beta)$ to reflect the partial neutralization of the micelle charge, where β is the degree of neutralization. Additionally, the r value should be increased to match the total size of the micelle together with its Stern layer. It was shown that for well-defined colloidal systems like aqueous micellar solutions of SDS or cetyltrimethylammonium bromide (CTAB) such calculations give plausible results [16, 17].

Yet, despite the usefulness of the described equation, it is a severe simplification originating from the inability to analytically solve the PB equation for a case of complex geometry. However, at present one is no more constrained to analytical solutions due to the availability of computers allowing the direct numerical solving of this equation. Nowadays there is a variety of software developed for this sake [29]. There, the input is the atomistic model of the system of interest (consisting of the positions of atoms, their van der Waals radii and atomic point charges) and, the output is the corresponding distribution of the electrostatic potential in surrounding space.

$$q_s = \frac{2\varepsilon_0 \varepsilon RT\kappa}{F}\sinh(Y/2)\left(1+\frac{2}{\kappa r\cosh^2(Y/4)}+\frac{8\ln\left[\cosh(Y/4)\right]}{(\kappa r)^2\sinh^2(Y/2)}\right)^{\frac{1}{2}} \qquad (3)$$

$$q_s = \frac{e}{s} = e\frac{N_{aggr}}{4\pi r^2}; \qquad Y = \frac{F\Psi_0}{RT}; \qquad \kappa = \sqrt{\frac{2F^2 I}{\varepsilon_0 \varepsilon RT}}$$

Here, q_s is the surface charge density, s is the molecular area of a head group on the micellar surface, N_{aggr} is the aggregation number, e is the elementary charge, κ is the reciprocal Debye length, I is the ionic strength of a solution. (represented as a three-dimensional grid of $\psi(x, y, z)$ values). The solution parameters (relative permittivity, temperature, ionic strength) are also required. The main benefit of the numerical approach is that the charge distribution is considered in all its complexity with no need to simplify or impose some limitations on its geometry. Additionally, the interpolation schemes can be applied for $\varepsilon(x, y, z)$ at the solute-solvent boundary to form a smooth contact between the two continuums. Hence,

this technique is widely used for studying various biomolecules and biological assemblies (lipid membranes, individual proteins, and protein complexes including viruses) having an elaborate structure, where it reveals the regions of high positive or negative charge density [30–33]. However, to our knowledge, such objects as surfactant micelles have not been investigated with this method up to date.

This work aims to fill this gap and perform the numerical computations of the electrostatic potential around ionic micelles based on their accurate atomistic models instead of the simplified ones. We chose SDS and CTAB micelles for this study as the typical and well-defined ones. The produced results will be contrasted with the predictions of the simplified model given by the OHW equation.

EXPERIMENT AND DISCUSSION OF THE RESULTS. Computational procedure. The parameters of micelles required by the OHW equation (radius, surface area, degree of neutralization) were calculated grounding on the molecular dynamics simulations of SDS and CTAB micelles composed from 60 (the former) or 80 and 95 (the latter) surfactant monomers. Unlike SDS, for CTAB there is some spread in the experimental data about aggregation number, hence, two values of N_{aggr} were considered. We used the last 10 ns interval of the trajectories generated during our previous investigations of these systems, for details please refer to the corresponding papers [13, 14]. The radius was calculated in two ways: 1) as the gyration radius of hydrocarbon core multiplied by $\sqrt{5/3}$, and 2) as the position of the maximum of the radial distribution function (RDF) between micelle center of mass and S (N) head groups atoms. Both ways provided similar values (within 0.05 nm).

The solution parameters submitted to the OHW equation were: ε = 78.5; T = 298.15 K; I = 0.05 M = 50 mol m^{-3}.

To determine the degree of neutralization we calculated the radial distribution function $g(d)$ of counterions around the micelle, Eq. 4. It shows how much the density of counterions on distance d from the surface differs from the cell-average value. Preliminary, the function $N(d)$ was calculated as the total number of ions laying within distance d from the surface. The peaks on RDF's indicate the regions of increased ions density, hence, it is reasonable to define the Stern layer as the peak in $g(d)$.

$$g(d) = \frac{\rho(d)}{\rho_0} = \frac{1}{\rho_0}\frac{dN(d)}{dV(d)} = \\ = \frac{1}{\rho_0}\frac{1}{4\pi(r+d)^2}\frac{dN(d)}{dd} \quad (4)$$

Where ρ_0 is the cell-average number density of counterions, $\rho(d)$ is the number density of counterions at distance d from micelle, dN is the number of counterions within an infinitely thin layer around micelle at distance d, dV is the volume of this layer, which is approximated by the volume of a spherical layer, r is the micelle radius.

The input for PB computations was obtained in two stages. At first, the distribution of electrostatic potential around micelles was calculated using the Adaptive Poisson – Boltzmann solver (APBS) software [34,35]. The box size was chosen similar to the MD cell size, namely 8 nm for SDS and 10 nm for CTAB, and grid dimensions were 257×257×257. The micelle was centered in the box. Relative permittivity was set to 78.5 for water and 2 for micelle (matching higher alkanes like *n*-decane). Radius of solvent molecules was set to the

default value that is 0.14 nm. Because we deal with highly charged systems, non-linearized version of Poisson-Boltzmann equation was chosen. Both the cation and the anion of the background electrolyte were single-charged and were attributed with radius 0.1 nm for SDS and 0.2 nm for CTAB matching the ionic radii of Na^+ and Br^-, respectively [36]. The computations were carried out at a range of electrolyte concentrations from 0.05 M to 1 M including the case of no electrolyte.

The atomistic models were obtained from the above stated MD simulations of SDS and CTAB micelles. For each surfactant, 3 models were prepared by extracting instantaneous configurations from MD trajectory at 10 ns, 15 ns, and 20 ns. The atomic point charges were taken from the used potential models, which belong to the optimized potentials for liquid simulations – all-atom (OPLS-AA) force field [13, 14]. The atomic radii were provided by *gmx editconf* utility executed with *-mead* option specified.

The second stage was averaging the spatial distribution of the electrostatic potential $\psi(x, y, z)$ over relevant regions to get meaningful average values, which can be interpreted and compared with predictions of other methods. The quantities predicted by analytical models of micelles are usually related to the distance from the micelle surface, while the micelle shape itself is considered as a simple geometric form (sphere, cylinder etc.). However, in our case it appears non-trivial to define the concept of "distance from micelle surface" because the atomistic models have rough, irregular shapes preventing the application of simple geometric criteria like distance from the micelle center of mass. Consequently, it is difficult to outline the regions for averaging the $\psi(x, y, z)$.

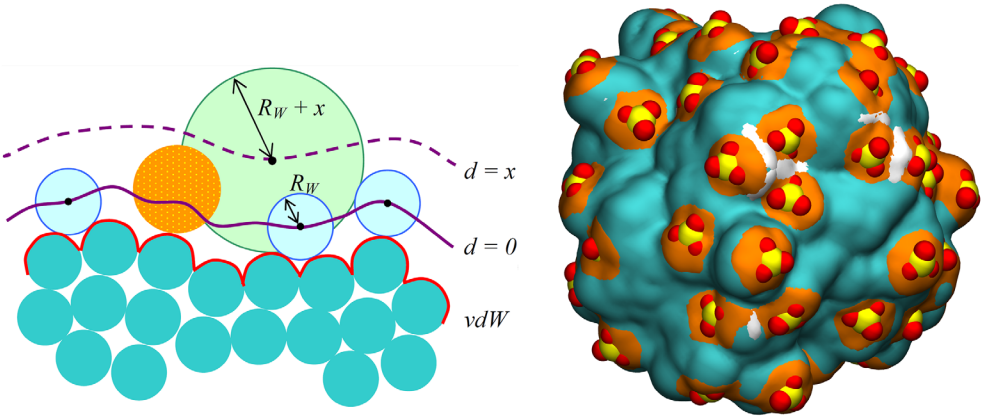

A B

Fig. 1. **A:** The principle of calculation of solvent-accessible surfaces. Dark blue circles – CH_2 groups of hydrocarbon core, dotted orange circle – a head group, red line "vdW" – van der Waals surface of hydrocarbon core, light blue outlined circles – solvent probes with radius R_W, light green outlined circle – solvent probe with radius $(R_W + x)$, solid and dashed violet lines – SAS of hydrocarbon core obtained with the smaller and the bigger probes, respectively. The former SAS establishes the origin of the distance scale, $d = 0$, and the points of the latter SAS are considered as located on distance x from the hydrocarbon core.

B: SDS micelle within its solvent-accessible surface. The regions of the surface located within 0.4 nm of S atoms are highlighted orange, and the regions within 0.5 nm of two S atoms are highlighted white. S and O atoms are shown as red and yellow spheres, respectively.

We solved this problem by employing solvent-accessible surfaces (SAS). According to the definition, SAS is the locus of the center of a spherical probe as it rolls over the accessible regions of the van der Waals surface of object. The probe radius R is usually set to the approximate radius of water molecules R_W that is 0.14 nm. In turn, the van der Waals (also called molecular) surface is the union of atom-centered spheres each having the radius set to the van der Waals radius of the corresponding atom [37]. Here we generated the solvent-accessible surface of the hydrocarbon core of micelles using the *gmx sasa* utility with the default value of the probe radius (0.14 nm) and increased precision (parameter *-dots 100*). The head groups OSO_3^- and $CH_2N(CH_3)_3^+$ were omitted in the calculation as not forming the surface but protruding from it. This SAS was considered as the actual micelle surface, and it set the origin for measuring distance d towards a bulk solution: all points of this SAS were attributed with $d = 0$. Further, a series of SAS was generated using larger probe radii of $(0.14+x)$ nm where x ranged from 0.05 to 1 nm. These surfaces were larger than the original one and represented an accurate equivalent to the notion "the place of points at distance x from micelle". The principle is illustrated in Figure 1A.

These surfaces were used then as the regions for averaging the electrostatic potential distribution. The average of $\psi(x, y, z)$ evaluated over the surface generated using probe radius $(0.14+x)$ nm was considered as the Ψ value at distance $d = x$ from micelle surface. Because each surface was intrinsically represented as a set of points, and the potential distribution was a three-dimensional grid, calculation of the average value was done by enumerating the surface points and summing up the values of potential there, which were in turn determined via trilinear interpolation between the neighboring grid points. Importantly, not all surface points were used here, but only a subset: we excluded the SAS points located closer than 0.4 nm to any S (N) atom of head groups and the points within 0.5 nm of two or more S (N) atoms at the same time. The justification is provided in the Results section below. An example of a SAS with the indication of the excluded regions is shown in Figure 1B.

Table 1

The parameters of micelles and subsequent solutions of OHW equation

surfactant	N_{aggr}	r, nm	s, nm^2	$\lvert\Psi_0\rvert$, mV	β	$\lvert\Psi_\delta\rvert$, mV
SDS	60	1.81	0.686	139	0.48	94
CTAB	80	2.22	0.774	134	0.61	75
CTAB	95	2.35	0.731	138	0.65	74

Table 2

Electrostatic potential of micelles from numerical solution of PB equation at I = 0.05 M

surfactant	N_{aggr}	$\lvert\Psi_0\rvert$, mV	$\lvert\Psi(0.2)\rvert$, mV	$\lvert\Psi(0.4)\rvert$, mV	$\lvert\Psi_\delta\rvert$, mV
SDS	60	100	85	68	75
CTAB	80	149	106	76	70
CTAB	95	151	111	85	78

Firstly, we focus on the theoretical predictions of the OHW equation. The parameters of micelles obtained from MD simulations (r, s, β) and the subsequent solutions of Eq. 2 are collected in Table 1. For Ψ_δ calculation, the micelle radius r was increased by 0.1 nm in order to reflect the incorporation of neighboring ions (the s value was accordingly changed, too). We deliberately chose the addition less than δ because the visual examination of MD trajectories revealed that most of these counterions are located in between the head groups or alongside them, therefore, do not advance far towards a bulk solution. The analysis of $g(d)$ graphs suggested placing the Stern layer boundary δ at about 0.32 nm for SDS and 0.45 nm for CTAB, Figure 2. The corresponding β values found as $N(\delta)/N_{aggr}$ are 0.48 and 0.61, respectively. We note that the experimentally determined β values vary within the range of 0.5–0.9 for different surfactants and depend on the method used [3, 15].

There is no significant difference found between Ψ values of CTAB micelles composed of 80 and 95 monomers indicating the negligible effect of the micelle size in this case.

Now we turn to the results of PB calculations. From the qualitative point of view, visual examination of the electrostatic potential distribution depicted as equipotential surfaces (isosurfaces) reveals its complex shape. $\psi(x, y, z)$ is quite uniform near the regions where the hydrocarbon core is exposed to water, however, it sharply increases in magnitude upon approaching the head groups. Its gradient increases there, too, as is evidenced by a tighter spacing between isosurfaces: there the magnitude reaches ≥260 mV/nm, while far from head groups it drops to ≤80 mV/nm.

To get quantitative results we averaged $\psi(x, y, z)$ following the procedure described in the Computational procedure section. The previous observations motivated us to exclude the vicinities of head groups from averaging: these regions, while having comparatively small total area, are located at $\psi(x, y, z)$ values very different from the rest of the surface. Therefore, keeping them would distort the average.

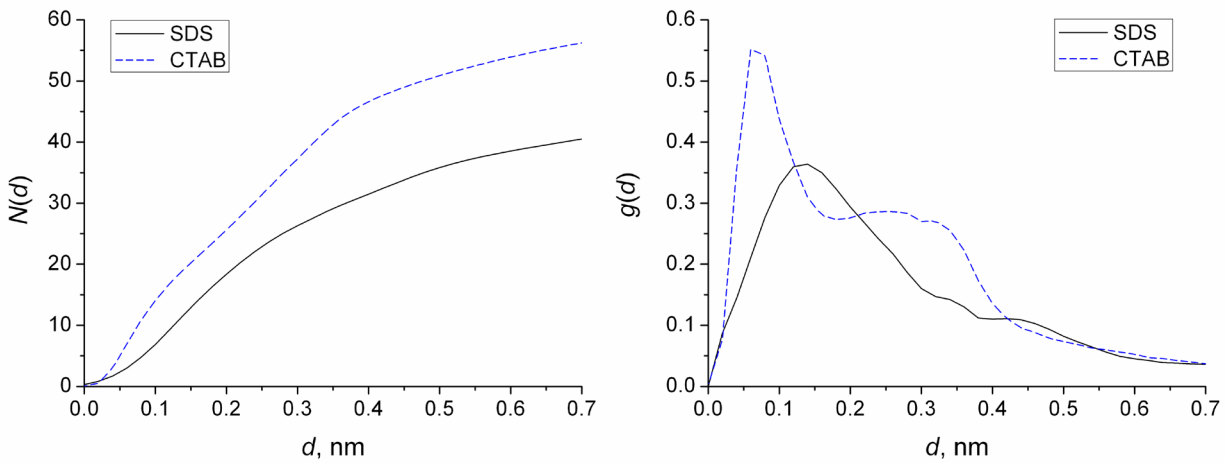

Fig. 2. A: the number of counterions at given distance from micelle surface; B: radial distribution function of counterions around the micelle. The origin corresponds to the solvent-accessible surface of hydrocarbon core.

The produced dependences of Ψ on distance from micelle surface and ionic strength are presented in Figures 3, 4A and summarized in Table 2. The profiles demonstrate the expected behavior of gradual monotonic decrease towards zero with distance and ionic strength. At similar conditions, Ψ around CTAB micelles have a larger magnitude than around the SDS ones. It should be emphasized that the data for high ionic strengths is rather evaluative because all the computations were done using the same atomistic model. While at such conditions the micelles usually change shape from ellipsoidal to rod-like.

A feature of the numerical computations is the possibility to handle the case of a "bare" micelle in the absence of counterions and background electrolyte. In this case $I = 0$ and κ^{-1} tends to infinity preventing the use of the OHW equation. The estimated Ψ_0 values equaled –535 mV and +630 mV for SDS and CTAB micelles, respectively.

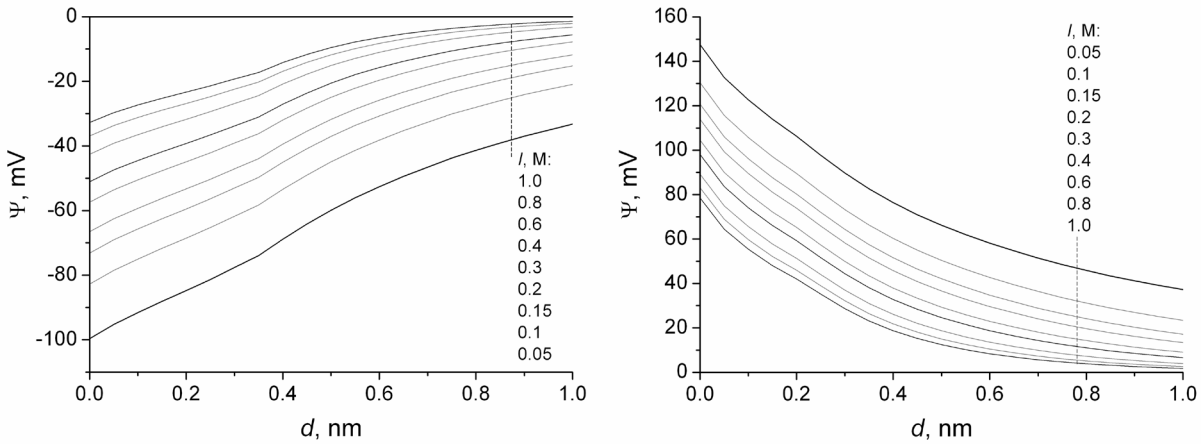

Fig. 3. Profiles of electrostatic potential fade with distance for SDS (A) and CTAB (B) micelles at different ionic strengths.

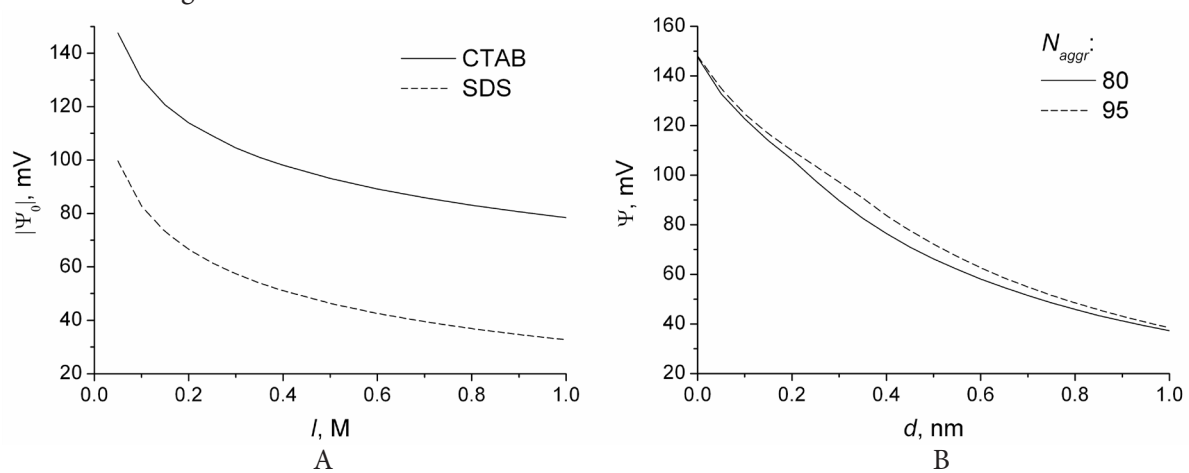

Fig. 4. **A:** Dependence of surface electrostatic potential on ionic strength for SDS and CTAB micelles; **B:** Profile of electrostatic potential fade with distance for CTAB micelles of different sizes at $I = 0.05$ M.

Table 3

Effect of counterions radius on Ψ_0 from the numerical solution of PB equation at I = 0.05 M. The original values are highlighted in bold

surfactant	N_{aggr}	$\lvert\Psi_0\rvert$, mV		
		R_i = 0.2 nm	R_i = 0.1 nm	R_i = 0
SDS	60	130	**100**	71
CTAB	80	**149**	106	74

To check the robustness of the presented results, we varied several factors, which can affect the computed $\psi(x, y, z)$ distributions.

The graphs presented above were produced, basing on a single model for each micelle. To estimate the effect of the choice of configuration, we repeated the computations at I = 0.05 M using two other models. The produced Ψ profiles were within 5 mV at d = 0 and within 3 mV for larger d indicating that using a single model is enough to get a correct result. The possible reason is that the main structural motifs of the micelle surface are observed at any time during the evolution of its shape. We note that the values in Table 2 are averages over three models.

Next, because of the uncertainty with N_{aggr} of CTAB micelles we repeated the computations using the models with N_{aggr} = 95 instead of 80. Both results are confronted in Table 2 and Figure 4B. It is seen that while some difference is present, the profiles agree well: the Ψ values almost coincide at the shortest (≤0.15 nm) and longest (≥0.7 nm) d values. In between the discrepancy is no more than 10 mV that is moderate. This is in line with the behavior of the OHW equation.

A crucial factor is the radius of ions of the background electrolyte. We tested the values 0.2 nm for SDS (instead of 0.1 nm) and 0.1 nm for CTAB (instead of 0.2 nm). Also, the point-like case (R_i = 0) was checked. Unlike the previous factors, here the influence appeared significant for both kinds of micelles: each decrease of R_i by 0.1 nm reduced $\lvert\Psi_0\rvert$ by 30–40 mV, Table 3. This effect is expected due to the appearance of counterions closer to the surface.

Finally, we tested the influence of the computation parameters. The box size increase to 12×12×12 nm^3 and the grid dimensions decrease to 129×129×129 were found to cause the negligible difference of Ψ_0 (<3 mV).

First of all, the comparison of results in Tables 1 and 2 shows that both OHW equation and numerical computations provide the magnitude of Ψ_0 in the range of 100–150 mV for both kinds of micelles. The closer look, however, reveals a discrepancy: while OHW equation predicts almost equal $\lvert\Psi_0\rvert$ for SDS and CTAB (within 5 mV), their numerical results are much different (by ~50 mV). This behavior seems rather surprising because both ways are based on the same theory (that is Eq. 2) and requires explanation.

The main distinction between the ways is the geometry of the model: while the OHW equation represents the micelle with head groups as a smooth sphere with the uniformly distributed charge, in numerical computations the protrusion of head groups from the hydrocarbon core and their discrete charge is taken into account.

The second distinction is more subtle but no less important: in the derivation of the OHW equation, the ions were treated as point charges implying they approach infinitely close to the solute. Oppositely, the used software for numerical solution allowed tuning the distance of the closest approach between the ions and the solute in terms of ions radii R_i. As was mentioned before, this parameter strongly affects the results. The examination of Table 3 shows that if equal radii are used, the Ψ_0 values of SDS and CTAB become much closer (within 7–20 mV) resembling the behavior of the OHW equation.

Still, there remains the difference in predicted Ψ_0 magnitude. Surprisingly, the closest match between OHW and numerical predictions is observed for R_i = 0.2 nm instead of zero size. We attribute this fact to the geometry of the models *via* the following qualitative consideration. The discrete head groups have a high charge density. When their charge is smeared across the whole surface, the charge density proportionally decreases. As a result, such uniformly charged surface exerts proportionally weaker attraction to counterions. This, however, leads to exponentially smaller concentration and charge density of the approached counterions. Therefore the original surface charge becomes neutralized to a lesser extent resulting in higher $|\Psi_0|$ values. To achieve the same magnitude in numerical computation one has to artificially prevent counterions from accumulating around highly charged head groups by attributing the ions with ~0.2 nm radii.

Considering the surface potential of "bare" micelles without counterions, its large magnitude against the $|\Psi_0|$ values in Table 2 indicates the effect exerted by the outer part of EDL.

Turning to the potential of Stern layer Ψ_δ, both ways agree that for CTAB it equals ~75 mV. For SDS the numerical result is –75 mV. Its direct comparison with the OHW solution is impossible because of the discrepancies described above.

To summarizing, in our opinion the distinction of results of the used ways is caused by the different treatment of head groups and counterions. Among the two ways, we have a preference for the numerical solution because it implies fewer simplifications and assumptions and, thus, provides a more realistic treatment of the examined systems. Nevertheless, the analytical equation produces the values of correct magnitude with much less computational effort.

CONCLUSIONS. The surface electrostatic potential Ψ_0 of micelles of common surfactants sodium dodecyl sulfate and cetyltrimethylammonium bromide was estimated by two theoretical approaches based on the Poisson – Boltzmann equation. The analytical equation derived for uniformly charged spherical particles and point-like counterions was found to provide similar Ψ_0 values for both micelles. Oppositely, the numerical solution with the geometry of the systems accurately reproduced and ions attributed with radii equal to their ionic radii resulted in pronouncedly higher Ψ_0 of CTAB micelles than of SDS ones. Namely, at background electrolyte ionic strength of 0.05 M the values equaled +150 mV and –100 mV, respectively. By the same approach, the electrostatic potential on the boundary of the Stern layer Ψ_δ was found to be *ca.* +74 mV and –75 mV, respectively. The discrepancy between the approaches was explained on the basis of the assumptions and simplifications made in them.

*ACKNOWLEDGEMENTS. T***he authors thank the Ministry of Education and Science of Ukraine for financial support in the framework of the project "Novel nanomaterials based on the lyophilic self-assembled systems: theoretical prediction, experimental investigation, and biomedical applications" (0120U101064).**

КОНТИНУАЛЬНО-ЕЛЕКТРОСТАТИЧНЕ ДОСЛІДЖЕННЯ ЙОННИХ МІЦЕЛ ІЗ ВИКОРИСТАННЯМ АТОМІСТИЧНИХ МОДЕЛЕЙ

В. С. Фарафонов,* О. В. Лебідь, М. О. Мчедлов-Петросян

Харківський національний університет імені В. Н. Каразіна, пл. Свободи, 4, Харків, 61022, Україна
**e-mail: farafonov@karazin.ua*

Розглянуто питання про ключовий параметр, пов'язаний з будовою подвійного електричного шару міцел йоногенних ПАР, – електростатичний потенціал. Наведено короткий огляд експериментальних методів та теоретичних моделей для оцінки електростатичного потенціалу. Запропоновано метод розрахунку електростатичного потенціалу, який базується на чисельному розв'язанні рівняння Пуассона – Больцмана, з використанням атомістичної моделі міцели йоногенної ПАР. Необхідні для побудови атомістичних моделей параметри одержано з молекулярно-динамічного моделювання. Із використанням цього методу розраховано електростатичний потенціал для міцел додецилсульфату натрію та броміду цетилтриметиламонію при різних іонних силах. Результати обговорюють порівняно зі значеннями, розрахованими в рамках спрощеної моделі за рівнянням Ошими – Хілі – Уайта.

Ключові слова: міцела поверхнево-активної речовини, шар Штерна, електростатичний потенціал, рівняння Пуассона – Больцмана, доступна для розчинника поверхня.

REFERENCES

1. Surfactants science and technology. Retrospects and Prospects. Ed. Romsted L. S. Boca Raton: CRC Press. 2014.
2. Handbook of Surface and Colloid Chemistry. Ed. Birdi K. S. Boca Raton: CRC Press, 2009.
3. Mchedlov-Petrossyan N. O., Vodolazkaya N. A., Kamneva N. N. Acid-base equilibrium in aqueous micellar solutions of surfactants. In: Micelles: Structural Biochemistry, Formation and Functions & Usage. Ed. Bradburn D., Bittinger *J. N. Y.: Nova Publishers*. 2013. Chapter 1. 1–71.
4. Rusanov A. I. Micellization in Surfactant Solutions. Reading: Harwood Academic Publishes. 1997.
5. Rusanov A. I. Nanothermodynamics: chemical approach. *Russian Chemistry Journal*. 2006. **50** (2): 145–151 [in Russian].
6. Shinoda K. The significance and characteristics of organized solutions. *Journal of Physical Chemistry*. 1985. **89** (11): 2429–2431. https://doi.org/10.1021/j100257a055.

7. Organized Solutions. Surfactants in Science and Technology. Ed. Friberg S. E., Lindman B. N.Y.: Marcel Dekker. 1992.
8. Stigter D. On the Adsorption of Counterions at the Surface of Detergent Micelles. *Journal of Physical Chemistry*. 1964. **68** (13): 3603–3611. https://doi.org/10.1021/j100794a028.
9. Stigter D. Micelle formation by ionic surfactants. III Model of Stern layer, ion distribution, and potential fluctuation. *Journal of Physical Chemistry*. 1975. **79** (10): 1008–1013. https://doi.org/10.1021/j100577a013.
10. Rathman J. F., Scamehorn J. F. Counterion binding on mixed micelles. Journal of Physical Chemistry. 1984. **88** (24): 5807–5816. https://doi.org/10.1021/j150668a014.
11. Gilányi T. Fluctuating micelles: a theory of surfactant aggregation 2. Ionic surfactants. *Colloids and Surfaces A: Physicochemical and Engineering Aspects*. 1995. **104** (1): 119–126. https://doi.org/10.1016/0927-7757(95)03223-Z.
12. Roussel G., Michaux C., Perpete E. A. Multiscale molecular dynamics simulations of sodium dodecyl sulfate micelles: from coarse-grained to all-atom resolution. *Journal of Molecular Modeling*. 2014. **20**: 2469–2476. https://doi.org/10.1007/s00894-014-2469-0.
13. Farafonov V. S., Lebed A. V. Developing and validating a set of all-atom potential models for sodium dodecyl sulfate. *Journal of Chemical Theory and Computation*. 2017. **13** (6): 2742–2750. https://doi.org/10.1021/acs.jctc.7b00181.
14. Farafonov V. S., Lebed A. V. Molecular dynamics simulation study of cetylpyridinum chloride and cetyltrimethylammonium bromide micelles. *Kharkov University Bulletin, Chemistry Series*. 2016. **27** (50): 25–30. https://doi.org/10.26565/2220-637X-2017-27-03.
15. Mchedlov-Petrossyan N. O. Protolytic equilibrium in lyophilic nano-sized dispersions: Differentiating influence of the pseudophase and salt effects. *Pure and Applied Chemistry*. 2008. **80** (7): 1459–1510. https://doi.org/10.1351/pac200880071459.
16. Hartland G.V., Grieser F., White L.R. Surface potential measurements in pentanol-sodium dodecyl sulphate micelles. *Journal of Chemical Society, Faraday Transactions*. 1978. **1** (83): 591–613. https://doi.org/10.1039/F19878300591.
17. Mchedlov-Petrossyan N. O., Vodolazkaya N. A., Yakubovskaya A. G., Grigorovich A.V., Alekseeva V. I., Savvina L. P. A novel probe for determination of electrical surface potential of surfactant micelles: N,N'-di-n-octadecylrhodamine. *Journal of Physical Organic Chemistry*. 2007. **20** (5): 332–344. https://doi.org/10.1002/poc.1150.
18. Fernandez M. S., Fromherz P. Lipoid pH indicators as probes of electrical potential and polarity in micelles. *Journal of Physical Chemistry*. 1977. **81** (18): 1755–1761. https://doi.org/10.1021/j100533a009.
19. Funasaki N. Micellar effects on the kinetics and equilibrium of chemical reactions in salt solutions *Journal of Physical Chemistry*. 1979. **83** (15): 1998–2003. https://doi.org/10.1021/j100478a014.
20. Grieser F., Drummond C. J. The physicochemical properties of self-assembled surfactant aggregates as determined by somemolecular spectroscopic probe techniques. *Journal of Physical Chemistry*.

1988. **92** (20): 5580–5593. https://doi.org/10.1021/j100331a012.

21. Khlestkin V. K., Polienko J. F., Voinov M. A., Smirnov A. I., Chechik V. Interfacial Surface Properties of Thiol-Protected Gold Nanoparticles: A Molecular Probe EPR Approach. *Langmuir*. 2008. **24** (3): 609–612. https://doi.org/10.1021/la702823n.
22. Voinov M. A., Kirilyuk I. A., Smirnov A. I. Spin-labeled pH-sensitive phospholipids for interfacial pka determination: synthesis and characterization in aqueous and micellar solutions. *Journal of Physical Chemistry B*. 2009. **113** (11): 3453–3460. https://doi.org/10.1021/jp810993s.
23. Bulavin L. A., Garamus V. M., Karmazina T. V., Pivnenko E. N. Measurements of structural and electrostatic parameters and surface tension of micelles of an ionic surfactant versus concentration, ionic strength of solution and temperature by small-angle neutron scattering. *Colloids and Surfaces A: Physicochemical and Engineering Aspects*. 1998. **131** (1–3): 137–144. http://dx.doi.org/10.1016/S0927-7757 (96)03882-4.
24. Aniansson G. E. A. Dynamics and structure of micelles and other amphiphile structures. Journal of Physical Chemistry. 1978. **82** (26): 2805–2808. https://doi.org/10.1021/j100515a011.
25. Lyklema J. Surface charges and electrokinetic charges: distinctions and juxtapositionings. *Colloids and Surfaces A: Physicochemical and Engineering Aspects*. 2011. **376** (1–3): 2–8. https://doi.org/10.1016/j.colsurfa.2010.09.021.
26. Cai Q., Hsieh M. J., Wang J., Luo R. Performance of nonlinear finite-difference Poisson – Boltzmann solvers. *Journal of Chemical Theory and Computation*. 2010. **6** (1): 203–211. https://dx.doi.org/10.1021%2Fct900381r.
27. Ohshima H., Healy T. W., White L. R. Accurate analytic expressions for the surface charge density/surface potential relationship and double-layer potential distribution for a spherical colloidal particle. *Journal of Colloid and Interface Science*. 1980. **90** (1): 17–26. https://doi.org/10.1016/0021-9797(82)90393-9.
28. Lukanov B., Firoozabadi A. Specific ion effects on the self-assembly of ionic surfactants: a molecular thermodynamic theory of micellization with dispersion forces. *Langmuir*. 2014. **30** (22): 6373–6383. https://doi.org/10.1021/la501008x.
29. Li C., Li L., Petukh M., Alexov E.. Progress in developing Poisson-Boltzmann equation solvers. *Molecular Based Mathematical Biology*. 2013. **1** (1): 42–62. https://dx.doi.org/10.2478%2Fmlbmb-2013-0002.
30. Schweke H., Mucchielli M.-H., Sacquin-Mora S., Bei W., Lopes A. Protein interaction energy landscapes are shaped by functional and also non-functional partners. *Journal of Molecular Biology*. 2020. **432** (4): 1183–1198. https://doi.org/10.1016/j.jmb.2019.12.047.
31. Tarasova E., Farafonov V., Taiji M., Nerukh D. Details of charge distribution in stable viral capsid. *Journal of Molecular Liquids*. 2018. **265**: 585–591. https://doi.org/10.1016/j.molliq.2018.06.019.
32. Tarabara U., Vus K., Girnyk S., Kamneva N., Lavryk O., Mikhailyuta M., Trusova V., Gorbenko G. Effect of amyloid fibrils on electrokinetic properties of lipid vesicles. *East European Journal of Physics*. 2017. **4** (2): 19–28. https://doi.org/10.26565/2312-4334-2017-2-0.

33. Callenberg K. M., Choudhary O. P., de Forest G. L., Gohara D. W., Baker N. A., Grabe M. APBSmem: a graphical interface for electrostatic calculations at the membrane. *PLOS One*. 2010. **5** (9): e12722. https://doi.org/10.1371/journal.pone.0012722
34. Baker N. A., Sept D., Joseph S., Holst M. J., McCammon J. A. Electrostatics of nanosystems: application to microtubules and the ribosome. *Proceedings of the National Academy of Sciences of the U.S.A*. 2001. **98** (18): 10037–10041. https://doi.org/10.1073/pnas.181342398.
35. Jurrus E., Engel D., Star K., Monson K., Brandi J., Felberg L. E., Brookes D. H., Wilson L., Chen J. Improvements to the APBS biomolecular solvation software suite: Improvements to the APBS Software Suite. *Protein Science*. 2017. **27** (1): 112–128. https://doi.org/10.1002/pro.3280.
36. Shannon R. D. Revised effective ionic radii and systematic studies of interatomie distances in halides and chaleogenides. *Acta Crystallographica*. 1976. **A32**: 751–767. https://doi.org/10.1107/S0567739476001551.
37. Connolly M. Analytical molecular surface calculation. *Journal of Applied Crystallography*. 1983. **16** (5): 548–558. https://doi.org/10.1107/S0021889883010985.

Стаття надійшла 12.07.2021.

УДК 544.654.076.324.4:546.26 doi: 10.33609/2708-129X.87.06.2021.70-81

ОСОБЛИВОСТІ ЕЛЕКТРОВІДНОВЛЕННЯ Li_2CO_3 В ЕКВІМОЛЯРНОМУ РОЗПЛАВІ ХЛОРИДІВ НАТРІЮ ТА КАЛІЮ

І. А. Новоселова[1*], С. В. Кулешов[1], А. О. Омельчук[1], В. М. Биков[2], О. М. Фесенко[2]

[1] Інститут загальної та неорганічної хімії імені В. І. Вернадського НАН України, просп. Академіка Палладіна, 32/34, Київ 03142, Україна
[2] Інститут фізики НАН України, просп. Науки, 46, Київ 03028, Україна
**e-mail: inessa_nov@ukr.net*

Наведено результати досліджень електрохімічного відновлення Li_2CO_3 в розплавленій еквімолярній суміші хлоридів натрію та калію в різних газових середовищах (повітря, аргон, діоксид вуглецю). Відновлення Li_2CO_3 до вуглецю на повітрі відбувається через стадію попередньої хімічної реакції кислотно-основного типу з утворенням двох електрохімічно активних частинок CO_2 і $Li_xCO_3^{2-x}$ за потенціалів –0,8 та –1,7, відповідно, відносно $Pb|PbCl_2$ електрода порівняння. Обидва процеси незворотні, причому лімітуючою стадією відновлення $Li_xCO_3^{2-x}$ є дифузія деполяризатора до поверхні електрода. В атмосфері аргону та CO_2 у процесі електровідновлення бере участь лише $Li_xCO_3^{2-x}$. Методами РФА, СЕМ та КР-спектроскопії встановлено, що катодний продукт – це аморфний вуглець із високою розупорядкованістю. Агломеровані частинки складаються з деградованих графенових структур із приблизним розміром кристалітів – 30–40 нм.

Ключові слова: карбонат літію, електровідновлення, розплави солей, вуглецеві наноматеріали.

ВСТУП. Вивченню особливостей електровиділення вуглецю із карбонатних і галогенідно-карбонатних розплавів присвячено великий цикл робіт, починаючи з поч. XX ст. Встановлено, що за певних умов електролізу на катоді формується фаза вуглецю у вигляді плівок або порошків із 100% виходом за струмом або утворюється монооксид вуглецю CO. В останні 10 років цей напрям досліджень набув особливої актуальності і привертає увагу провідних наукових центрів світу [1–10]. Це пов'язано з перспективою вирішення за допомогою цього процесу важливого екологічного завдання – утилізації діоксиду вуглецю, що входить до складу парникового газу.

На сьогодні відомо, що для отримання вуглецю використовують термічно нестійкі карбонати першої і другої груп періодичної системи, а саме: Li_2CO_3, Na_2CO_3, $MgCO_3$, $CaCO_3$, $BaCO_3$ [11–16]. Багато питань щодо

морфології, структури і дисперсності вуглецевих продуктів відновлення однозначно не розкрито й досі. Найчастіше вивчали електровідновлення карбонату літію як в чисто карбонатних, так і змішаних галогенідно-карбонатних розплавах, але літературні відомості з електровиділення вуглецю із Li_2CO_3 містять цілу низку розбіжностей. Наприклад, не визначено єдиного механізму, за яким відбувається електровідновлення Li_2CO_3, точно не встановлено потенціали, за яких утворюється вуглець, не враховано вплив катіонного оточення на особливості розряду карбонат-аніону та морфологічні і структурні властивості вуглецевих фаз, не з'ясовано, які електрохімічні частинки беруть участь у процесі тощо. Метою роботи було вивчення процесу електровідновлення Li_2CO_3 на фоні розплавленої суміші NaCl–KCl у широкому діапазоні концентрацій Li_2CO_3 ($1{,}0–15{,}0\times10^{-4}$ моль/см^3), швидкостей поляризації (0,02–0,10 мВ/с) та різних газових атмосферах (повітря, аргон та CO_2).

ЕКСПЕРИМЕНТ І ОБГОВОРЕННЯ РЕЗУЛЬТАТІВ. Особливості електровідновлення Li_2CO_3 вивчали методом циклічної вольтамперометрії за температури 750 °С, швидкостях поляризації – V = 0,1, 0,05, та 0,02 В/с, у широкому діапазоні потенціалів. Дослідження проводили на повітрі, в атмосферах аргону і CO_2 у кварцовій та сталевій (розробленій для роботи під тиском) комірках (рис. 1).

Робочими електродами (катодами) слугували платинові голчасті та пластинчасті електроди площею ~0,24 і ~3,6 см^2 відповідно. Як анод (допоміжний електрод) використовували скловуглецеві (СВ) пластини, площа поверхні яких була значно більшою за поверхню катода. Електродами порівняння (ЕП) були Pt квазіобернений ($Pt|O_2/O^{2-}$) та свинцевий ($Pb|PbCl_2$) електроди. Для розплавленого електроліту використовували скловуглецеві, алундові чи платинові тиглі. Електрохімічні комірки розташовували у печі «СШОЛ–1.1.6» із вертикальною нагрівальною шахтою, термостатування якої забезпечували за допомогою електронного потенціометра «КВП–1503» та платино-платинородієвої термопари як датчика температури.

Фоновим електролітом слугувала розплавлена еквімолярна суміш солей NaCl–KCl (1:1). NaCl та KCl (кваліфікації «х. ч.») попередньо сушили за температури 150 °С упродовж 12 годин із подальшим сплавлянням у платиновому тиглі за температури 700 °С. Охолоджений розплав розтирали в агатовій ступці і повторно висушували. Li_2CO_3 («х. ч.»), висушували упродовж 24 годин за температури 200 °С.

Для вольтамперометричних досліджень та проведення електролізів використовували потенціостат «ПИ–50–1» із програматором «ПР–8». Реєстрацію вольтамперограм здійснювали на двокоординатному приладі «ЛКД–4» із подальшим оцифруванням за допомогою програмного забезпечення «GetData Graph Digitizer 2.26».

Продукти відновлення характеризували методами РФА (дифрактометр «ДРОН–3М», CuKα–випромінення), СЕМ (растровий електронний мікроскоп «JEOL JSM–35») та спектроскопії КРС («Renishaw inVia Raman Microscope», Ne–He-лазер із довжиною хвилі 633 нм).

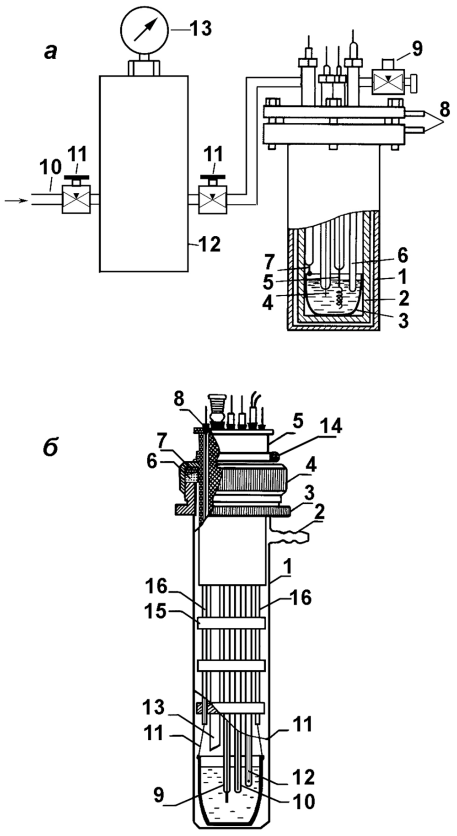

Рис. 1. *(а)* – Схема сталевої герметичної установки для роботи під тиском: *1* – стальний реактор автоклавного типу; *2* – кварцовий стакан; *3* – тигель; *4* – індикаторний електрод; *5* – електрод порівняння; *6* – термопара; *7* – струмопровід; *8* – водяне охолодження реактора; *9* – клапан скидання тиску в камері; *10* – з'єднувальний шланг; *11* – кран регулювання подачі газу; *12* – стальний ресивер (V = 2 л); *13* – манометр.

(б) – Схема кварцової електрохімічної комірки для роботи в газовій атмосфері: *1* – кварцовий стакан; *2* – штуцер для вакуумування; *3* – кільце з різьбою; *4* – стальна гайка; *5* – фторопластова втулка; *6* – кільце із вакуумної гуми; *7* – кільце із фторопласта; *8* – пробки з вакуумної гуми; *9* – індикаторний електрод; *10* – електрод порівняння; *11* – струмопроводи до анода; *12* – термопара; *13* – трубка для подачі солей; *14* – стопорне кільце; *15* – термостійкі шайби; *16* – алундові трубки.

Результати вольтамперометричних досліджень відновлення карбонату літію в атмосфері повітря наведено на рис. 2. Аналіз отриманих результатів показав, що розряд фонового електроліту з виділенням лужного металу починається за потенціалу ~ -1,8 В відносно $Pb|PbCl_2$ ЕП (крива 1). Жодних додаткових хвиль на вольтамперограмі не реєструється, що свідчить про відсутність сторонніх домішок. У розплав NaCl–KCl послідовно (по $0{,}25\times10^{-3}$ моль/см^3) додавали Li_2CO_3, починаючи з концентрації $0{,}1\times10^{-3}$ моль/см^3. Інтервал між зніманням вольтамперограм за різних концентрацій становив не менше 10 хв.

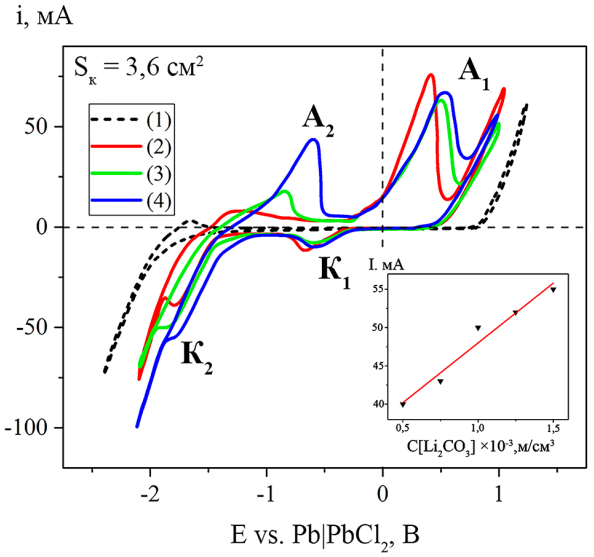

Рис. 2. Вольтамперограми розплаву Na,K|Cl (*1*), що містив Li_2CO_3: (*2*) – 0,5, (*3*) – 1,0, (*4*) – 1,5 × 10^{-3} моль/см^3. t = 750 °С; V = 0,1 В/с; $S_к$ = 3,6 см^2; $Pb|PbCl_2$ ЕП; атмосфера повітря. Вставка – залежність сили струму від концентрації Li_2CO_3.

За концентрації у фоновому розплаві $0{,}5\times10^{-3}$ моль/см^3 Li_2CO_3 в катодній області потенціалів на вольтамперограмі реєструють дві хвилі K_1 і K_2 при $E_{п/2}$ = -0,45 та -1,6 В

відповідно (крива 2). На зворотному ході вольтамперограми, в анодній області, їм відповідають хвилі A_1 та A_2 ($E_{п/2}$ = +0,2 та -1,2 В відповідно), що характеризують окиснення продуктів катодного відновлення. Подальше збільшення концентрації Li_2CO_3 у розплаві (рис. 2, криві 3, 4) зумовлює зростання висоти як катодної хвилі K_2, так і анодної A_2, що їй відповідає. Висота хвиль K_1 і A_1 залишається практично незмінною. Відбувається незначне зміщення потенціалів катодних і анодних хвиль у позитивну область. Процес, якому відповідає хвиля K_2, контролюється швидкістю доставки деполяризатора до поверхні електрода, оскільки при збільшенні концентрації Li_2CO_3 у розплаві (криві 3–4) відбувається прямо пропорційне зростання сили струму, що відповідає пікам цих хвиль (рис. 2, вставка).

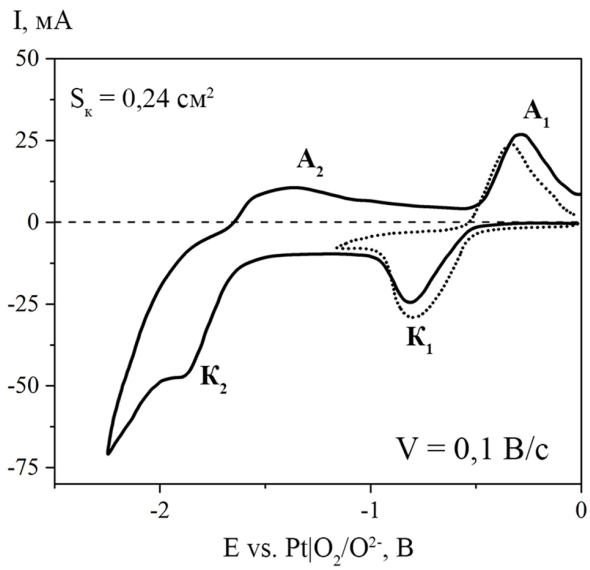

Рис. 3. Вольтамперограми розплавленої суміші Na,K|Cl–Li_2CO_3 ($0{,}75\times10^{-3}$ моль/см^3) в різних інтервалах сканування потенціалу. t = 750 °C; $S_к$ = 0,24 см^2; Pt|O_2/O^{2-} ЕП; атмосфера повітря.

Якщо циклічну вольтамперограму записати в інтервалі розгортки потенціалів, який не досягає потенціалу хвилі K_2 (-2,25 В), наприклад, в інтервалі від 0 до -1,2 В (пунктирна лінія, рис. 3), то, як і у випадку, коли вольтамперограму записували в інтервалі потенціалів від 0 до -2,25 В (суцільна лінія, рис. 3), в анодній області при $E_{п/2}$ = -0,45 В (відносно Pt|O_2/O^{2-} ЕП) також реєструють одну хвилю. Це свідчить на користь того, що хвиля A_1 характеризує окиснення продукту, утвореного в інтервалі потенціалів хвилі K_1.

Наявність добре відтворюваних хвиль на вольтамперограмах дозволяє оцінити лімітуючі стадії електродного процесу і деякі його параметри. Характер стадії перенесення заряду визначали за загальноприйнятими критеріями, а саме:

– із залежності потенціалу напівпіку катодної хвилі від швидкості поляризації (критерій Делахея [17]):

$$E_{n/2} = -CRT/\alpha n_\alpha F - \ln(D^{1/2})RT/\alpha n_\alpha F + \ln(k^0_s)RT/\alpha n_\alpha F - \ln(\alpha n_\alpha v^{1/2})RT/\alpha n_\alpha F) \quad (1)$$

де $E_{n/2}$ – потенціал напівпіку, В; C – концентрація деполяризатора, моль/см^3; R – універсальна газова стала, Дж/моль·К; T – температура, К; α – коефіцієнт переносу; n_α – кількість електронів, які беруть участь в електродному процесі; F – стала Фарадея, Кл/моль; D – коефіцієнт дифузії, см^2/с; k^0_s – гетерогенна константа швидкості електродного процесу; v – швидкість поляризації, В/с.

– за значеннями потенціалу півширини піку ($\Delta E = E_{пк} - E_{пк/2}$) (критерій Матсуди – Аябе [18]):

$$\Delta E = 1{,}857\ RT / \alpha n_\alpha F \quad (2)$$

Зменшення швидкості сканування потенціалу (рис. 4) зумовлює зменшення сили

струму, що відповідає пікам катодних та анодних хвиль, і зміщення потенціалу обох хвиль у позитивну область. Згідно діагностичного критерію Делахея це свідчить про те, що електрохімічні процеси в цьому інтервалі потенціалів незворотні. Із рівняння Матсуди – Аябе розраховано коефіцієнти переносу заряду, для хвиль K_1 і K_2 вони дорівнюють 0,26 та 0,41 відповідно.

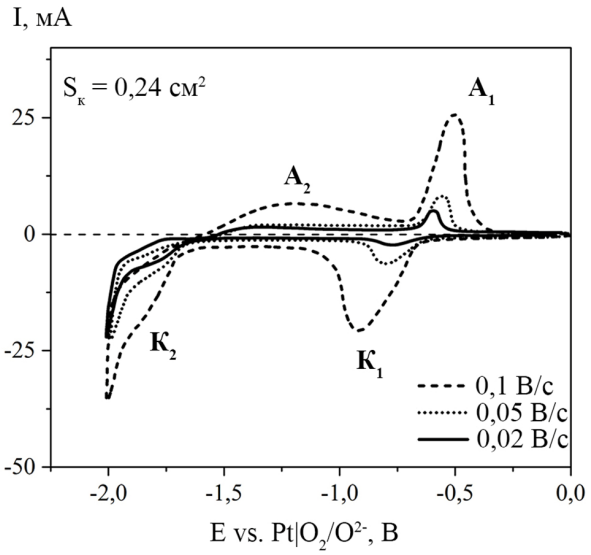

Рис. 4. Вольтамперограми розплавленої суміші Na,K|Cl–Li_2CO_3 ($0{,}75\times10^{-3}$ моль/см³) за різних швидкостей сканування. t = 750 °C; $S_к$ = 0,24 см²; атмосфера повітря

Дещо інший характер мають вольтамперограми відновлення Li_2CO_3 в атмосфері аргону та вуглекислого газу під тиском. За концентрації Li_2CO_3 $0{,}75\times10^{-3}$ моль/см³ у розплаві на вольтамперограмах в атмосфері аргону (рис. 5, *а*) фіксують лише одну катодну ($E_{п/2}$ = -1,5 В) хвилю K_2, а на зворотному ході розгортки потенціалу відповідну їй анодну A_2 ($E_{п/2}$ = -0,7 В) хвилю (потенціали вказано відносно Pb|$PbCl_2$ ЕП). За зміни атмосфери з повітря на CO_2 і поступовому збільшенні його тиску над розплавом (рис. 5, *б*) висота хвилі K_1 зменшується і за тиску 0,5 МПа її практично не реєструють, у той час як висота хвиль K_2 і A_2 збільшується.

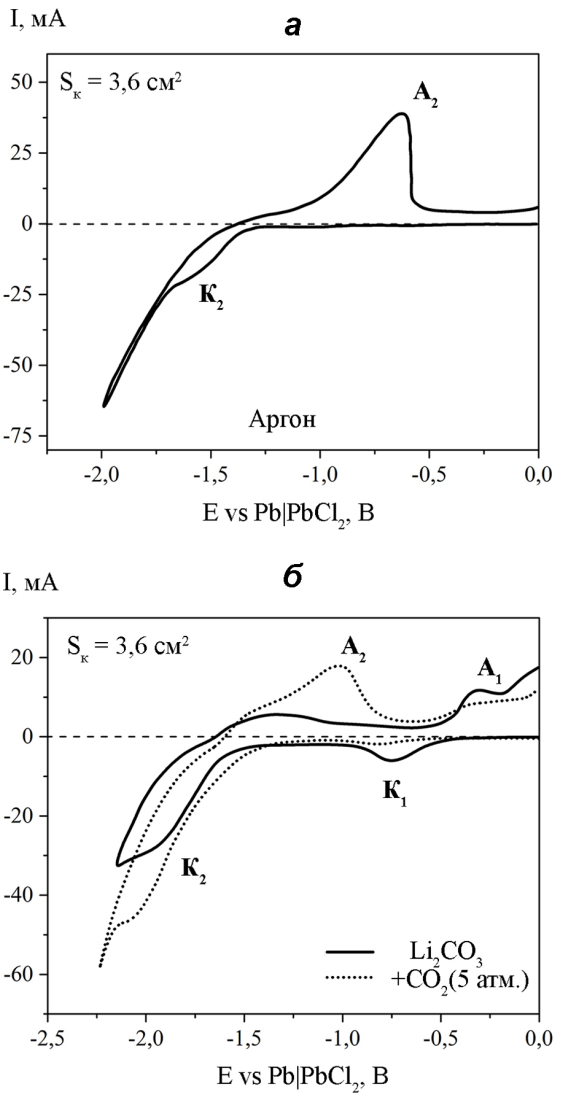

Рис. 5. Вольтамперограми розплавленої суміші Na,K|Cl–Li_2CO_3 ($0{,}75\times10^{-3}$ моль/см³) в атмосфері аргону (*а*), повітря та вуглекислого газу за тиску 0,5 МПа (*б*). t = 750 °C, V = 0,1 В/с, $S_к$ = 3,6 см², Pb|$PbCl_2$ ЕП.

ISSN 2708-129X. Укр. хім. журн., 2021

Із метою ідентифікації продуктів електровідновлення (природи катодних хвиль) проведено потенціостатичні електролізи (t = 750 °C) за потенціалів E_1 = -1,0 В ($i_{к1}$ = 0,08 А/см^2) та E_2 = -1,8 В ($i_{к2}$ = 0,15 А/см^2) на повітрі. В обох випадках після електролізу тривалістю 2 години на катоді утворювалися темні сольові «груші» – тверда суміш продуктів електролізу та електроліту (рис. 6, *а*). Сольова складова «груші» добре розчинялася у гарячій дистильованій воді, при цьому на дні стакана залишався дисперсний чорний порошок, який відмивали при кип'ятінні до негативної реакції на хлорид-йон. Отриманий порошок сушили за температури 105–130 °C на повітрі.

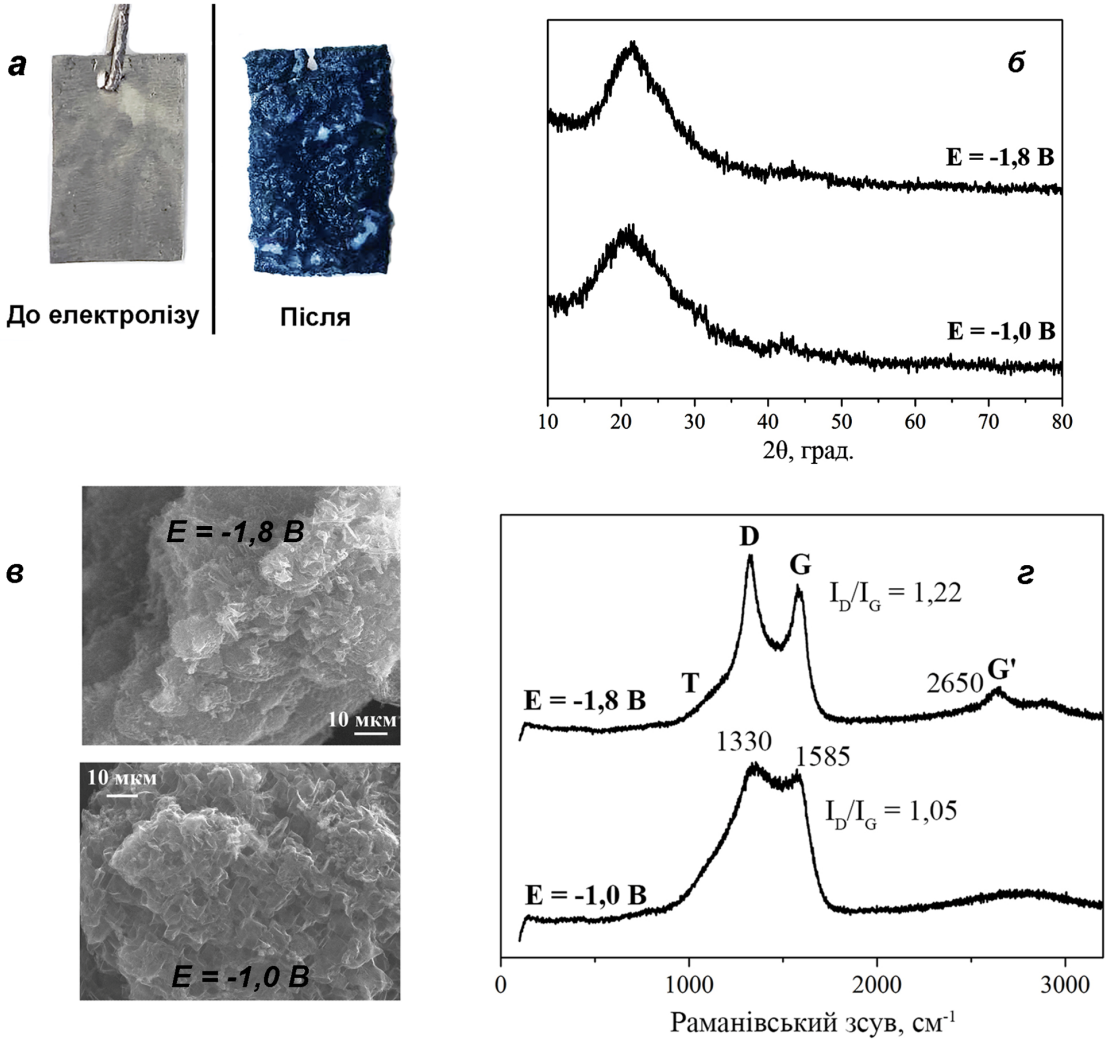

Рис. 6. Фото Pt катода до та після електролізу (*а*), рентгенівські дифрактограми (*б*), СЕМ-зображення (*в*) та Раман-спектри (*г*) катодних продуктів, одержаних електролізом розплавленої суміші Na,K|Cl–Li_2CO_3 (2×10^{-3} моль/см^3) при потенціалах, що відповідають різним хвилям вольтамперограм за температури 750 °C.

Методом РФА (рис. 6, *б*) встановлено, що катодний продукт в обох випадках – аморфний вуглець. Про аморфність вуглецю свідчить той факт, що на дифрактограмах реєструють розмитий (за 2θ–21°) та слабковиражений (за 43°) піки (гало), характерні для аморфно-кристалічного вуглецю (графіту).

Морфологію та структуру електролітичних порошків вуглецю вивчали методами СЕМ та КР-спектроскопії. Із зображень СЕМ (рис. 6, *в*) видно, що агломеровані частинки складаються з деградованих графітових структур. Загальний вигляд нагадує модель «пом'ятого паперу».

Методом КРС встановлено, що вуглець, який одержаний за різних потенціалів (-1,0 та -1,8 В), має високу розупорядкованість (дефектність). На це вказує висока інтенсивність піку D (частота 1318–1327 $см^{-1}$), який пов'язаний з порушенням графенової структури, а також високі значення співвідношення інтенсивності піків D та G (рис. 6 *г*). Середній розмір кристалітів вуглецевого продукту складає 30–40 нм (розраховано за формулою Tuinstra – Koenig [19]).

Відміни у морфології (рис. 6, *в*), характер Раман-спектрів *(*рис. 6, *г)* продуктів відновлення дають підстави вважати, що за зазначених умов (різниця потенціалів відновлення 0,8 В) вуглець утворюється на катоді з 2-х різних електрохімічно активних частинок (ЕХАЧ).

На основі аналізу цих експериментальних даних можна запропонувати наступний механізм електровідновлення Li_2CO_3 у хлоридному розплаві.

Перша катодна хвиля K_1 відповідає електровідновленню CO_2. Цей процес можна описати загальним рівнянням (1):

$$3CO_2 + 4\bar{e} \rightarrow C + 2CO_3^{2-}. \quad (1)$$

CO_2 утворюється в результаті термічної дисоціації Li_2CO_3 за хімічною реакцією (2), спрощене рівняння якої можна записати в іонному вигляді (3):

$$Li_2CO_3 \rightleftarrows Li_2O + CO_2 \quad (2)$$

$$CO_3^{2-} \rightleftarrows CO_2 + O^{2-}. \quad (3)$$

Рівноваги (2) і (3) чутливі до змін газового середовища над розплавом, оскільки в інертному середовищі аргону та в атмосфері CO_2, на вольтамперограмах (рис. 5) фіксують лише катодну хвилю K_2 ($E_{п/2}$ = -1,5 В) і відповідну їй анодну хвилю A_2 ($E_{п/2}$ = -0,7 В), а хвилі K_1 та A_1 відсутні. Відсутність цих хвиль пояснюється тим, що при зміні атмосфери відбувається зміщення рівноваг (2) і (3) у ліву сторону.

За потенціалу катодної хвилі K_2 відбувається електровідновлення Li_2CO_3 (ЕХАЧ – $Li_xCO_3^{2-x}$) з утворенням вуглецю за реакцією (4):

$$CO_3^{2-} + 4\bar{e} \rightarrow C + 3O^{2-}. \quad (4)$$

Це підтверджено літературними даними. Делімарський Ю. К. із співр. [20] при дослідженні електровідновлення Li_2CO_3 у хлоридному розплаві на повітрі, методами осцилографічної полярографії та хронопотенціометрії припустили, що процес електровідновлення CO_3^{2-} є ступінчастим із попередньою кінетичною реакцією кислотно-основного типу. Підтвердженням цього факту також є робота колективу авторів Кунмінського університету науки і технологій [21]. Методом термогравіметрії вони встановили, що процес дисоціації карбонату літію дуже залежить від атмосфери, в якій проводять розкладання.

Підтвердженням зроблених висновків можна також вважати результати робіт [6–16], оскільки на вольтамперограмах,

отриманих авторами зазначених статей, у розплавах, що містять карбонат літію, зафіксовано катодні хвилі, які відповідали утворенню вуглецевих структур за потенціалів, близьких до встановлених нами. На відміну від виконаних нами досліджень, автори робіт [6–16] експерименти проводили лише в атмосфері аргону, тому катодну хвилю K_1 не реєстрували.

Як вказано вище, електрохімічні процеси (1) та (4) є незворотними, оскільки потенціал обох хвиль зі зміною швидкості сканування змінюються, а також різниця між потенціалами ($E_{пK1}$ - $E_{пA1}$) і ($E_{пK2}$ - $E_{пA2}$) значно більша, ніж для 4-х електронного оборотного переносу заряду.

За потенціалів анодних хвиль A_1 та A_2 відбуваються такі перетворення:

$$C + 2CO_3^{2-} \rightarrow 3CO_2 + 4\bar{e}, \quad (5)$$

$$C + 2O^{2-} \rightarrow CO_2 + 4\bar{e}. \quad (6)$$

Не виключено, що під час електролізу можна утворити карбід літію Li_2C_2 у результаті сумісного електровідновлення іонів літію та карбонату, який за температур, вищих за 650 °С, може розкладатися на літій і вуглець.

Вихід вуглецю за струмом при електролізі становив 40–60%. Це могло бути наслідком втрат при відмиванні продуктів відновлення водою (не більше 3–5 мас.%); побічних реакцій на катоді: хімічним відновленням карбонат-йонів (CO_3^{2-} + C → CO_2 +CO) та/або вуглекислого газу (CO_2 +C → 2CO); окисненням на аноді одержаного вуглецю, оскільки електродні простори не ізольовані один від одного.

ВИСНОВКИ. Електрохімічне відновлення карбонату літію є складним процесом, що супроводжується низкою можливих побічних реакцій. Перебіг цього процесу (склад ЕХАЧ та область потенціалів відновлення) залежить від атмосфери газового середовища над розплавом і протікає в повітряній атмосфері через стадію попередньої хімічної реакції кислотно-основного типу з утворенням електрохімічно активних частинок CO_2 і $Li_xCO_3^{2-x}$, які відновлюються за різних потенціалів: –0,8 та –1,7 В ($Pb|PbCl_2$ ЕП) відповідно. В атмосфері аргону та вуглекислого газу за великого тиску процес протікає через утворення катіонного комплексу $Li_xCO_3^{2-x}$, який відновлюється до вуглецю.

Ця публікація підтримана джерелом фінансування Національної академії наук України № 0118U003438.

PECULIARITIES OF ELECTROREDUCTION OF Li_2CO_3 IN THE EQUIMOLAR MELT OF SODIUM AND POTASSIUM CHLORIDES

I.A. Novoselova[1*], S.V. Kuleshov[1], A.O. Omel'chuk[1], V.M. Bykov[2], O.M. Fesenko[2]

[1]V. I.Vernadsky Institute of General and Inorganic Chemistry of National Academy of Sciences of Ukraine, 32/34 Academic Palladin Avenue, Kyiv, 03142, Ukraine

[2]Institute of Physics of National Academy of Sciences of Ukraine, 46 Nauky Avenue, Kyiv, 03032, Ukraine

** e-mail: iness@ionc.kar.net, inessa_nov@ukr.net*

Recently, preparation of carbon materials by molten salt electrolysis has been demonstrated as a promising way of carbon capture, utilization and storage. This paper discusses the results of studies on the mechanism of carbon electrodeposition reactions in molten carbonate salts, especially voltammetric investigations. A CV study of the electroreduction of Li_2CO_3 against the background electrolyte NaCl–KCl was carried out. It was found that the electroreduction of Li_2CO_3 to carbon occurs through the stage of a preliminary chemical reaction of acid-base type with forming of electrochemically active particles – CO_2 and $Li_xCO_3^{2-x}$ at potentials of -0.8 and -1.7 V (against Pb|PbCl2 reference electrode), respectively. Both processes are irreversible, and the electroreduction of $Li_xCO_3^{2-x}$ takes place with diffusion control of the delivery of the depolarizer to the electrode surface. Electrolysis of melts have been carried out under potentiostatic conditions in an air atmosphere at different potentials (E = -1.0 and -1.8 V) at the temperature 750°C. The product yield was 40–60%. Compositions, morphological and structural peculiarities of carbon products have been studied by XRD analyses, SEM and Raman spectroscopy. XRD study shows that a symmetrical halo occurs at 2θ ~21 and 43°, suggesting that obtained carbon materials are amorphous. The ratio of the intensities of D and G bands (I_D/I_G) on Raman spectra was > 1 that indicates the extent of defects and impurities in the electrolytic carbon or the presence of ultrathin carbon. Agglomerated particles consist of degraded graphite structures with an approximate crystallite size of 30–40 nm. Their general appearance resembles the model of "crumpled paper".

The electroreduction of Li_2CO_3 to carbon in molten salts presented in this study is environmentally benign and affordable, providing a promising route for the production carbon nanomaterials. Also, this work highlights the possibility of using Li_2CO_3 as a precursor of high-temperature electrochemical synthesis of various carbonaceous materials, in particular, tungsten carbides.

Keywords: lithium carbonate, electroreduction, molten salts, carbon nanomaterials.

ЛІТЕРАТУРА

1. Hughes M. A., Allen J. A., Donne S. W. Carbonate reduction and the properties and applications of carbon formed through electrochemical deposition in molten carbonates: a review. *Electrochimica Acta*, 2015. **176**. P. 1511–1521.
2. A carbon science perspective in 2018: Current achievements and future challenges / A. Bianco et al. *Carbon*, 2018. **132**. P. 785–801.
3. Yin H., Wang, D. Electrochemical valorization of carbon dioxide in molten salts. *Materials and Processes for CO_2 Capture, Conversion, and Sequestration* / eds. L. Li, W. Wong-Ng, K. Huang, L.P. Cook. John Wiley & Sons, Inc., 2018. P. 267–295.
4. Mechanistic approach of the electrochemical reduction of CO_2 into CO at a gold electrode in molten carbonates by cyclic voltammetry / D. Chery et al. *International journal of hydrogen energy*, 2016. **41** (41) P. 18706–18712.
5. Transformation of the greenhouse gas carbon dioxide to graphene / X. Liu et al. *Journal of CO_2 Utilization*, 2020. **36**. P. 288–294.

6. Electrochemical formation of carbon nano-powders with various porosities in molten alkali carbonates / K. Le Van et al. *Electrochimica Acta*, 2009. **54** (19). P. 4566–4573.
7. Thermodynamic and experimental approach of electrochemical reduction of CO_2 in molten carbonates. / D. Chery, V. Albin, L. Lair, M. Cassir. *International Journal of Hydrogen Energy,* 2014. 39 (23). P. 12330–12339.
8. Molten salt CO_2 capture and electro-transformation (MSCC-ET) into capacitive carbon at medium temperature: effect of the electrolyte composition / B. W. Deng et al. *Faraday Discussions*, 2016. **190**. P. 241–258.
9. Sustainable carbons and fuels: recent advances of CO_2 conversion in molten salts / A. Yu et al. *ChemSusChem*, 2020. **13** (23). P. 6229–6245.
10. Chery D., Lair V., Cassir M. Overview on CO_2 valorization: challenge of molten carbonates. *Frontiers in Energy Research*, 2015. **3**. P. 1–10.
11. Ijije H. V., Chen G. Z. Electrochemical manufacturing of nanocarbons from carbon dioxide in molten alkali metal carbonate salts: roles of alkali metal cations. *Advances in Manufacturing*, 2016. **4**. P. 23–32.
12. Electrochemical graphitization conversion of CO_2 through soluble $NaVO_3$ homogeneous catalyst in carbonate molten salt / Y. Chen et al. *Electrochimica Acta*, 2019. **331**. P. 135461.
13. Electrochemical deposition of carbon in LiCl–NaCl–Na_2CO_3 melts / J. B. Ge et al. *Carbon*, 2016. **98**. P. 649–657.
14. Hughes M. A., Allen J. A., Donne S. W. The properties of carbons derived through the electrolytic reduction of molten carbonates under varied conditions: Part I. A study based on step potential electrochemical spectroscopy. *Journal of The Electrochemical Society*, 2018. **165** (11). P. A2608–A2624.
15. Deng B., Tang J., Gao M. Electrolytic synthesis of carbon from the captured CO_2 in molten LiCl–KCl–$CaCO_3$: Critical roles of electrode potential and temperature for hollow structure and lithium storage performance. *Electrochimica Acta*, 2018. **259**. P. 975–985.
16. Wang X., Liu X., Licht G., Licht S. Exploration of alkali cation variation on the synthesis of carbon nanotubes by electrolysis of CO_2 in molten carbonates. *Journal of CO_2 Utilization*, 2019. **34**. P. 303–312.
17. Delahay P. Theory of irreversible waves in oscillographic polarography. *Journal of American Chemical Society*, 1953. **75** (5). P. 1190–1196.
18. Matsuda H., Ayabe Y. Zur Theorie der Randles-Sevcik schen Kathodenstrahl-Polarographie. *Zeitschrift fuer Elektrochmie and Angewandte Physikalische Chemie*, 1955. **59** (6). P. 494–503.
19. Cançado L. G., Takai K., Enoki T. General equation for the determination of the crystallite size L_a of nanographite by Raman spectroscopy. *Applied Physics Letters*, 2006. **88** (16). P. 163106.
20. Делимарский Ю. К., Шаповал В. И., Василенко В. А. Значение кинетического процесса при электровосстановлении CO_3^{2-} в расплавленном KCl–NaCl. *Электрохимия*, 1971. **7** (9). С. 1301–1304.
21. Shi L., Qu T., Liu D., Deng Y., Yang B., Dai Y. Process of thermal decomposition of lithium carbonate. *Materials Processing*

Fundamentals / eds. J. Lee et al. Springer, Cham, 2020. P. 107–116.

REFERENCES

1. Hughes, M.A., Allen, J.A. and Donne, S.W. (2015). Carbonate Reduction and the Properties and Applications of Carbon Formed Through Electrochemical Deposition in Molten Carbonates: A Review. *Electrochimica Acta*. 176: 1511–1521.
2. Bianco, A., Chen, Y., Chen, Y., Ghoshal, D., Hurt, R.H., Kim, Y.A., Koratkar, N., Meunier, V. and Terrones, M. (2018). A carbon science perspective in 2018: Current achievements and future challenges. *Carbon*. 132: 785–801.
3. Yin, H. and Wang, D. (2018). 'Electrochemical Valorization of Carbon Dioxide in Molten Salts', in Li, L., Wong-Ng, W., Huang, K. and Cook, L.P. (eds.) *Materials and Processes for CO_2 Capture, Conversion, and Sequestration*. https://doi.org/10.1002/9781119231059.ch6
4. Chery, D., Albin, V., Meléndez-Ceballos, A., Lair, V. and Cassir, M. (2016). Mechanistic approach of the electrochemical reduction of CO_2 into CO at a gold electrode in molten carbonates by cyclic voltammetry. *International Journal of Hydrogen Energy*. 41(41): 18706–18712.
5. Liu, X., Wang, X., Licht, G. and Licht, S. (2020). Transformation of the greenhouse gas carbon dioxide to graphene. *Journal of CO_2 Utilization*. 36: 288–294.
6. Le Van, K., Groult, H., Lantelme, F., Dubois, M., Avignant, D., Tressaud, A., Komaba, S., Kumagai, N. and Sigrist, S. (2009). Electrochemical formation of carbon nano-powders with various porosities in molten alkali carbonates. *Electrochimica Acta*. 54(19): 4566–4573.
7. Chery, D., Albin, V., Lair, V. and Cassir, M. (2014). Thermodynamic and experimental approach of electrochemical reduction of CO_2 in molten carbonates. *International Journal of Hydrogen Energy*. 39(23): 12330–12339.
8. Deng, B., Chen, Z., Gao, M., Song, Y., Zheng, K., Tang, J., Xiao, W., Mao, X. and Wang, D. (2016). Molten salt CO_2capture and electro-transformation (MSCC-ET) into capacitive carbon at medium temperature: effect of the electrolyte composition. *Faraday Discussions*. 190: 241–258.
9. Yu, A., Ma, G., Ren, J., Peng, P. and Li, F. (2020). Sustainable Carbons and Fuels: Recent Advances of CO_2 Conversion in Molten Salts. *ChemSusChem*. 13(23): 6229–6245.
10. Chery, D., Lair, V. and Cassir, M. (2015). Overview on CO_2 Valorization: Challenge of Molten Carbonates. *Frontiers in Energy Research*. 3: 1–10.
11. Ijije, H.V. and Chen, G.Z. (2015). Electrochemical manufacturing of nanocarbons from carbon dioxide in molten alkali metal carbonate salts: roles of alkali metal cations. *Advances in Manufacturing*. 4(1): 23–32.
12. Chen, Y., Wang, M., Lu, S., Tu, J. and Jiao, S. (2020). Electrochemical graphitization conversion of CO_2 through soluble $NaVO_3$ homogeneous catalyst in carbonate molten salt. *Electrochimica Acta*. 331:135461.
13. Ge, J., Wang, S., Hu, L., Zhu, J. and Jiao, S. (2016). Electrochemical deposition of carbon in LiCl–NaCl–Na_2CO_3 melts. *Carbon*. 98: 649–657.

14. Hughes, M.A., Allen, J.A. and Donne, S.W. (2018). The Properties of Carbons Derived through the Electrolytic Reduction of Molten Carbonates under Varied Conditions: Part I. A Study Based on Step Potential Electrochemical Spectroscopy. *Journal of The Electrochemical Society*. 165(11): A2608–A2624.
15. Deng, B., Tang, J., Gao, M., Mao, X., Zhu, H., Xiao, W. and Wang, D. (2018). Electrolytic synthesis of carbon from the captured CO_2 in molten LiCl–KCl–$CaCO_3$: Critical roles of electrode potential and temperature for hollow structure and lithium storage performance. *Electrochimica Acta*. 259: 975–985.
16. Wang, X., Liu, X., Licht, G., Wang, B. and Licht, S. (2019). Exploration of alkali cation variation on the synthesis of carbon nanotubes by electrolysis of CO_2 in molten carbonates. *Journal of CO_2 Utilization*. 34:303–312.
17. Delahay, P. (1953). Theory of Irreversible Waves in Oscillographic Polarography. *Journal of the American Chemical Society*. 75(5):1190–1196.
18. Matsuda, H., Ayabe, Y. (1955) Zur Theorie der Randles-Sevcik schen Kathodenstrahl-Polarographie. *Zeitschrift fuer Elektrochmie and Angewandte Physikalische Chemie*. (59): 494–503.
19. Cançado, L.G., Takai, K., Enoki, T., Endo, M., Kim, Y.A., Mizusaki, H., Jorio, A., Coelho, L.N., Magalhães-Paniago, R. and Pimenta, M.A. (2006). General equation for the determination of the crystallite size L_a of nanographite by Raman spectroscopy. *Applied Physics Letters*. 88(16):163106.
20. Delimarskiy, Y. K., Shapoval, V.I., Vasilenko, V.A. (1971). Znachenie kineticheskogo processa pri jelektrovosstanovlenii CO_3^{2-} v rasplavlennom KCl–NaCl. *Soviet electrochemistry*. 7(9): 1301–1304 (in Russian).
21. Shi, L., Qu, T., Liu, D., Deng, Y., Yang, B. and Dai, Y. (2020) 'Process of thermal decomposition of lithium carbonate', in Lee, J., Wagstaff, S., Lambotte, G., Allanore, A., Tesfaye, F. (eds.) *Materials Processing Fundamentals*. Springer. Cham: 107–116.

Стаття надійшла 21.07.2021

UDC 544.6.018+544.35 doi: 10.33609/2708-129X.87.06.2021.82-96

MODERN RESEARCH METHODS OF PHYSICOCHEMICAL AND ELECTRO-CHEMICAL PROPERTIES OF ELECTROLYTES FOR Li-ION BATTERIES AND HYBRID SUPERCAPACITIES

V. A. Diamant

V. I. Vernadsky Institute of General & Inorganic Chemistry NAS Ukraine, Akad. Palladin Avenue, 32/34, 03680 Kyiv, Ukraine
e-mail: carbon.h.4@gmail.com

In review examinei base properties of modern non-aqueous electrolytes for Li-ion batteries and hybrid supercapacitors taking part in the formation of power density, electrochemical and thermal stability. Discussed such aspects as the electrolytes functions in electrochemical power sources, physicochemical and electrochemical properties of electrolytes for supercapacitors, the physicochemical and electrochemical properties of electrolytes for primary and secondary batteries, and methods of electrolytes research. As the base methodi for electrolytes studies considered: electrochemical impedance spectroscopy, voltammetry, amperometry, viscosimetry, and combined Ramman spectroscopy.

Key words: electrolyte, non-aqueous solvent, operating life, impedance, voltammetry, viscosity, conductivity.

INTRODUCTION. Modern electrolytes are complex physico-chemical systems which properties are formed by all components of these systems. Hence, receiving new knowledge about interactions between components of electrolytes could give the ability to move the properties of electrolytes according to their application. Today, we have a rather limited amount of methods to study the physicochemical and electrochemical properties of modern electrolytes. These are classical methods of density measurement [1–4], scanning calorimetry [5–8], thermal gravimetric analysis (TGA) [9–11], and electrochemical methods: conductivity measurement [12–14], cyclic voltammetry [15–16], and electrochemical impedance spectroscopy [17–18]. The study of electrolyte systems in – situ is a more difficult task because it needs non-destructive physicochemical and electrochemical control methods [19–20] and is closely connected with the functions of electrolytes in electrochemical power sources and energy storages. In dependences of these functions, the research methods could be changed. For a better understanding of the ability of methods, it is necessary to know the differences in these functions according to various types of energy storage/power sources. Also, the great interest performs impact of solvent or mixture of solvents on ending properties of such

electrochemical systems. So, the main aim of this review is to combine specific tasks for the control of working parameters of batteries or capacitors with properties of electrolytes.

The electrolytes functions in electrochemical power sources (EPS). The charge transfer is the base function of electrolytes in chemical power sources. The conductivity y of electrolyte forms by the ion transfer component. The component with an electron transfer function contributing to the self-discharge of the element. The basic requirements for the electrolytes in all cases are:

– high ionic conductivity;

– electrochemical stability window of at least 4.5 V on a platinum electrode

– temperature range of the electrochemical window in the liquid state from - 60 °C to + 60 °C;

– no corrosion activity happening to structural materials (aluminum and copper current collectors, steel housing, etc.) [21].

Some particular requirements exist only for supercapacitors. Their electrochemical capacity depends on the number of charges, so very concentrated electrolytes and the use of ionic liquid lead to better performance. The region of electrochemical stability on the electrolyte plate narrows down from 4.5 V to 2.5 V, when the working material is replaced with porous carbon. Therefore, for the electrolyte used in the supercapacitor, the following characteristics decrease: the electrochemical stability window is not less than 2.5 V by solubility - 0.9 M and more [22–23].

Physiochemical and electrochemical properties of electrolytes for supercapacitors. Often, for the preparation of the electrolyte, conventional solvents such as acetonitrile, propylene carbonate, and other carbonate solvents and their mixtures are used [23–24]. Last year, the solutions of tetrafluoroborate tetraethylammonium in acetonitrile are implemented in batteries manufacturing and the researcher domain. The last is charged up to the capacity of 2.5 V [23–28]. This salt has high electrochemical (~ 2.8 V on carbon) [26] and thermal stability (320 °C) [27]. But it is expensive to produce and highly toxic at the same time. Also, the hydrolysis with traces of water and fluorine-containing anion results in HF, which can lead to corrosion of the hull and the current collector. Therefore, the search for cheap, easy to manufacture, and environmentally friendly analogs of this salt is highly relevant.

Other types of known electrolytes are based on ionic liquids [29, 30, 31] and polymer electrolytes [22–24, 29]. They create a low vapor pressure, simplifying the assembly stage of the power source and providing fire safety.

The physicochemical and electrochemical properties of electrolytes for primary and secondary batteries. The properties of an electrolyte flow in the batteries are of great importance since it is the main way to transport the reagents to the electrodes. Thus, it affects the operational reliability of the entire electrochemical system. The requirements for electrolytes are simplified and do not change during the last decades for the primary power sources in the presence of irreversible chemical reactions [32]. In contrast to primary, the secondary power sources can cycle. The secondary power sources need a higher electrochemical (operating potential range) and thermal (operating temperature range) resistance to ensure high operating life. Modern electrolytes have sufficiently high values of the potentials operating range (3.5–5.1 V) [33–40]. Salt components have significant thermal stability (100–400 °C) (Table 1) [33–40].

Table 1

Composition, operating temperature range, and potentials operating range of commercial and laboratory electrolytes for secondary power sources.

Salt component	T, ˚C	Electrochemical stability (solvent in which it was measured)	Literature cited
$LiClO_4$	400 °C	5.1 V (propylene carbonat	[33, 34],
$LiAsF_6$	340 °C	4,5 B propylene carbonate	[33, 35]
$LiBF_4$	293 °C	5.0 V (propylene carbonate)	[33, 35]
$LiPF_6$	30 °C – 117 °C	4.5 V (propylene carbonate)	[41, 36, 35, 33]
Lithium triflate	300 °C	5,1 B (sulpholane)	[33], [37], [38 p. 318],
propylene carbonate	360 °C	5,0 V (propylene carbonate)	[42], [37], [38 p. 318], [39]
Lithium Methanide	340 °C	4.0 V (tetrahydrofuran)	[39]
$LiSO_3F$	360 °C	4.9 V (γ-butyrolactone)	[40]

Table 2

Electroconductivity of the lithium salts in aprotic solvents.

σ, mCm*Cm^{-1}	$LiBF_4$	$LiPF_6$	$LiAsF_6$	$LClO_4$	$LiCF_3SO_3$	$LiN(SO_2CF_3)_2$	Literature cited
(1.0 M 25 °C) in ПК	3.4	5.8	5.7	5.6	1.7	5.1	[33], [35]
(1.0 M 25 °C) in ЕК/DMK	4.9	10.7	11.1	8.4		9.0	[33], [35]
(1,0 M 25 °C) in PC / DME	9.46	15.3	14.8	13.5	6.12	12.6	[35]

Nowadays, the industry samples contained mainly lithium compounds that have some operational problems. For example, $LiClO_4$ solutions in organic solvents can explode during exploitation [33]. $LiAsF_6$ and its decomposition products are toxic. $LiAsF_6$ and $LiBF_4$, $LiPF_6$ are sensitive to hydrolysis since their products - PF_5, BF_3, and AsF_5 initiate solvents polymerization. In addition, these reactions result in lithium fluoride, which stimulates the creation of a blocking film with cyclic carbonate on the electrodes [43, 37]. The other disadvantages typical for these fluorinated salts are high cost, limited use with cathode materials based on manganese spinel, and environmental hazards. But, despite the pointed problems, LiPF6 remains today the most common salt for liquid electrolytes in lithium-ion batteries with

different cathode and anode materials [43]. Although $LiPF_6$ begins to decompose by temperatures above 30 °C, even being in an electrolyte [41, 36, 35, 33].

Also, $LiSO_3F$ does not dissolve in solvents which have proved to be efficient for lithium EPS. The lithium triflate solutions in non-aqueous solvents are inferior to other systems in terms of electrical conductivity. Lithium methanide and imide lead to corrosion of aluminum current collector [33, 37, 44].

Methods of electrolytes research. Analysis of the electrolytes features gives grounds to assert that CEI and CVA are the most informative methods for the study of electrochemical properties of electrolytes. For the determination of the ion's transportability of electrolyte, the density measurements are also actual.

Electrochemical impedance of lithium-ion battery. Spectroscopy of electrochemical impedance (SEI) has been promoted in recent years, and the number of objects under study is constantly growing. Many studies are used to understanding the processes into chemical power sources and their components. The electrochemical impedance spectroscopy could be used to study the battery as a whole [18, 4750, 54] or its parts (electrode or electrolyte) [20, 52, 5558]. Modeling allows us to understand the mechanisms of formation conductivity in liquid [55], solid and polymer electrolytes [57], colloidal solutions [52], and other heterogeneous systems. When modeling an electrolyte system and determining its elements, additional physical and chemical values such as the relaxation time of the system [18,56], and the diffusion coefficient (via calculating the Warburg impedance) should be identified. A very important aspect in research of lithium and sodium secondary power sources is to investigate the properties, formation, and functioning conditions of a solid protective film formed on cathode and anode materials after the first cycle due to the destruction of some electrolyte part [45-48, 50-51, 54]. The only possible way to carry out the study of this film without opening the battery is to construct an electrochemical model of the system, which will allow us to interpret the data obtained by electrochemical impedance spectroscopy and calculate the values of interest [47]. Most of the equivalent schemes constructed to explain the impedance of a lithium-ion battery follow one of the three examples (Fig.1) [17, 47]:

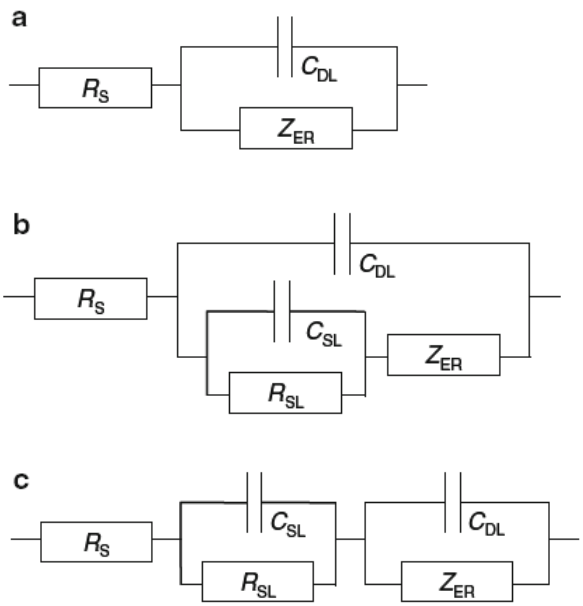

Fig. 1. Basic equivalent schemes of a lithium-ion battery: a unit model – without the solid passivation film on the surface of the electrode (a); 2 models – with the solid passivation film on the surface of the electrode materials (b, c). SL – indicates elements of the scheme associated with a solid passivation film, R_s – resistance of solution, C_{SL} – capacity of the passivation film, R_{SL} – resistance of the passivation film, C_{DL} – capacity of the double electric layer, Z_{ER} – boundary impedance.

As a rule, we have to consider the formation of a passivation film on the metal surface of the current collector (or often oxide corrosive film) and the formation of a solid electrolyte film on the surface of the cathode and anode material, as well as the formation of a double electric layer [47]. Models of this type are given in Fig. 2.

According to [46], model equivalent circuit diagrams of the battery before discharge and after may differ significantly (Fig. 3)

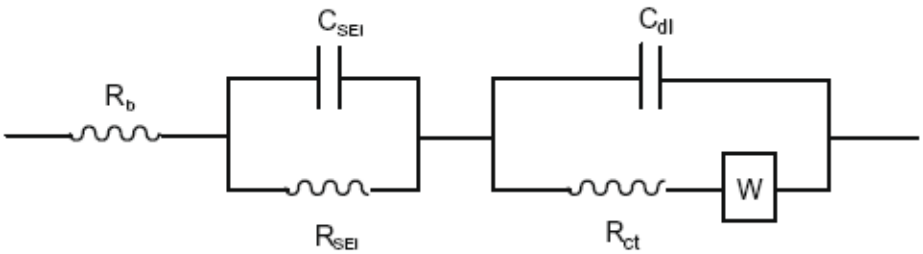

Fig. 2. Equivalent circuit diagram of the battery, considering the corrosion film on the surface of the current collector and the solid electrolyte film on the surface of the electrode material [45]. W – the Warburg element, Rb – resistance of the electrolyte, R_{SEI} – resistance of the passivation film, Rct – resistance of cathode, C_{SEI} – capacity of the passivation film, C_{dl} – capacity of the double electric layer.

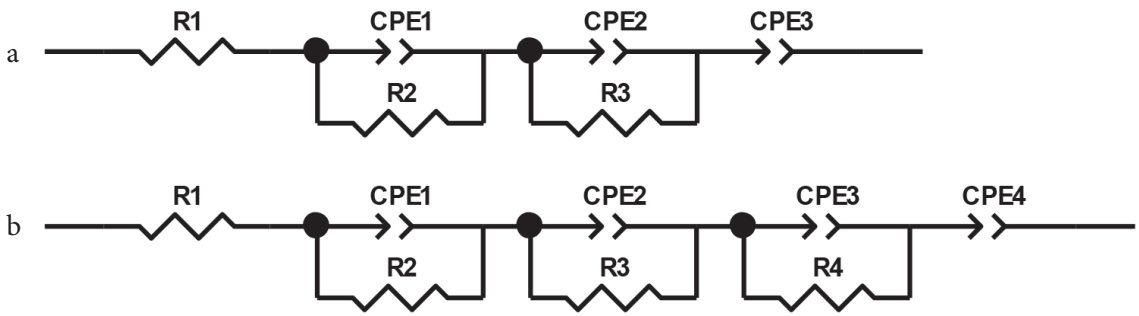

Fig. 3. Model equivalent circuits of the battery before discharge (a) and after discharge (b) [46].

This model has more than two constant phase elements connected with "capacitance dispersion" due to electrode porosity, surface roughness, and heterogeneities [19]. Also, such interpretation partially corresponds to the Voight's model for rubber-like materials (impedance at the local contact area between flexible surface film and electrode) [17, 59]. More reasonable is a model that takes into account the simultaneous transport of electrons and ions in the counterflow (Figure 4) [47]. More reasonable is a model, that takes into account the simultaneous transport of electrons and ions in the counterflow (Figure 4), [47]. Among all the mentioned examples, R_{SOL} elements and the double layer capacity of CSL / SOL could be attributed to the electrolyte component of the batteries because the electrolyte is directly involved in the formation of a solid surface film and ionic conductivity.

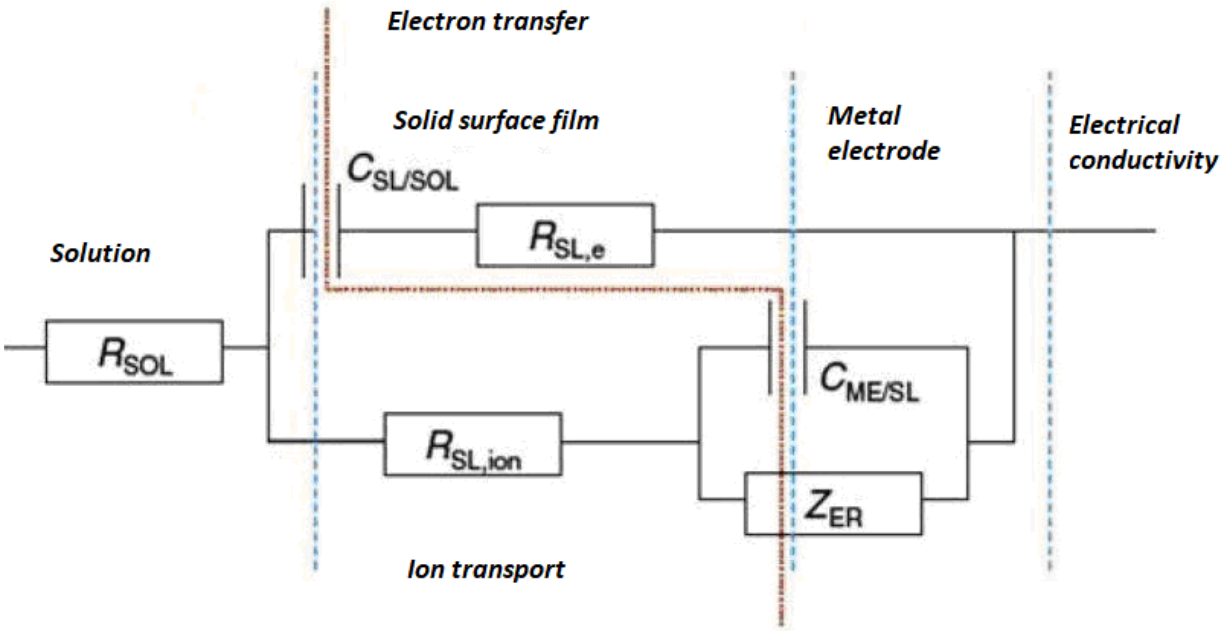

Fig. 4. Model equivalent circuit scheme of lithium-ion battery [47].

The conception of polymer electrolytes (PEs) is a highly specialized and multidisciplinary field that covers the disciplines of electrochemistry, polymer science, organic and inorganic chemistry. The good mechanical strength, ease of thin film fabrication with desirable shapes and the ability of forming good electrode/electrolyte contact are the main advantages of dry SPEs. The electrolyte scheme [17, 57–59] of a polymer electrolyte composed in a cell following the order Li | Polymer | Li is simpler (Fig. 5.). This equivalent circuit consists of two shunted CPE elements and closely connects with electrode porosity [19].

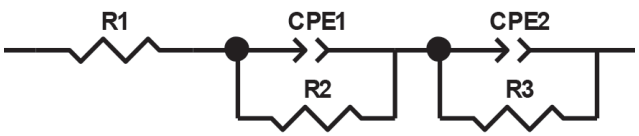

Fig. 5. Equivalent circuit of polymer electrolyte [58].

Attempts to construct equivalent models of primary power sources (lithium), sodium-ion battery, lead, Nickel-cadmium, Nickel-metal hydride batteries, and their electrodes are also reviewed [60]. All the described models need to be revised and refined.

Thus, the modeling of electrolyte systems is carried out periodically, in general, use the universal model [17]. We find this approach fundamentally wrong, as it does not consider the relationship between conductivity mechanism and the electrolyte aggregate state, as well as the dissolved salt-solvent interaction. However, these relationships form the prerequisites for changing the conductivity mechanisms.

Another method, often used in addition to modeling equivalent circuit diagrams, is the direct measurement of the active impedance component. However, the imaginary part of the impedance also has a significant effect due to thermal stress. It depends not only on the

capacity of the double electric layer on the electrode surface but also on the change in its structure after chemical transformations. It is formed due to the diffusion of ions, which is increasingly fixed in the low-frequency range. Therefore, the high-frequency range is not always advisable, since at a frequency above 103 Hz the diffusion of the ions will be blocked [61].

So, EIS could be used to study electrolytes properties *in-situ* without the destruction of batteries and separately to detect their properties during contact with the electrode surface.

Voltammetry of electrolytes. The voltammetry method allows for the investigation of the overall electrochemical stability of the electrolyte and defines the so-called «electrochemical stability window» (the potentials interval where electrochemical processes are impossible), as well as the electrochemical reactions where the individual electrolyte components participate. Reference voltammetric studies are done on platinum electrodes, but the electrodes and current collectors used in real systems are made from copper, aluminum, and carbon. Therefore, voltammetric studies are carried out on noble metals – silver and gold, as well as on aluminum, copper, and glassy carbon [62]. The peaks of all these electrodes are associated with extraneous processes, such as oxygen reduction, reduction of the surface oxide film, reduction/oxidation of surface groups, etc [62]. The characteristic window of electrochemical stability of different classes of organic solvents with tetraalkylammonium (a) and a lithium background salt (b) are shown in Fig.6 [63]:

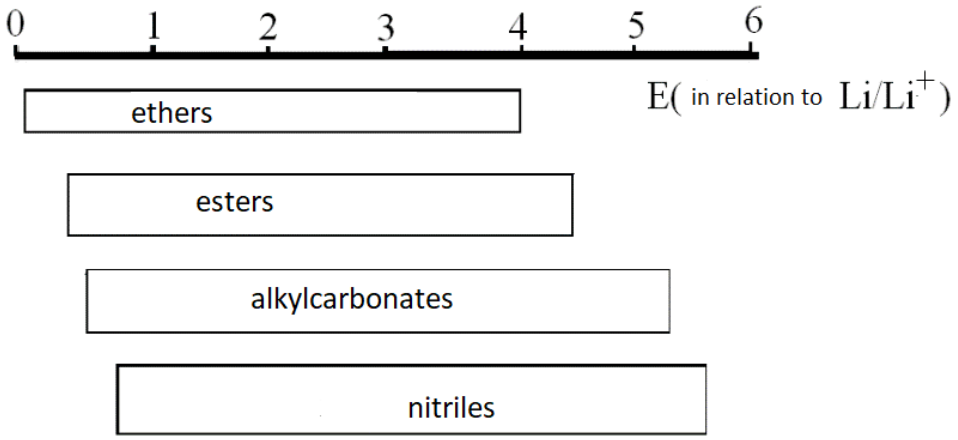

Fig. 6. The electrochemical stability of solvents.

Using voltammetry detected that many modern electrolytes have a low range of electrochemical stability. Their decomposition takes place at the potential range from 0,5–2 V. The typical products of solvent decomposition and the most popular in studies of background salts $LiClO_4$ and $LiPF_6$ are presented in Table 3. Moreover, it was shown the impact of salt anion on the electrochemical and temperature stability of electrolytes by voltammetry. In the case of the salicyl borate anion - the coordinate covalent bond in the aromatic nucleus has shifted the recovery peak to higher potentials (Table 4).

Table 3

The products of electrolyte decomposition [63].

Solvent and other components	Possible reduction products	Potential limit relative to Li/Li^+
O_2	LiO_2, Li_2O_2	1,5 – 2 V
H_2O	LiOH	1,5 – 1,2 V
HF PF_5	LiF, Li_xPF_y	1.8 and below
Eters	ROLi	Below 0,5 V
esters	ROCOOLi (carboxylates)	Below 1,2 V
alkylcarbonates	ROCOOLi, ROLi	Below 1,5 V
ethylene carbonate	CH_2(OCOOLi), CH_2=CH_2	Below 1,5 V
propylene carbonate	CH_3CH(OCOOLi), $CH_2OCOOLi$, CH_3CH=CH_2	Below 0,5 V
dimethyl carbonate	$CH_3OCOOLi$, CH_3OLi	Below 1.2 V
$LiClO_4$	LiCl, $LiClO_x$	Below 1 V
$LiPF_6$	LiF, Li_xPF_y	Below 1 V
$LiN(SO_2CF_3)_2$	LiF, $LiCF_3$, $LiSO_2CF_3$, $Li_2NSO_2CF_3$	Below 1 V

Table 4

Reduction in the first cycle of lithium bis(Saltillo)borate substitution in the aromatic nucleus to Galogen atom [64].

The salt components of the electrolyte	Recovery potential at the first cycle relative to Li/Li^+, V	The salt components of the electrolyte	Recovery potential at the first cycle relative to Li/Li^+, V
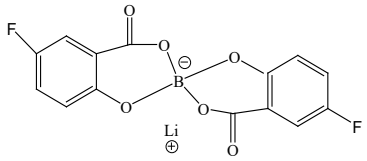	0.75 1.12 1.45	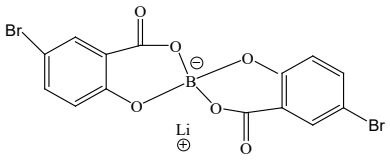	1.3
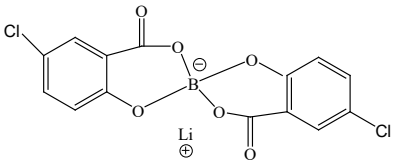	1.3 1.65	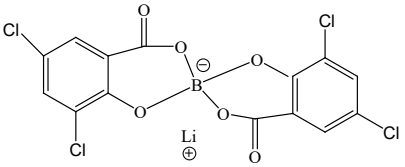	1.35

Measurements of densitometry and amperometry to evaluate the electrical conductivity of electrolytes. Known, that in non-aqueous solvents, the autoionization of the solvent, if protic, will be different to water, meaning that the ionization of these functional polymers will be different. In aprotic solvents, there will not be autoionizable protons, so solvent-solute proton transfer is not possible. The formation and stabilization of charges in non-polar low dielectric solvents is known to be challenging, and so it is not surprising that identifying ionic species in electrolytes is challenging. At another hand, introducing insulating phases into non-aqueous salt solution leads to remarkable conductivity enhancements, an effect ascribed to the breaking up of ion pairs. This new class of electrolytes combines the high ionic conductivities of liquids and the beneficial mechanical properties of soft matter [65].

Electrolyte viscosity is a macroscopic property, although its foundation lies on molecular-scale interactions between solvent and ionic species. A comprehensive understanding of viscosity behavior with respect to solvent composition, salt concentration and temperature is only possible with correct interpretations of molecular interactions and related quantities. For this purpose, the use of a combination of methods gives more corrective and informational results.

So, the following methods are widely used to study the physicochemical properties and conductivity of non-aqueous electrolytes: dielectrometry, differential scanning calorimetry, densitometry, viscometry and combined Raman spectroscopy [66]. Such studies found the ability to form solvat complexes of metal cations with solvent components. Analyzing these calculations could determine the nature of ion solvation and the mechanism of charge carrier growth depending on the salt concentration. The difference between the conductivity nature of the systems based on lithium and sodium was established. It depends upon the structure and charge of the metal complex. In systems based on Li+ electrolytes form a complex $[Li\ (TFSI)_2]^-$, whereas, in sodium systems, the dominant form is $[Na(TFSI)_3]^{2-}$ complexes. It directly relates to the density change and electrolytes conductivity, depending on the metal salt concentration.

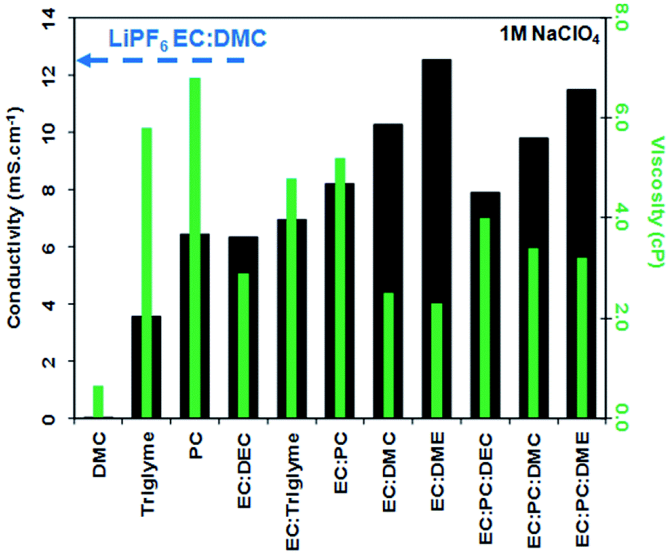

Fig. 7. Conductivity effect (black bands and axes of the left side of the axis) on the viscosity (green bands and the right side of the y axis) of electrolytes consisting fom 1 M $NaClO_4$ dissolved in various solvents and solvent mixtures [67].

The most informative is one hour study of the electrolyte's thermal behavior, ionic conductivity, and viscosity using inert and «real» electrodes. This approach allows optimizing the working electrolyte mixtures (salt and

solvent, to stabilize the film on the electrode surface, reduce polarization and achieve full power at a low potential plateau. For example, the relationship between conductivity, viscosity, and composition of the electrolyte system $LiPF_6$, on reference samples were investigated in various solvents. Results of measurements are shown in Fig. 7. There are no linear dependences in such systems, but the correlation between the optimal range of viscosity and maximum conductivity could be observed

Thus, the study of the temperature dependence of the conductivity on the salt concentration and electrolyte viscosity, dielectric properties of solvents and their mixtures can be a tool to select the optimal composition of electrolytes with high power in a wide range of potentials and a stable film on the electrode - electrolyte interface.

CONCLUSIONS. Spectroscopy of electrochemical impedance, voltammetry, amperometry with viscosimetry, and combined Ramman spectroscopy have been successfully used for the study properties of electrolytes necessary in the manufacturing of modern batteries and hybrid supercapacitors. They permit the analysis of properties that are difficult or even impossible to study by only one of these methods separately. EIS could be used to study electrolytes properties in-situ without the destruction of batteries and separately to detect their properties during contact with the electrode surface. The voltammetry method allows for the investigation of the overall electrochemical stability of the electrolyte and defines the so-called «electrochemical stability window» (the potentials interval where electrochemical processes are impossible), as well as the electrochemical reactions where the individual electrolyte components participate. The study of the temperature dependence of the conductivity on the salt concentration and electrolyte viscosity, dielectric properties of solvents and their mixtures can be a tool to select the optimal composition of electrolytes with high power in a wide range of potentials and a stable film on the electrode - electrolyte interface.

ACKNOWLEDGEMENTS. The authors will express thanks to the National Academy of Sciences of Ukraine for the financial support of this work.

СУЧАСНІ МЕТОДИ ДОСЛІДЖЕННЯ ФІЗИКО-ХІМІЧНИХ І ЕЛЕКТРОХІМІЧНИХ ВЛАСТИВОСТЕЙ ЕЛЕКТРОЛІТІВ У ЛІТІЙ-ЙОННИХ АКУМУЛЯТОРАХ ТА ГІБРИДНИХ СУПЕРКОНДЕНСАТОРАХ

В. А. Діамант

Інститут загальної та неорганічної хімії ім. В. І. Вернадського НАН України, просп. Акад. Палладіна, 32/34, 03680 Київ, Україна

e-mail: carbon.h.4@gmail.com

В огляді надано базові властивості сучасних неводних електролітів для літій-іонних акумуляторів та гібридних суперконденсаторів, які беруть участь у формуванні потужності, електрохімічної та

термічної стабільності. Обговорено такі аспекти, як функції електролітів в електрохімічних джерелах живлення, фізико-хімічні та електрохімічні властивості електролітів для суперконденсаторів, фізико-хімічні та електрохімічні властивості електролітів для первинних та вторинних батарей та методи дослідження електролітів. Як базові методи досліджень електролітів наведено: електрохімічну імпедансну спектроскопію, вольтамперометрію, амперометрію, віскозиметрію та комбіновану спектроскопію Рамана. Використання цих методів дозволяє аналізувати властивості, які важко або навіть неможливо вивчити за допомогою лише одного з цих методів. ЕІС можна використовувати для вивчення властивостей електролітів in-situ без руйнування батарей та окремо для виявлення їхніх властивостей під час контакту з поверхнею електрода. Метод вольтамперометрії дозволяє досліджувати загальну електрохімічну стабільність електроліту і визначає т. зв. «вікно електрохімічної стійкості» (інтервал потенціалів, де електрохімічні процеси неможливі), а також електрохімічні реакції, в яких беруть участь окремі компоненти електроліту. Вивчення температурної залежності провідності від концентрації солі та в'язкості електролітів, діелектричних властивостей розчинників та їхніх сумішей може бути інструментом для вибору оптимального складу електролітів із великою потужністю в широкому діапазоні потенціалів та стабільною плівкою на інтерфейс електрод – електроліт.

Ключові слова: електроліт, неводний розчинник, термін служби, імпеданс, вольтамперометрія, в'язкість, провідність.

REFERENCES

1. Millero F. J. Molal volumes of electrolytes. *Chemical Reviews*. 1971. **71**(2): 147–176.
2. Laliberte M., Cooper W. E. Model for calculating the density of aqueous electrolyte solutions. *Journal of Chemical & Engineering Data*. 2004. **49**(5): 1141–1151.
3. Li M., Wang C., Chen Z., Xu K., Lu J. New concepts in electrolytes. *Chemical reviews*. 2020. **120**(14): 6783–6819.
4. Lukatskaya M. R., Feldblyum J. I., Mackanic D. G., Lissel F., Michels D. L., Cui Y., Bao Z. Concentrated mixed cation acetate "water-in-salt" solutions as green and low-cost high voltage electrolytes for aqueous batteries. *Energy & Environmental Science*. 2018. **11**(10): 2876–2883.
5. Dalmazzone D., Clausse D., Dalmazzone C., Herzhaft B. The stability of methane hydrates in highly concentrated electrolyte solutions by differential scanning calorimetry and theoretical computation. *American Mineralogist*. 2004. **89**(8–9): 1183–1191.
6. Pehlivan İ. B., Marsal R., Niklasson G. A., Granqvist C. G., Georén P. PEI–LiTFSI electrolytes for electrochromic devices: Characterization by differential scanning calorimetry and viscosity measurements. *Solar energy materials and solar cells*. 2010. **94**(12): 2399–2404.
7. Zhang Z., Fouchard D., Rea J. R. Differential scanning calorimetry material studies: implications for the safety of lithium-ion cells. *Journal of power sources*. 1998. **70**(1): 16–20.
8. Sundaramahalingam K., Muthuvinayagam M., Nallamuthu N., Vanitha D.,

Vahini M. Investigations on lithium acetate-doped PVA/PVP solid polymer blend electrolytes. *Polymer Bulletin*. 2019. **76**(11): 5577–5602.
9. Nakajima H., Ohno H. Preparation of thermally stable polymer electrolytes from imidazolium-type ionic liquid derivatives. *Polymer*. 2005. **46**(25): 11499–11504.
10. Wilken S., Johansson P., Jacobsson P. Infrared spectroscopy of instantaneous decomposition products of $LiPF_6$-based lithium battery electrolytes. *Solid State Ionics*. 2012. **225**: 608–610.
11. Enotiadis A., Fernandes N. J., Becerra N. A., Zammarano M., Giannelis E. P. Nanocomposite electrolytes for lithium batteries with reduced flammability. *Electrochimica Acta*. 2018. **269**: 76–82.
12. Bešter-Rogač, M., & Habe, D. Modern advances in electrical conductivity measurements of solutions. *Acta chimica slovenica*. 2006. *53*(3).
13. Chintapalli M., Timachova K., Olson K. R., Mecham S. J., Devaux D., DeSimone J. M., Balsara N. P. Relationship between conductivity, ion diffusion, and transference number in perfluoropolyether electrolytes. *Macromolecules*. 2016. **49**(9): 3508–3515.
14. Valøen L. O., Reimers J. N. Transport properties of LiPF6-based Li-ion battery electrolytes. *Journal of The Electrochemical Society*. 2005.**152**(5): A882.
15. Muchakayala R., Song S., Wang J., Fan Y., Bengeppagari M., Chen J., Tan M. Development and supercapacitor application of ionic liquid-incorporated gel polymer electrolyte films. *Journal of industrial and engineering chemistry*. 2018. **59**: 79–89.
16. Li W., Zhang F., Xiang X., Zhang X. 2017. High-efficiency Na-storage performance of a nickel-based ferricyanide cathode in high-concentration electrolytes for aqueous sodium-ion batteries. *ElectroChem*. **4**(11): 2870–2876.
17. Impedance Spectroscopy. Theory, Experiment and Applications. /Ed. E. Barsoukov, J. Ross Macdonald. N.Y., Wiley. 2005. 616.
18. Riabokin O. L., Boichuk A. V., Pershina K. D. Control of the State of Primary Alkaline Zn–MnO_2 Cells Using the Electrochemical Impedance Spectroscopy Method. *Surface Engineering and Applied Electrochemistry*. 2018. **54**(6): 614–622.
19. Jean-Baptiste Jorcin, Mark E. Orazem, Nadine Pébère and Bernard Tribollet. CPE analysis by local electrochemical impedance spectroscopy. *Electrochimica Acta*. 2006. **51**(8–9): 1473–1479.
20. Pershina E.D., Burda V.E., Kazdobin K.A. *et al.* Identification of the sugars content in the production of champagne by the electrochemical impedance spectroscopy method. *Surf. Engin. Appl.Electrochem.* 2013. **49**: 348–354.
21. Etacheri, V., Marom, R., Elazari, R., Salitra, G., & Aurbach, D. Challenges in the development of advanced Li-ion batteries: a review. *Energy & Environmental Science*. 2011. **4**(9): 3243–3262.
22. Zhong, C., Deng, Y., Hu, W., Qiao, J., Zhang, L., & Zhang, J. A review of electrolyte materials and compositions for electrochemical supercapacitors. *Chemical Society Reviews*. 2015. **44**(21): 7484–7539.
23. Gao, H., & Lian, K. Proton-conducting polymer electrolytes and their applications in solid supercapacitors: a review. *RSC advances*. 2014. **4**(62): 33091–33113.
24. Sharma, K., Arora, A., & Tripathi, S. K. Re-

view of supercapacitors: Materials and devices. *Journal of Energy Storage*. 2019. **21**: 801–825.
25. Kieran M., Dunens O., Harris A. A review of carbon nanotube purification by microwave assisted acid digestion. *Separation and purification Technology*. 2009. **66**(2): 209–222.
26. Waldvogel S., Malkowsky I., Griesbach U., Pötter H. Novel fluorine-free electrolyte system for supercapacitors. *Electrochemistry Communications*. 2009. **11**(6): 1237–1241.
27. Nanbu N., Ebina T., Uno H., Ishizawa S. Physical and electrochemical properties of quaternary ammonium bis(oxalato) borates and their application to electric double-layer capacitors. *Electrochimica Acta*. 2006. **52**(4): 1763–1770.
28. Diamant V.A., Pershina E.D., Trachevsky V.V. *et al.* Physicochemical properties of tetramethylammonium bis(salicylo)borate. *Russ J Appl Chem.* 2015. **88**: 901–907.
29. Diamant V. A., Malovanyy S. M., Pershina K. D., Kazdobin K. A. Electrochemical properties of Sodium bis [salicylato (2-)]-borate-γ-butyrolactone Electrolytes in Sodium Battery. *Materials Today: Proceedings*. 2019. **6**: 86–94.
30. Kirchner B. Ionic Liquids Volume Editor. *Heidelberg: Springer*. 2009: 354.
31. House L., Hill J. Ionic Liquids Physicochemical Properties. *Amsterdam: Elsevier*. 2009. 478.
32. Gilliam R.J., Graydon J.W., Kirk D.W., Thorpe S.J. A review of specific conductivities of potassium hydroxide solutions for various concentrations and temperatures. *Int. J. Hydrogen Energy*. 2007. **32**(3): 359–364.
33. Xu K. Nonaqueous Liquid Electrolytes for Lithium-Based Rechargeable Batteries. *Chemical Reviews*. 2004. **104**(10): 4303–4417.
34. Nikolsky B.P. Handbook of the chemist. *Leningrad: Chemistry*. 1971. 1169 p. [*in Russian*].
35. Dudley J., Wilkinson D., Thomas G., LeVae R. Conductivity of electrolites for rehargeble lithium batteris. Journal of Poweer Sources. 1991. **35**(1): 59–82.
36. Yang H., Zhuang G., Ross P. Thermal Stability of LiPF6 Salt and Li-ion Battery Electrolytes Containing $LiPF_6$. Journal of Power Sources. 2006. **161**(1): 573–79.
37. Webber A. Conductivity and Viscosity of Solutions of LiCF3SO3, $Li(CF_3SO_2)_2N$, and Their Mixtures. Journal of The Electrochemical Society. 1991. **138**(9): 2586–2590.
38. Schaltkwijk W. Advances in Lithium-ion Batheries. *New York: Kluwer Academic*. 2002. 507 .
39. Dominey L., Koch V., Blakley T. Thermally stable lithium salts for polymer electrolytes. *Electrochimical Acta*. 1992. **37**(9): 1551–1554.
40. Diamant V. A., Trachevskii V. V., Pershina K. D., Ogenko V. M., Donchu Chen, Huawen Hu, Min Chen, Xiaowen Wang, Menglei Chang. Specialties of the structure and conductivity of the non-aqueous electrolytes based on alkali metal bis(salicyl) borates and bis (oxalato) borates. *Ukr. Chem. Journal*. 2019. **85**(3): 47–57.
41. Diamant V. A., Pershina K. D., Trachevskii V. V., Kazdobin K. A. Synthesis of Alkali Metal Bis(salicilato)borates by Microwave Method. *Surface Engineering & Applied Electrochemistry*. 2016. **52**(2): 212–216.

42. Borup R., Meyers J., Pivovar B., Kim Y. S., Mukundan R., Garland N., Zelenay P. Scientific aspects of polymer electrolyte fuel cell durability and degradation. *Chemical reviews*. 2007. **107**(10): 3904–3951.
43. Ivanov-Shits A. K., Demyanets L. N. Materials of the Ionic of a Solid. *Priroda*. 2003. **12**: 35–43.
44. Gromadsky D.G. High-capacity super-capacitors based on porous carbon materials with optimized electrode constituents. *PhD thesis: Kyiv*. 2012. 166 p. [*in Ukrainian*].
45. Sun X., Angell C. A. Doped sulfone electrolytes for high voltage Li-ion cell applications. *Electrochemistry Communications*. 2009. **11**(7): 1418–1421.
46. Świętosławski M., Molenda M., Grabowska M., Wach A., Kuśtrowski P., & Dziembaj R. Electrochemical impedance spectroscopy study of C/Li_2MnSiO_4 composite cathode material at different states of charge. *Solid State Ionics*. 2014. **263**: 99–102.
47. Péter, L. A systematic approach to the impedance of surface layers with mixed conductivity forming on electrodes. *Journal of Solid State Electrochemistry*. 2013. **17**(12): 3075–3081.
48. Zhang L., Huang J., Youssef K., Redfern P. C., Curtiss L. A., Amine K., Zhang Z. Molecular engineering toward stabilized interface: an electrolyte additive for high-performance Li-ion battery. *Journal of The Electrochemical Society*. 2014. **161**(14): A2262–A2267.
49. Kazdobin K. A., Pershina K. D., Kokhanenko V. V., Maslyuk L. N., Zapol'skii A. K. Nature of the conductivity of kaolin under hydration and mechanochemical activation. *Surface Engineering and Applied Electrochemistry*. 2014. **50**(1): 95–100.
50. Cecchetto L., Salomon M., Scrosati B., Croce F. Study of a Li–air battery having an electrolyte solution formed by a mixture of an ether-based aprotic solvent and an ionic liquid. *Journal of Power Sources*. 2012. **213**: 233–238.
51. Ran L., Liu X., Tang Q., Zhu K., Tian J., Du J., Shan Z. Grinding aid-assisted preparation of high-performance carbon-$LiMnPO_4$. *Electrochimica Acta*. 2013. **114**: 14–20.
52. Pershina, E.D., Kokhanenko, V.V., Maslyuk, L.N. *et al.* Conductivity of aqueous suspensions of alumosilicates. *Surf. Engin. Appl.Electroche.* 2011. **47**:441–445.
53. Wu Q., Ha S., Prakash J., Dees D. W., Lu W. Investigations on high energy lithium-ion batteries with aqueous binder. *Electrochimica Acta*. 2013. **114**: 1–6.
54. Seh Z. W., Sun J., Sun Y., Cui Y. A highly reversible room-temperature sodium metal anode. *ACS central science*. 2015. **1**(8): 449–455.
55. Manivel A., Velayutham D., Noel M. Electrochemical behaviour of tetra-n-butylammonium nonaflate as an ionic liquid and as a supporting electrolyte in aprotic solvents: A comparative study. *Journal of electroanalytical chemistry*. 2011. **655**(1): 79–86.
56. Bisquert J., Randriamahazaka H., Garcia-Belmonte G. Inductive behaviour by charge-transfer and relaxation in solid-state electrochemistry. *Electrochimica Acta*. 2005. **51**(4): 627–640.
57. Hiller M. M., Joost M., Gores H. J., Passerini S., Wiemhöfer H. D. The influence of interface polarization on the determination of lithium transference numbers of salt

in polyethylene oxide electrolytes. *Electrochimica Acta*. 2013. **114**: 21–29.
58. S.B. Aziz, T.J. Woo, M.F.Z. Kadir, H.M. Ahmed A conceptual review on polymer electrolytes and ion transport models. *Journal of Science: Advanced Materials and Devices.* 2018. 3(1):1–17.
59. K. D. Pershina, K. O. Kazdobin. Impedance spectroscopy of electrolytic materials. *Kyiv: Osvita Ukraine*. 2012. 223 p. [*In Ukrainian*].
60. Shih, Hong, and Tai-Chin Lo. Electrochemical impedance spectroscopy for battery research and development. *Cortech Corporation. CA, Tech. Rep*. 1996. **31**. 9–11.
61. Bisquert J., Compte A. Theory of the electrochemical impedance of anomalous diffusion. *Journal of Electroanalytical Chemistry*. 2001. **499**(1): 112–120.
62. Schweiger H.-G. Entwicklung und Erprobung neuer Messgeräte und Methoden für die rationelle Optimierung von neuen Elektrolyten für Lithium-Ionen-Batterien. *PhD thesis: Regensburg*. 2006.
63. Etacheri V., Marom R., Elazari R., Salitra G., Aurbach D. Challenges in the development of advanced Li-ion batteries: a review. *Energy & Environmental Science*. 2011. **4**(9): 3243–3262.
64. Kaymaksiz S., Wilhelm F., Wachtler M., Wohlfahrt-Mehrens M., Hartnig C., Tschernych I., Wietelmann U. Electrochemical stability of lithium salicylato-borates as electrolyte additives in Li-ion batteries. *Journal of Power Sources*. 2013. **239**: 659–669.
65. Bhattacharyya, A. J., & Maier, J. Second Phase Effects on the Conductivity of Non-Aqueous Salt Solutions:"Soggy Sand Electrolytes". *Advanced Materials*. 2004. **16**(9–10): 811–814.
66. Monti D., Jónsson E., Palacín M. R., Johansson P. Ionic liquid based electrolytes for sodium-ion batteries: Na^+ solvation and ionic conductivity. *Journal of Power Sources*. 2014. **245**: 630–636.
67. Ponrouch A., Monti D., Boschin A., Steen B., Johansson P., Palacin M. R. Non-aqueous electrolytes for sodium-ion batteries. *Journal of Materials Chemistry A*. 2015. **3**(1): 22.

Стаття надійшла 15.07.2021.

УДК 54-386; 546.662; 546.664 doi: 10.33609/2708-129X.87.06.2021.97-120

THE COORDINATION COMPOUNDS Gd (III) AND Dy(III) WITH SOME β-DIKETONES

O. S. Berezhnytska[1,2], A. E. Horbenko[1], O. O. Rohovtsov[1], S. S. Smola[3], Ya. V. Fedorov[1], O. E. Chygyrynets[2], O. K. Trunova[1]

[1] V.I.Vernadsky Institute of General and Inorganic Chemistry of NAS of Ukraine, Akad. Palladin Avenue, 32/34, Kyiv 03142, Ukraine.
[2] National Technical University of Ukraine «Igor Sikorsky Kyiv Polytechnic Institute», 37, Peremohy Avenue, Kyiv 03056, Ukraine.
[3] A.V. Bogatsky Physico-Chemical Institute NASU, Lyustdorfska doroha St., 86, Odessa, Ukraine
** e-mail: berezhnytska@gmail.com*

New complexes of Dy (III) and Gd (III) with b-diketones containing unsaturated and aryl substituents were synthesized. Metal polymers based on synthesized complexes were obtained by the method of radical polymerization. The composition and structure of synthesized complexes and metal polymers are established. It is shown that during polymerization the coordination environment of the central ion remains unchanged. The spectral-luminescent characteristics of the synthesized compounds were studied. The presence of water molecules in the immediate coordination environment causes a low intensity of emission of monomeric dysprosium complexes. In the luminescence spectra of metal polymers, there are bands magnetic dipole transition ($^4F_9 \rightarrow {}^6H_{15/2}$) and electric dipole transition ($^4F_9 \rightarrow {}^6H_{13/2}$). The close energies of the triplet level of the ligand and the resonant level of the dysprosium ion cause low emission characteristics of the synthesized dysprosium complexes.

Key words: lanthanides, complexes, luminescence properties, metalopolymer, gadolinium, dysprosium, β-diketones.

INTRODUCTION. High luminescence [1–6], magnetic activity [7–11], and the possibility of using as bioactive materials [12–13] and telecommunication devices [14–16] are responsible for the continuing interest in coordination compounds of lanthanides.Highly volatile stable complexes of lanthanides with a mononuclear structure play a significant role as precursors for the gas-phase synthesis of thin-film materials [17–18].

One of the most important factors influencing the properties is the correct selection of ligand systems makes it possible to avoid nonradiative energy losses during the transition from the singlet to the triplet level. Only at minimum phosphorescence and fluorescence energies can maximum luminescence intensities be achieved [19–22]. Therefore, the difference in the triplet energy level of the ligand and the resonance energy level of the lanthanide ion

is of great importance. In general, the energy of the resonance level of the metal should be somewhat lower than the energy of the triplet level of the ligand, which neutralizes the non-radiative deactivation of the resonance level together with a high probability and efficiency of the emitting transition. The overwhelming majority of studies in this area are on lanthanide complexes emitting in the visible region of the spectrum, in particular, Eu(III), Tb(III), Sm(III), Nd(III), Yb(III) [12, 20, 22–26]. Although dysprosium compounds (III) are also capable of emitting in the visible region of the spectrum, such studies are limited due to the complexity of the ligand selection. Such is due to the rather high energy of the resonance level of the dysprosium ion compared to Eu (III) and Sm (III). Some works considered the possibility of using dysprosium complexes in the creation of white light emitters for optoelectronics. It could be realized by doping or titrating dysprosium complexes with complexes of other metals, or by mixed-ligand complexation. Thus, in the work use, bimetallic Dy: Eu complexes and trimetallic Dy: Gd: Eu complexes emit white light. Doping of gadolinium complexes with dysprosium complexes or Dy \ Eu Dy \ Sm HMC allowed the authors to obtain white light [15, 27–28]. In particular, the work showed the possibility of transition from yellow through white to blue light [29, 30].

In addition, complexes of these metals can be used as contrast agents for MRI diagnostics. The Gd^{3+} and Dy^{3+} ions, having an optimal contrast enhancement in comparison with other paramagnetic ions, are highly toxic in the free state (10 mg / kg of body weight) [31]. Today, the chemical compounds DTPA (diethylenetriaminepentaacetic acid), DTPA-BMA (gadodiamide), DOTA (tetraazocyclododecanetetraacetic acid), HP-DO3A (2-hydroxypropyltetraazododecanetriacetic acid) and, other derivatives are used as ligand systems. Their complexes with metals have paramagnetic properties, are low-molecular water-soluble, hydrophilic contrast agents that are excreted from the body by the kidneys [31–33]. The main problem of creating paramagnetic contrast agents is to find the optimal balance of high paramagnetic properties and toxicity. The ideal contrast paramagnetic should have the maximum relaxing ability in the practical absence of toxicity [34, 35]. For the rejection of macromolecular contrast agents, it is possible to create a significant improvement in the relaxation efficiency of low-molecular-weight compounds [36, 37]. In addition, polymeric systems based on non-scaling b-diketonates of lanthanides (Gd (III) and Dy (III) can be used as a precursor for rejecting contrast talkers to compete with other active materials. cell link in the molecule ligand.

It is unlikely that in the low-molecular state, β-diketones could be used as precursors for obtaining contrast agents because they are bidentate ligands. However, polymer systems based on them can compete with existing materials. The presence of a final double bond in the ligand molecule makes it an active monomer in polymerization reactions. Thus, metal complexes based on unsaturated β-diketones are active monomers in free radical polymerization reactions [38, 39].

According to the literature data, it could be pointed the areas of high scientific and technological interests of this investigations: 1 – the using both mono- and heterometallic complexes Gd (III) and Dy (III); 2 – doping of gadolinium complexes by complexes of other metals emitted in the visible and nearest-IR spectral regions.

In this regard, in this work, we performed the synthesis, studies of the structure and properties of-diketonate complexes of Gd (III) and Dy (III) with unsaturated β-diketones and metal polymers based on them.

EXPERIMENT AND DISCUSSION OF THE RESULTS. As starting compounds were selected β-diketonate ligands (2-methyl-5-phenylpentan 1-3,5, -dion (mphrd) (2-methyl-5-biphenyl penten 1-3,5, -dione (mbphd) are shown in scheme 1.

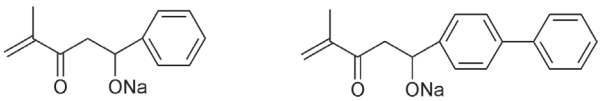

mphpd mbphpd

Scheme 1. Structure of the ligands.

To a three-necked reactor cooled with a mixture of ice and sodium chloride, equipped with a magnetic stirrer, a reflux condenser and a dropping funnel containing 0,5 moles of sodium metal (11,5 g) and, 300 cm^3 of dry diethyl ether, was added dropwise a solution of 0,5 mol (99 cm^3) of biphenylketone and 0,5 mol (63 cm^3) of methacrylic acid ethyl ester. As a result of the reaction, a yellow precipitate fell out:

The synthesis of ligands was performed by Kleisen condensation according to the scheme presented in Fig. The method of ligand synthesis is described earlier [38, 40].

For the synthesis of β-diketonate complexes Gd (III) and Dy (III) was used dysprosium acetate (III) $Dy(CH_3COO)_3 \cdot 4H_2O$ (c.p), gadolinium nitrate (III) $Gd(NO_3)_3 \cdot 5H_2O$ (c.p), sodium hydroxide NaOH (c.p).

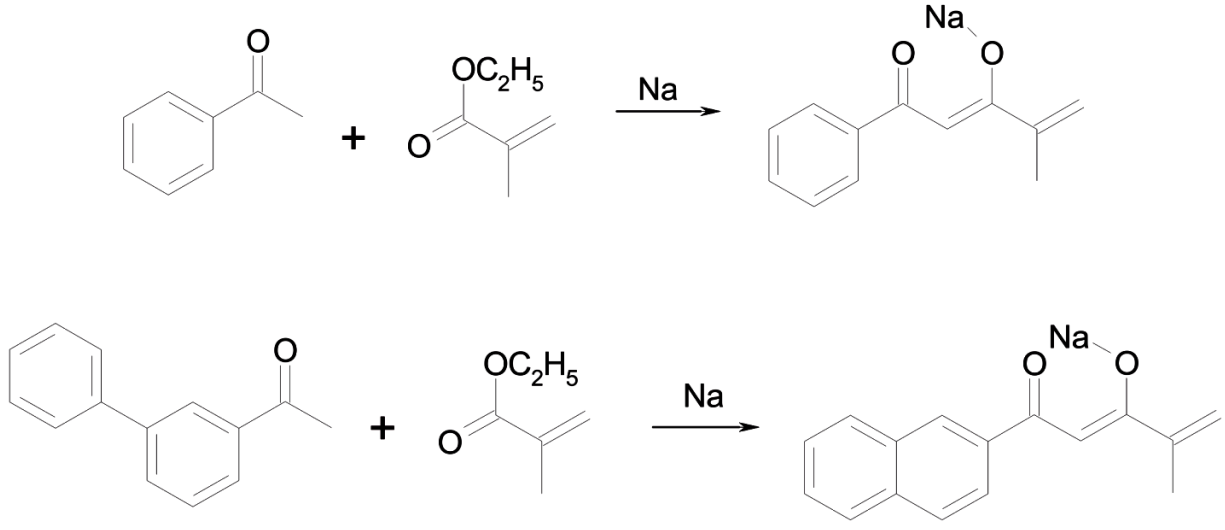

Scheme 2. Synthesis scheme of ligands.

The synthesis of complexes was performed by the interaction of aqueous solutions of metal salts with an aqueous solution of a sodium salt of the corresponding ligand at a molar ratio of reagents 1: 3 (pH 8–9) at room temperature.

$$Dy(CH_3COO)_3 + 3NaL \rightarrow DeL_3 + 3CH_3COONa$$

$$Gd(NO_3)_3 + 3NaL \rightarrow GdL_3 + 3NaNO_3$$

L= mphpd, mbphpd.

The resulting precipitates of the complexes were separated from the mother liquor by centrifugation, washed with water, and dried in a vacuum desiccator over anhydrous $CaCl_2$. All synthesized complexes were yellowish.

A feature of the synthesis and purification of β-diketonates of lanthanides $Ln(\beta\text{-dik})_3$ is the need to carry out all operations at room temperature, since with an increase in temperature, partial oligomerization of the complexes occurs (due to the presence of a reactive C=C double bond in ligand molecules), significantly worsens their solubility. Therefore, recrystallization and additional purification of the complexes by vacuum sublimation were not carried out, although the volatility of the complexes is high enough, which was confirmed by the results of thermal analysis.

Metal polymers of gadolinium and dysprosium were obtained by the method of thermally initiated radical polymerization. Polymerization was carried out at 80° C in a DMF solution at a monomer (tris-diketone) concentration of 0.3 mol/dm^3 and an AIBN initiator concentration of 0.003 mol/dm^3. The obtained metal polymers were precipitated from solutions with isopropanol [26, 38].

The synthesized compounds were investigated by elemental analysis, FTIR, electron and fluorescence spectroscopy, thermal analysis, dynamic light scattering, and electron microscopy (SEM).

Quantum-chemical calculations of ligand molecules and metal complexes were carried out. The geometry of β-diketone molecules and their complexes with dysprosium and gadolinium was calculated using the MOPAC2016 program. For the calculation, the PM7 method was chosen, which better shows the long-range interaction of atoms in a molecule, makes it possible to more accurately predict the crystal structure and heats of the formation of solids. In addition, the PM7 method calculates hydrogen bonds in more detail, which makes it possible to better describe non-covalent interactions. The use of PM7 in combination with the SPARKLE model, in which the lanthanide atom is represented as a point charge [41–42], makes it possible to obtain reliable data on the geometry of lanthanide complexes with both aliphatic and aromatic ligands.

The estimation of the enthalpy of formation of complexes was carried out on the basis of the calculated values for ligands and the corresponding values for metal complexes. The energy gap between the upper filled molecular orbital (HOMO) and the lower vacant molecular orbital (LUMO) was calculated. For each ligand and complex, the total energy, dipole moment, and ionization potential were given. The populations on the atomic orbitals and the charges on the atoms of the ligand molecules and the corresponding complexes with gadolinium and dysprosium were calculated. This allows us to conclude about the localization of the electron density and bond saturation.

Quantum-chemical calculations of ligand molecules and metal complexes based on them were carried out. The geometric structure of the ligand molecule was first optimized by the molecular mechanics method MM+ using the HyperChem program, then the resulting geometric structure was the initial one for optimization of the molecule geometry based on the SPARKLE PM7 model in the MOPAC2016 program. As a result of calculations, the following geometrically optimized structures were obtained (Fig.1).

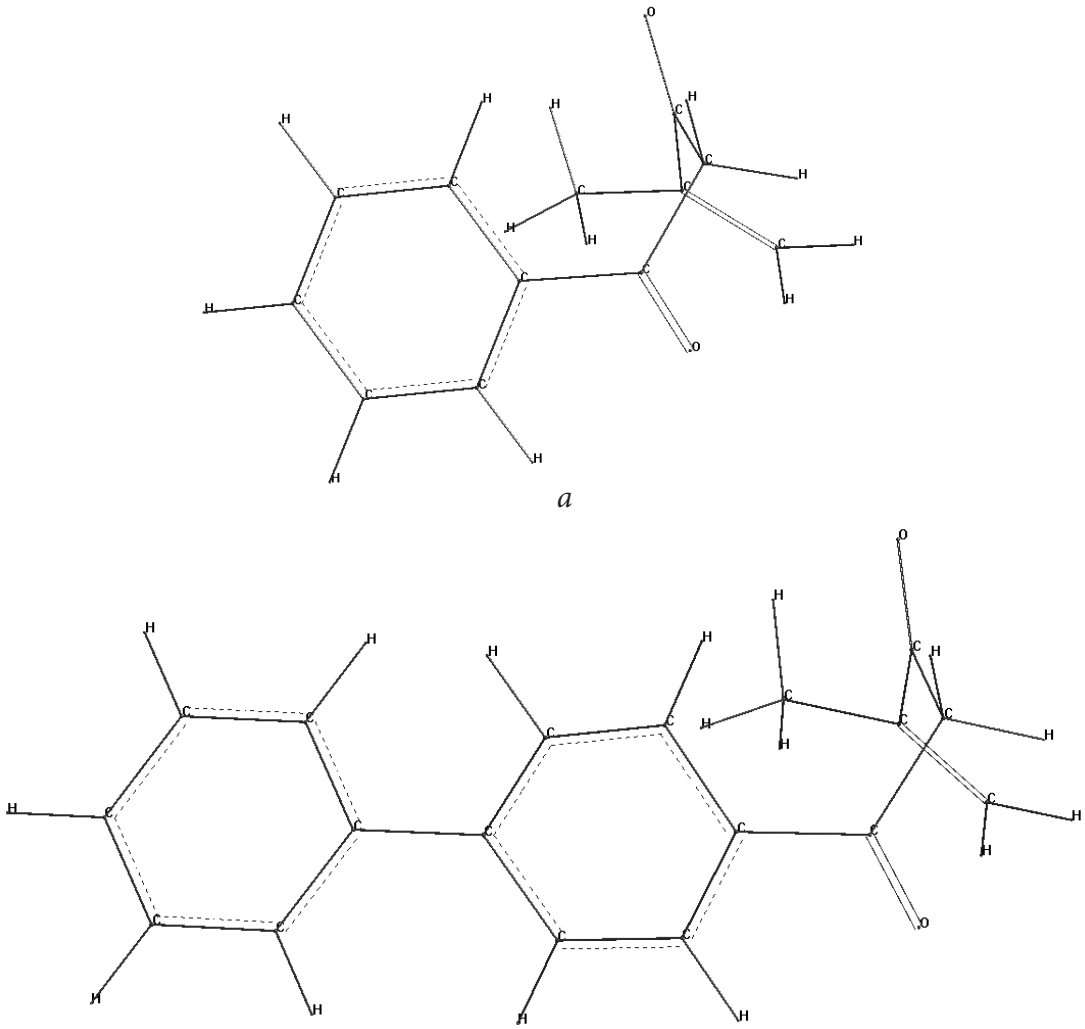

a

b

Fig. 1. Geometrically optimized structural formulas of β-diketones (a – mphpd, b – mbphpd).

There were calculated the base energy characteristics of the ligand molecules using the SPARKLE PM7 model: the enthalpy of formation, the total energy of the molecule and bond lengths, the parameters of the electron populations of the ligands (Table 1).

Table 1

Characteristics of the structure and electronic populations of β-diketone molecules and β-diketone molecules.

Estimated parameter	mphpd	mbphpd
Total energy (eB)	-2225,898	-3001,148
Heat of formation (kJ / mol)	-187,341	-119,148
The dipole moment	2,179	2,526

Table 1

E_{homo}(eV)	-10,227	-9,561
E_{lumo}(eV)	-0,697	-1,061
Energy gap	9,53	8,5
Ionization potential (eV)	10,227	9,473
Bond lenght (Å)		
C_{RCO} - R	1,48175	1,4824
C_{RCO} - O	1,20643	1,20565
$C_{RCO} – C_{CH2}$	1,50965	1,50799
$C_{CH2} – C_{CO}$	1,51066	1,5115
C_{CO} - O	1,20514	1,2051
$C_{CO} – C_{C-CH2}$	1,48905	1,4891
Atomic unit of charge:		
Q C_{RCO}/Q_{CR}	0,4832/-0,1651	0,4953/ -0,1693
QC_{RCO} / QO	0,4832/-0,4296	0,4953/-0,4460
QC_{CH2} / QC_{CO}	-0,4988/ 0,4734	-0,501/0,4814
Q C_{CO} /QO	0,4734/-0,4309	0,4814/-0,4311
$QC_{CO} – QC_{C-CH2}$	0,4734/ -0,0605	0,4814/ -0,0406

Analyzing the value of the heats of formation of ligands, we see that the process of formation of molecules is exothermic, we observed this in the process of synthesis. As mentioned above, while mixing the starting reagents, the reaction mixture was heated. With an increase in the volume of the ligand, upon going from phenolic to biphenyl substituent, the heat of formation increases from -187.341 kJ/mol (mphpd) to -119.148 kJ/mol (mbphpd). The dipole moment for mbphpd (2.526) is slightly higher than for mphpd (2.179), which may be due to the different distribution of electron charges in the biphenyl molecule. The bond lengths in both molecules are comparable, as expected, due to the same nature of the substituents. The negative charge in both ligands is concentrated on oxygen atoms. Having calculated the energies of the highest filled molecular orbital (E_{HOMO}) and the lowest vacant molecular orbital (E_{LUMO}), we can conclude that these complexes will exhibit weak electron-withdrawing properties, for mphpd and mbphpd E_{LUMO} = -0.697 eV and -1.061 eV, respectively.

The performed quantum-chemical calculations made it possible to geometrically optimize the molecules of β-diketonate complexes of gadolinium and dysprosium (Fig.2)

As can be seen from Fig. and fig. all presented complex compounds have a non-planar structure, and the ligands are located in different planes. All ligands are bidentate and are coordinated to the central ion (c.i) by two oxygen atoms, which is consistent with previous studies and literature data. Comparing the average bond lengths of lanthanides - oxygen, we see that in dysprosium complexes it is less - 2.2241 Å versus 2.2381 Å for gadolinium complexes (Table 1). Such a change in the bond length can be explained both by the effect of lanthanide compression and by different populations of orbitals.

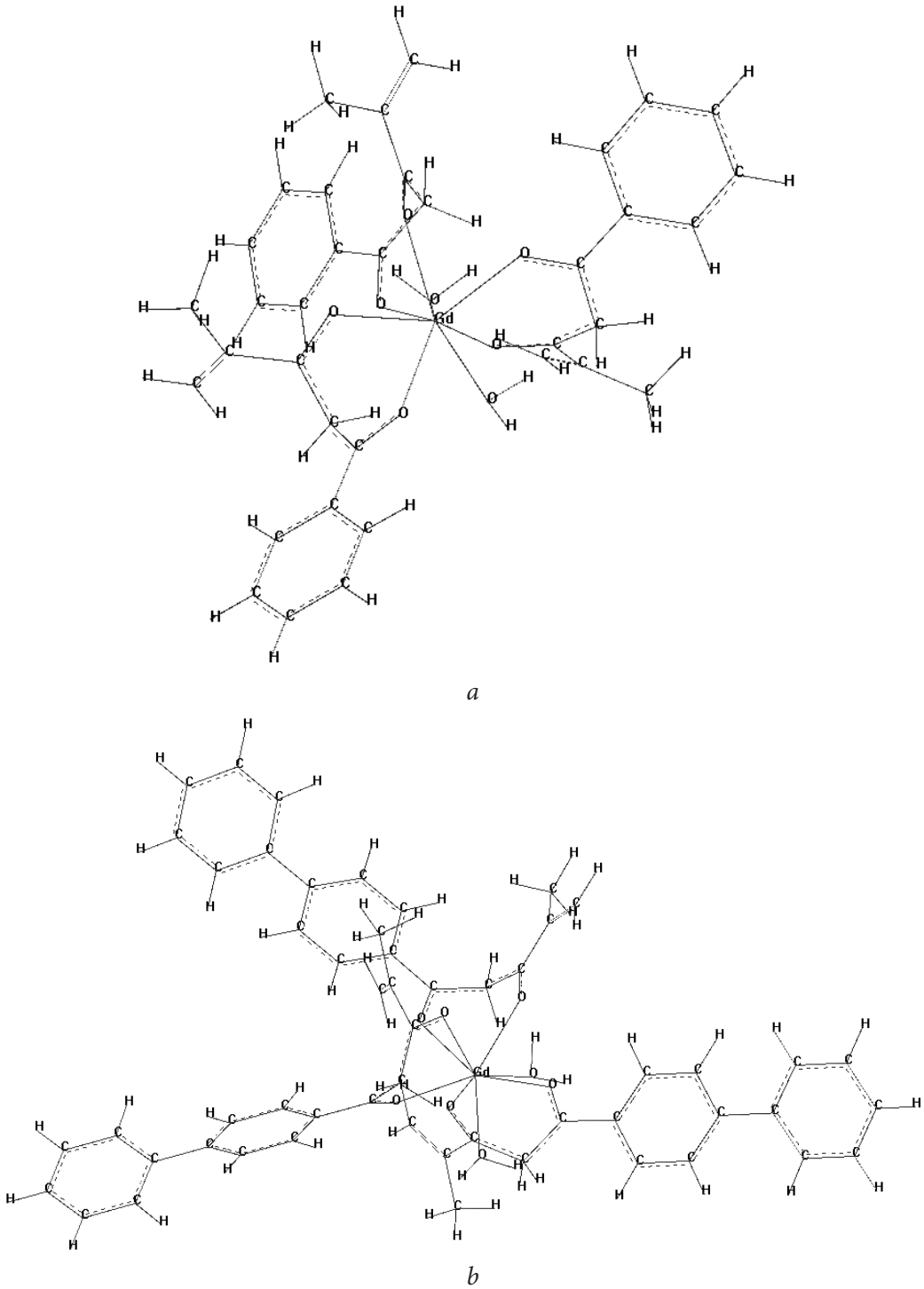

a

b

Fig. 2. Geometrically structure of β-diketonate complexes of $Gd(mphpd)_3 \cdot 2H_2O$ (a) and $Gd(mbphpd)_3 \cdot 2H_2O$ (b).

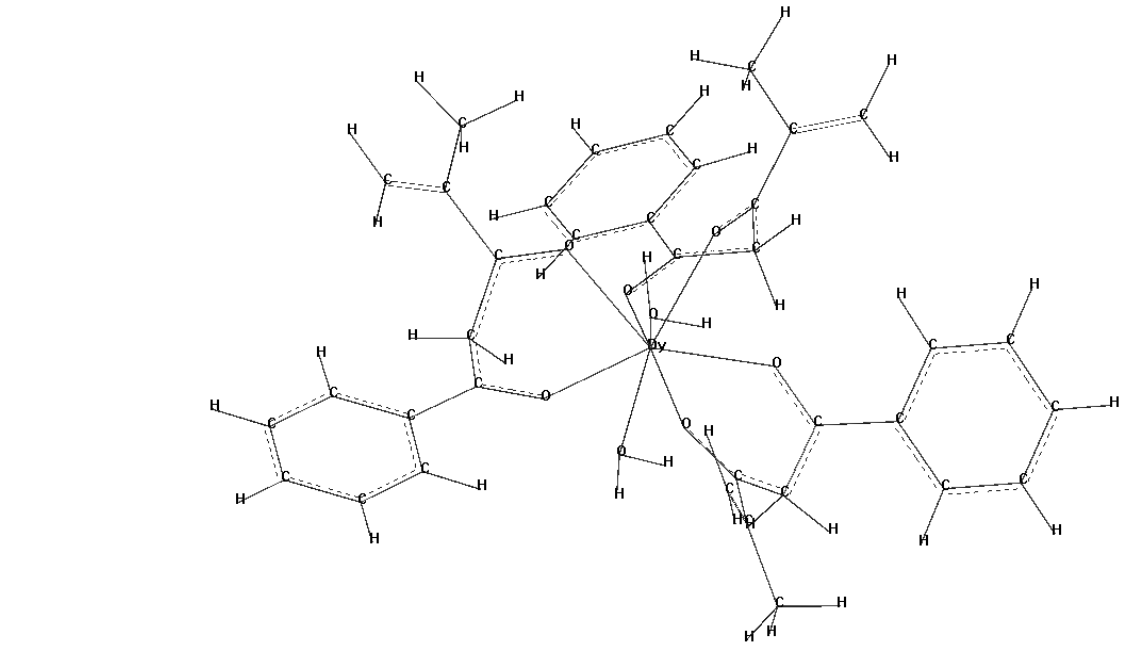

a

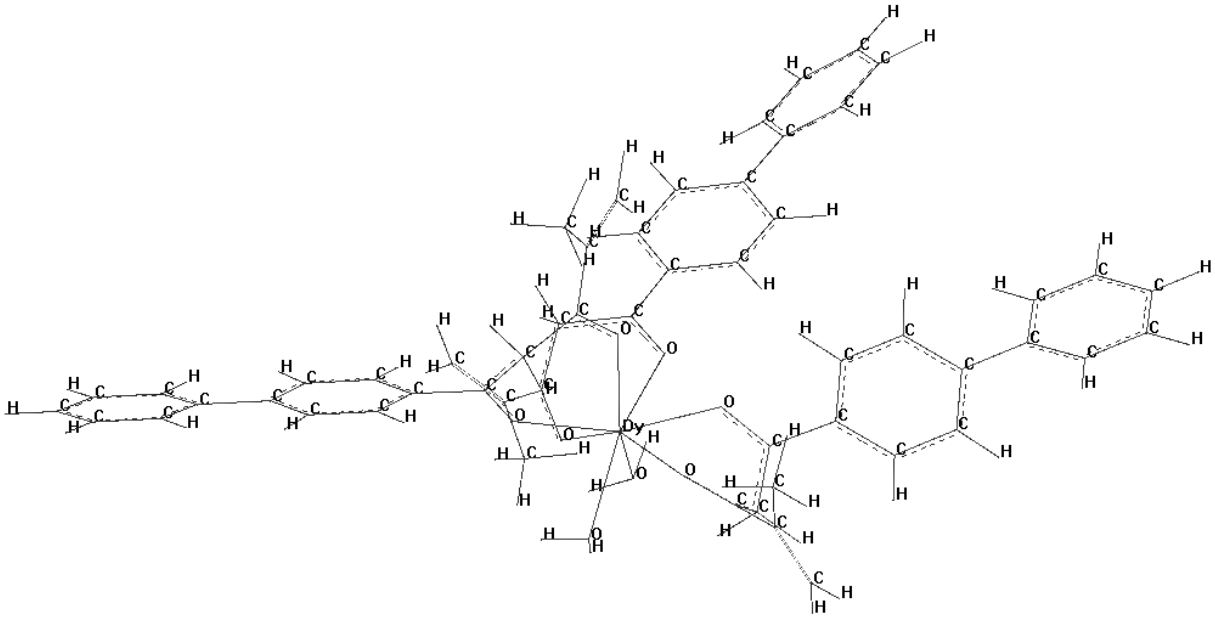

b

Fig. 3. Geometrically structure of β-diketonate complexes of $Dy(mphpd)_3 \cdot 2H_2O$ (a) and $Dy(mbphpd)_3 \cdot 2H_2O$ (b).

Analyzing the value of the heats of formation of complexes, it can be noted that negative values are observed for complexes based on mphpd, and positive for complexes of Gd and Dy with mbphpd - +106.474 and +185.622 kJ/mol, respectively. For the complexes $Gd(mbphpd)_3 \cdot 2H_2O$ and $Dy(mbphpd)_3 \cdot 2H_2O$, we have a positive value of the heats of formation, indicating that the formation of complexes occurs with heat absorption, that is, the process is endothermic.

As can be seen from the energies of the highest filled molecular orbital (EHOMO) and the lowest vacant molecular orbital (ELUMO), the complexes exhibit electron-withdrawing properties. EHOMO behaves like an electron donor, while ELUMO behaves like an acceptor. The difference between the energies of EHOMO and ELUMO represents the HOMO-LUMO energy gap. If a molecule has a small energy gap, it shows high reactivity.

The ionization potential and the parameters of the electron affinity were determined using the energies of E_{HOMO} and ELUMO, namely, $I = -E_{HOMO}$ and $A = -E_{LUMO}$, where I is the ionization energy and A is the electron affinity. In ionization by potential, a physical quantity is understood, which is determined by the ratio of the smallest energy required for the single ionization of an atom (or molecule) in the ground state to the charge of an electron. Ionization potential is a measure of ionization energy equal to the work of detachment of an electron from an atom or molecule and characterizes the bond strength of an electron in an atom or molecule.

As can be seen from the table, all calculated parameters correlate quite well in the case of pairs of complexes with the same ligands, namely: $Gd(mphpd)_3$ and $Dy(mphpd)_3$, $Gd(mbphpd)_3$ and $Dy(mbphpd)_3$. Somewhat lower values of the series parameters for dysprosium complexes, including the length of the lanthanide-oxygen bond, which is determined both by the different electronic structure of c.i. and by a decrease in the ionic radius of the latter. All calculated parameters of the complexes are shown in table 2.

Table 2

Characteristics of the structure and electronic populations of complexes.

Estimated parameter	$Gd(mphpd)_3$	$Gd(mbphpd)_3$	$Dy(mphpd)_3$	$Dy(mbphpd)_3$
Total energy (eV)	-6675,884	-8230,603	-6675,479	-8872,074
Heat of formation (kJ / mol)	- 105,962	106,474	-26,744	185,622
The dipole moment	0,696	0,576	0,723	0,572
E_{homo}(eV)	-9,249	-8,932	-9,244	-8,929
E_{lumo}(eV)	-0,548	-0,868	-0,558	-0,872
Energy gap	8,701	8,064	8,686	8,057
Ionization potential (eV)	9,249	8,931	9,244	8,929
Electron affinity (eV)	0,548	0,868	0,558	0,872
Hardness (eV)	4,3505	4,032	4,343	4,0285
Softness (eV)	0,23	0,248	0,2302	0,248
Bond length l_{av} O-Ln (Å)	2,2355	2,2454	2,2266	2,2242

The elimination of adsorbed water occurs at 70^{0}C, further dehydration of dysprosium and gadolinium complexes with methacroylacetophenone Ln(mphpd)$_3$ occurs at temperatures of 1650C and 1900C, respectively, and is accompanied by significant endoeffects. At the same time, there is a loss of sample mass by 4.4% (mop = 4.7%) for Dy(mphpd)$_3$ and 4.6% for Gd(mphpd)$_3$ (mop = 4.8%), which corresponds to the elimination of two coordinated water molecules. Endoeffects at temperatures of 198^{0}C (Dy(mphpd)$_3$) and 189^{0}C (Gd(mphpd)$_3$) are due to the melting of the complexes (the weight loss in this case is 2% and 1.8%, respectively). A further increase in temperature is accompanied by small exoeffects (235^{0}C for Dy and 242^{0}C for Gd) and an insignificant weight loss, which corresponds to the polymerization of the complexes. With a further increase in temperature (> 240^{0}C) in both compounds, the destruction of the complex occurs by the elimination of one molecule of methacroylacetophenone, which is accompanied by exothermic effects at 275 and 278^{0}C, respectively [43].

In the temperature range 285–500^{0}C, the thermal destruction of both complexes proceeds with the generation of heat; the thermogram contains exoeffects at 293, 332, 380, 442^{0}C for Dy(mphpd)$_3$; 305, 345, 380^{0}C for Gd(mphpd)$_3$) and a significant loss in the mass of the samples, which is due to the decomposition of organic fragments of the molecule. The total weight loss in the investigated temperature range for both complexes is ~ 80%. The general view of the thermograms of complexes based on mbphpd is practically the same. The only difference are in the lower dehydration temperature of complexes 150^{0}C (Dy(mbphpd)$_3$ and 165^{0}C - Gd(mbphpd)$_3$. The results of elemental analysis and DTA made it possible to establish that the composition of the synthesized complexes corresponds to the formula $LnL_3 \cdot 2H_2O$ Ln = Gd, Dy, L = mphpd, mbphpd.

Thermograms of methalopolymers differ significantly. A significant endoeffect at 175–185^{0}C is due to the elimination of water molecules, which are located in the cavities of the metalopolymer. Upon further heating, we observe an exoeffect at 350^{0}C and a significant weight loss ($\Delta m \approx 30\%$), which may be due to the destruction of the metalopolymer structure. Endoeffect at 440^{0}C may be due to steric rearrangements in the polymer structure. Further heating of the sample is accompanied by small exoeffects at 480 and 490^{0}C with practically no change in its weight, which indicates the stability of the polymer at high temperatures and the absence of destruction of the polymer structure.

The investigating of the results of thermal analysis, we can say that the dehydration of all synthesized monomeric complexes with aryl substituents occurs in the range 120–130^{0}C, which indicates the outer-sphere coordination of water molecules. Minor endoeffects in the region of 195–207^{0}C are due to the melting of the complexes (the weight loss is insignificant, up to 2.5%). An increase in temperature is accompanied by a number of exoeffects in the range 240–290^{0}C, which corresponds to the elimination of one ligand molecule, the weight loss, in this case, is in the range of 24–28%, which is in good agreement with the theoretically calculated). Further exoeffects after 300^{0}C correspond to the destruction of the organic part of the molecule, and a significant loss of mass. In general, the weight loss in the investigated temperature range is 75–85%. The decomposition mechanism for similar coordination compounds was described in detail

by the authors earlier [43-45]. Weight loss in this temperature range is accompanied by an insignificant endoeffect and corresponds to two coordinated water molecules, together with elemental analysis allows us to state that the composition of monomeric complexes corresponds to the formula $LnL_3 \cdot 2H_2O$, where Ln = Gd(III), Dy(III) L = mphpd, mbphhd.

IR spectra were recorded on a Specord M80 spectrometer in the range of 400-4000 cm^{-1} in KBr pellet. There are bands of symmetric and asymmetric stretching vibrations of the bond ν (C-O) and ν (C-C) in the IR spectra of the synthesized metal β-diketonates in the range of 1500–1700 cm^{-1}. Since there is delocalization of the electron density in the diketonate fragment, the stretching vibration bands also occupy an intermediate place between the stretching vibrations of single CO and CC and double C=O and C=C bonds [45–47]. It is known that a band with a higher frequency (~ 1575–1590 cm^{-1}) corresponds to a symmetric stretching vibration of the bond (CO), and with a lower frequency (~ 1520–1555 cm^{-1}) – to an asymmetric stretching vibration of a bond (CC). However, quite often these bands are observed as one wide line split into several components.

Table 3

Characteristic frequencies in IR spectra of Dy and Gd complexes with β-diketones (cm^{-1}).

Complex	ν(M-O) $+\delta_{hel.ring}$	ν_{as}(CO)	ν_{as}(CC)	ν_s(CO)	ν_s(CC)+ ν_s(CPh)	ν(H_2O)
$Dy(mphpd)_3$	415,422, 438, 475, 520	1427	1555	1590	1640, 1660	3230 3414
$[Dy(mphpd)_3]_n$	410, 425, 485, 515	1430	1560	1590	1640	3380
$Gd(mphpd)_3$	415,420,433, 473, 518	1440	1540, 1557	1595	1645, 1652	3350
$[Gd(mphpd)_3]_n$	412, 425, 490, 515	1445	1550	1590	1658	3380
$Dy(mbphhd)_3$	456, 470, 489, 520	1403, 1415	1542, 1560	1610	1680	3425
$[Dy(mbphhd)_3]_n$	450, 468, 470, 480, 515	1410	1550	1610	1670	3420
$Gd(mbphhd)_3$	455, 462, 478, 490, 514	1405	1540, 1560	1612	1675	3430
$[Gd(mbphhd)_3]_n$	455, 470, 485,500, 520	1400	1550	1605	1670	3430

Some inequality of ties, despite the delocalized system, is still present. This is especially noticeable in the region of 400–600 cm^{-1}, it is here that there are stretching vibrations of the M-O bond and deformation vibrations of a careless ring. Therefore, in this region of the spectrum, there is a significant number, mainly of low- intensity bands. This is due to the different

nature of the bonds, the electronic structure of the complexing ion, and the influence of the substituent in the diketonate fragment. For the same reason, in the 1400-1600 cm^{-1} region, we observe an insignificant splitting of the spectral lines assigned to ν_{as}(CC) and ν_{s}(CO). However, this inequality of bonds is not significant; therefore, it is inappropriate to speak of a significant deformation of the coordination polyhedron.

For all synthesized complexes in the region of 3200–3400 cm^{-1}, a broadband is observed, which corresponds to valence vibrations of coordinated water molecules. Unfortunately, based on the results of IR spectra, it is impossible to separate coordinated and adsorbed water molecules, however, based on the width of this band, we can confidently conclude that the synthesized compounds are not hydroxo complexes, this fact is also confirmed by their rather high solubility in organic solvents, in particular, DMSO, DMF, chloroform.

In general, the IR spectra of metal polymers table 3 are similar to the corresponding monomeric complexes, but there is an insignificant long-wavelength shift of the bands corresponding to characteristic vibrations, which suggests a weakening of the metal-ligand bond for polymers as compared to the monomeric complex. For polymers, the MO stretching vibration bands have already been split into several components, confirming a more ordered structure of metal polymers as compared to the monomeric complex.

Thus, the shape and position of the bands in the IR spectra of monomeric and metal-polymer complexes of gadolinium and dysprosium are characteristic of bidentate-coordinated β-diketonate ligands with delocalized π-bonds in the chelate rings (Table 3). The displacement of the position of the bands of metal polymers compared to monomers to the low-frequency region indicates a weakening of the metal-ligand bond, which is due to a higher part of covalence. Taking into account the data of IR spectroscopy and DTA, the schematic structure of complexes of lanthanides with β-diketones (for example, methacroylacetophenone) can be depicted as follows:

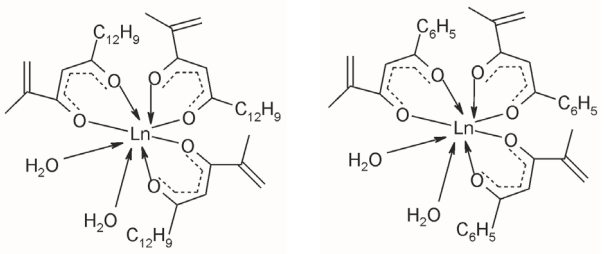

Ln = Gd^{3+}, Dy^{3+}

In the diffuse reflectance and electronic absorption spectra of the synthesized gadolinium and dysprosium compounds, there are broadened bands in the range of 230–400 cm^{-1}, which can be attributed to the $\pi \rightarrow \pi^*$ electronic transitions from the ground (S0) to the excited state (S1) of ligand molecules. The shift (70–100 nm) and broadening of this band, in comparison with its position for free ligands, may indicate both the realization of the complexation process and the influence of the electronic structure of the metal and substituents in the dicarbonyl fragment, as well as the superposition of the $\pi \rightarrow \pi^*$ bands the electronic transition and the charge transfer band from the ligand to the metal, the different nature of these transitions (Fig. 4). The lower intensity of the band of metallopolymers compared to monomers is due to the shielding of neighboring molecules by polymer fragments due to their larger size compared to monomeric systems. Since the main transitions of the gadolinium ion are observed in the UV region, it is impos-

sible to identify them for these compounds, since they overlap with the intense charge transfer band from the metal to the ligand. The shape of the band in both monomeric gadolinium complexes is the same, but in the case of the biphenyl substituent, we observe a shift of the band by 20 nm, which is due to different energies of the ligands and, accordingly, different positions of the charge transfer band. The broadening of the band for metal polymers is due to exchange interactions in the polymer; however, it should be noted that the position of the maxima in the monomer and polymer are unchanged, and an insignificant shift by 2–4 nm is due to additional exchange interactions in the polymer structure.

The similar shape and position of this band both in the diffuse reflectance spectra of the compounds and in the EAS indicates the similarity of the structure of the complexes in solution and in the polycrystalline state. In the diffusion reflection spectra of dysprosium coordination compounds, a set of bands with $^6H_{13/2}$ of the main multiplet is observed Table 4.

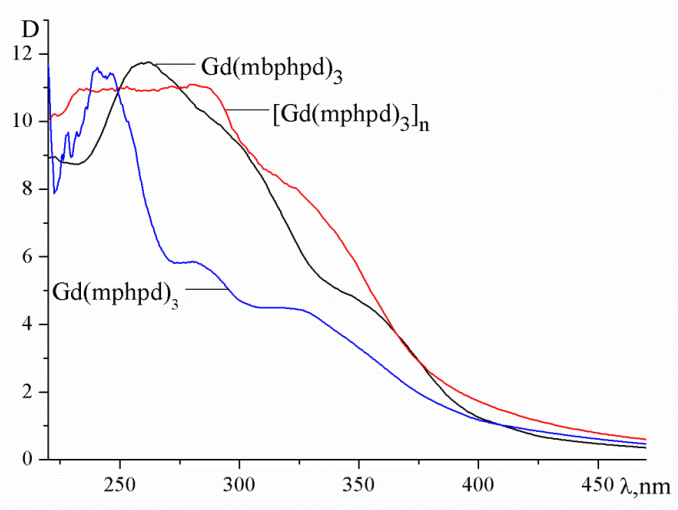

Fig. 4. Reflectance spectra of gadolinium complexes.

Table 4

The energy of the transition in the reflective spectra of the dysprosium (III) coordination compounds.

Transition	$Dy(mphpd)_3$	$[Dy(mphpd)_3]_n$	$Dy(mbphpd)_3$	$[Dy(mbphpd)_3]_n$
$^6H_{13/2}\rightarrow {}^6F_{3/2}$	756	757	757,763	758
$^6H_{13/2}\rightarrow {}^6F_{5/2}$	806	808	807	810
$^6H_{13/2}\rightarrow {}^6F_{7/2}$	906	909	907	910
$^6H_{13/2}\rightarrow {}^6F_{9/2,}\ {}^6H_{7/2}$	1097	1099	1100	1100
$^6H_{13/2}\rightarrow {}^6F_{11/2,}\ {}^6H_{9/2}$	1287	1289	1289	1290
$^6H_{13/2}\rightarrow {}^6F_{13/2,}\ H_{11/2}$	1697	1700	1699	1702

The shape and position of the bands in the diffuse reflectance spectra of monomeric and polymer complexes are similar (Fig.5) indicate a similar structure of the coordination polyhedron in monomeric and metal-polymer complexes. An insignificant shift of the bands to longer wavelengths, and in some places their broadening indicates a weakening of the bond of the central ion with the ligand in polymers, and on the presence of exchange interactions in the macromolecules of the metal chelating agents. Schematically, the structure of the elementary unit of metal polymers could be depicted as follows:

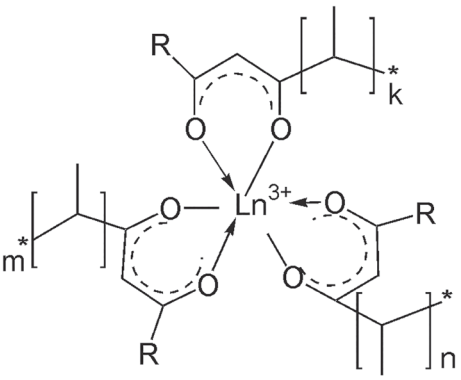

Ln=Gd, Dy; R=C_6H_5, $C_{12}H_9$

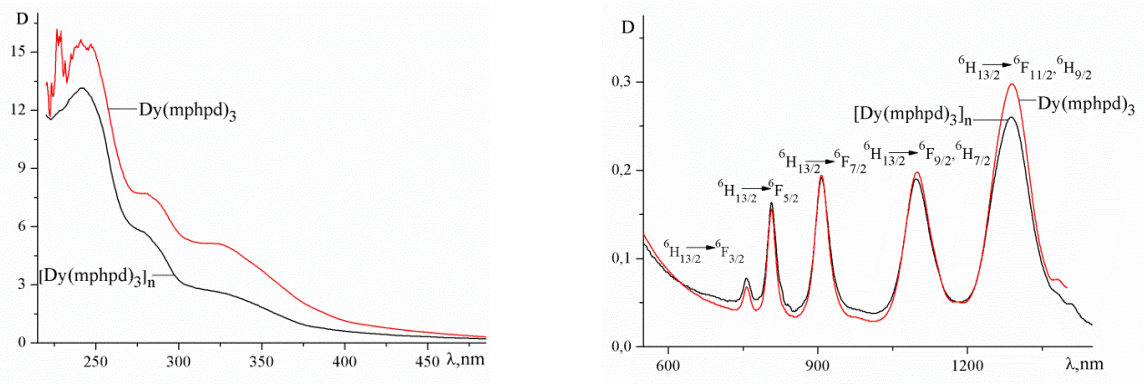

Fig. 5. Diffuse reflection spectra of dysprosium compounds.

Unfortunately, the method of electron spectroscopy does not allow one to establish the symmetry or structure of the coordination polyhedron for the studied coordination compounds. However, based on previous studies of similar complexes of europium, neodymium, samarium, and the ability to the splitting of spectral lines, such complexes have non-cubic symmetry of the ligand field.

Therefore, in order to determine the energy of the singlet and triplet levels of the ligands, the fluorescence and phosphorescence spectra of gadolinium-containing complexes were studied (Fig. 6).The excitation and luminescence spectra of solid complexes were recorded on a spectrofluorimeter Fluorolog FL 3-22, Horiba Jobin Yvon (Xe-lamp 450 W) with a light filter OS 11, with their subsequent

adjustment taking into account the radiation distribution of the xenon lamp and the sensitivity of the photomultiplier tube. The InGaAs (DSS-IGA020L, Electro-Optical Systems, Inc, USA) photoresistance was used as a radiation receiver for the IR region when cooled to liquid nitrogen temperature.

In general, ligand energies can be determined by recording the phosphorescence and fluorescence spectra of gadolinium, lanthanum, and lutetium complexes, which is due to the empty (lanthanum), half-filled (gadolinium), and completely filled (lutetium) f shell of these ions. For methacroylacetophenone, we recorded the fluorescence spectra of both the ligand itself and all the above complexes based on it. The results obtained are in good agreement with each other, and the obtained energy value is the same in all cases.

Subsequently, to establish the energy of the singlet and triplet levels of the ligand, we chose the Gd (III) complexes, which is due to several reasons, namely: the high position of the resonance level of Gd^{3+} (32000 cm^{-1}) in comparison with the triplet level of the ligands, prevents energy transfer from the organic part of the complex to the lanthanide ion and the presence of a heavy paramagnetic ion increase the efficiency of intersystem conversion due to mixing of singlet and triplet levels («paramagnetic effect») and, as a consequence, the ratio of the phosphorescence quantum yield to the fluorescence quantum yield (> 100).

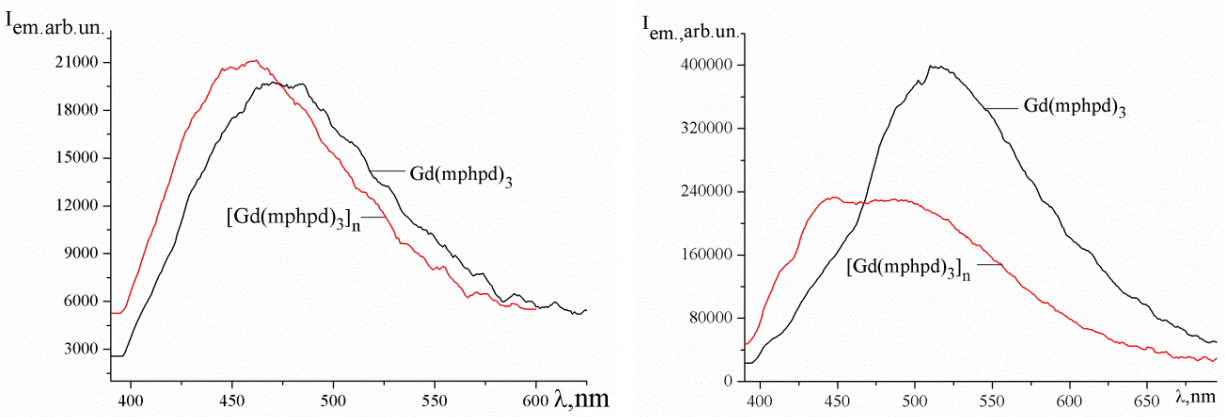

Fig. 6. Fluorescence (a) and phosphorescence spectra of the $Gd(mphpd)_3$ complex ($CHCl_3$ solution, λ = 380 nm).

The fluorescence spectrum of $Gd(mphpd)_3$ contains one structureless diffuse band with maxima at 450, 467, and 482 nm. The phosphorescence spectrum of the $Gd(mphpd)_3$ complex is a broad band with two maxima at 505 and 515 nm. It was found that for gadolinium methacroylacetophenonate, the energies of the singlet S_1 and triplet T_1 levels are 22150 cm^{-1} and 19520 cm^{-1}, respectively (table 5). Similar studies were carried out for all gadolinium complexes. It should be noted that the similarity between the excitation and fluorescence spectra for complexes with mphpd and mbphpd, which is associated with the same nature of the substituents in the diketonate fragment. The fluorescence spectrum of the polymer sample

$[Gd(mphpd)_3]_n$ (Fig.7). Contains one diffuse band with maxima at 431, 447, 461 nm. The position of the maxima in the $[Gd(mphpd)_3]_n$ phosphorescence spectrum (Fig.7) At 419 nm (shoulder), 449 nm, and 484 nm indicates that the energies of the singlet levels of the monomeric and metal-polymer complexes are close. Comparing the energy of the levels for the monomeric and polymer complexes of gadolinium (Table 5), it can be seen that polymerization causes an increase in the energy of exciting levels by ~ 1300 cm^{-1}, which is associated with the delocalization of the electron density in the ligand molecule.

For gadolinium complexes with mbphpd, we also recorded the fluorescence and phosphorescence spectra, as well as excitation and emission spectra (Fig. 6). The calculated energies of the singlet and triplet levels of all ligands are given in the table 5.

Table 5

Calculated energies of the singlet and triplet levels of the studied ligand systems.

Compounds	$E_{S1,}cm^{-1}$	$E_{T1,}$ cm^{-1}
$Gd(mphpd)_3$	22150	19520
$[Gd(mphpd)_3]_n$	23400	20800
$Gd(mbphpd)_3$	22360	19960
$[Gd(mbphpd)_3]_n$	23580	21300

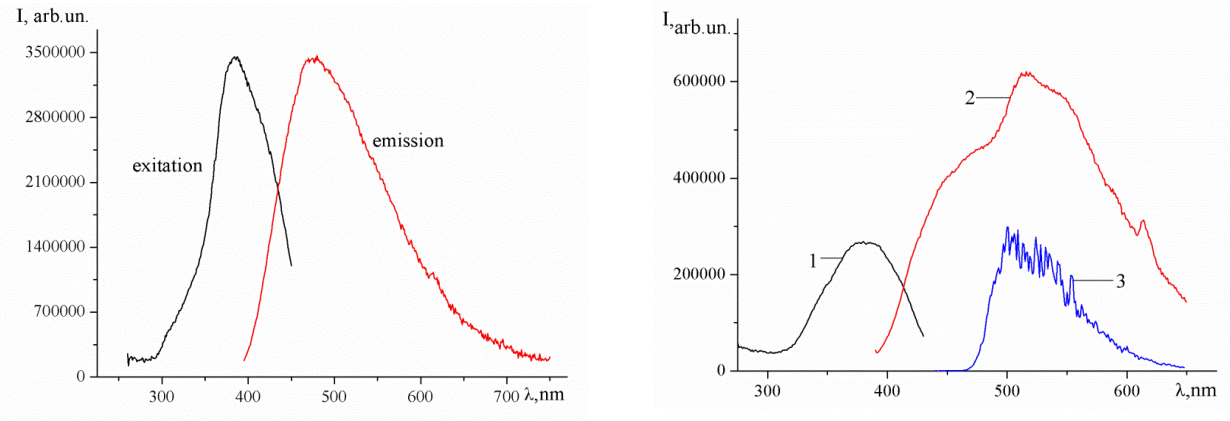

Fig. 7. Exitation ($\lambda_{em.}$ = 453 nm (1) and emission at 293K (2) $[Gd(mphpd)_3]_n$ ($\lambda_{ex.}$ = 380 nm) (a) and 77K (3) of $Gd(mbphpd)_3$ (b) (CHCl3, $\lambda_{ex.}$ = 380 nm).

Considering the close energies of the triplet levels of the ligand systems and the resonance level of Dy^{3+} (21000 cm^{-1}), low emission characteristics should be expected. The recorded emission spectra confirm this assumption. As can be seen from Fig. 8b, the intrinsic luminescence intensity of the ligand is rather high and is observed in the visible region of the spectrum next to the characteristic emission band of dysprosium.

Taking into account the excitation spectrum (Fig. 8a), it is advisable to record the emission spectra with exciting different wavelengths. As can be seen from Fig. 8b, upon ex-

citation at a wavelength of 375 nm, a broad band is present in the emission spectrum, which corresponds to the intrinsic emission of the ligand. At λ = 329 nm, we observe a decrease in the emission of the ligand, but the appearance of emission bands of the dysprosium ion. For the Dy^{3+} ion, the characteristic emission c transitions $^4F_{5/2} \rightarrow {}^6H_{J/2}$; J = 9, 11, 13, 15. So with a maximum (λ_{em} = 479–482 nm corresponds to $^4F_9 \rightarrow {}^6H_{15/2}$ magnetic dipole transition and the band λ_{em} = 572–574 nm (yellow-light) is characteristic of $^4F_9 \rightarrow {}^6H_{13/2}$ electric dipole transition. Thus, the excitation wavelength has a significant effect on the emission characteristics of metal complexes. In this regard, it is necessary to choose the correct excitation wavelength, which will reduce the luminescence intensity of the ligand and increase the metal complex. Unfortunately, for monomeric complexes with both ligands, the emission spectra could not be recorded for high ligand fluorescence.

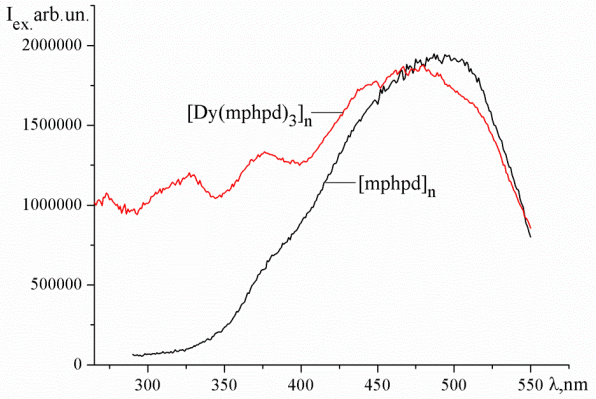

Fig. 8a. Exitation spectra of polymers (ligand and complexes).

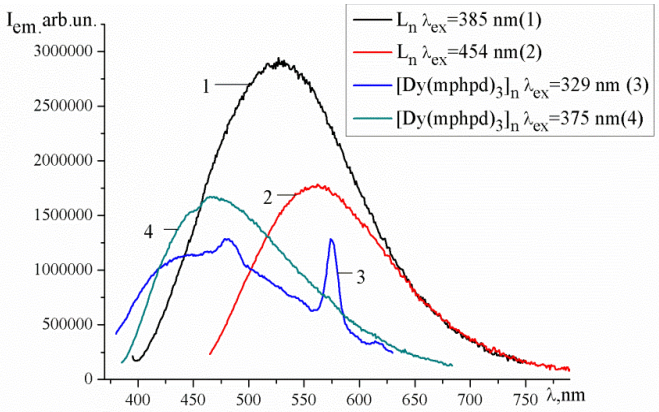

Fig. 8b. Emission spectra of polymer ligand and complexes at other exatation.

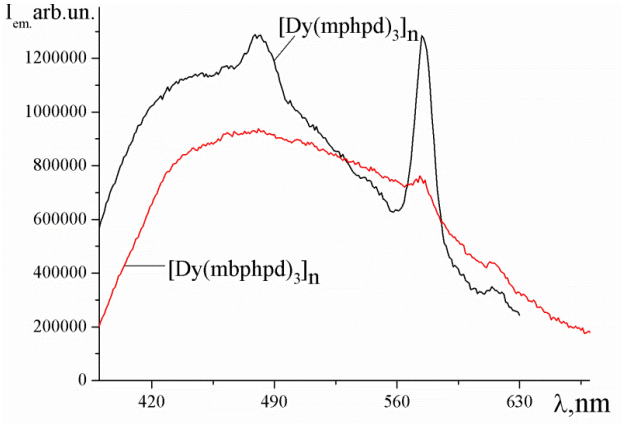

Fig. 8c. Emission spectra of complexes λ_{ex}= 329 нм ($[Dy(mphpd)_3]_n$) $\lambda_{ex.}$=355 нм ($[Dy(mbphpd)_3]_n$).

Comparing the emission spectra of metalopolymers with various ligands in Fig. 8c, it can be seen that the introduction of large aryl substituents probably has a negative effect on the emission characteristics of the compounds. Through the shielding of the emitting centers, and a low energy gap between the levels.

It is known that by changing the particle size or surface morphology, one can completely change their properties, which makes it possible to obtain systems of a given composition with predictable properties. A change in the

dispersion can also have affect on the luminescent characteristics of the complexes. The method of dynamic light scattering makes it possible to establish the dispersion and stability of dispersed systems in solution. The method of dynamic light scattering was used to determine the particle size of complexes dissolved in dimethylformamide at 25 °C with Zeta Sizer Malvern. The studies carried out have shown that the obtained systems are rough polydisperse systems, the reproducibility of the results is low. Micrographs were recorded to establish the surface morphology. Microphotographs were recorded on a scanning electron microscope (SEM) Tescan Mira 3. For polymer complexes, as in most cases, the characteristic larger particle size is due to agglomeration. When passing from a monomeric to a polymer sample, the surface morphology remains unchanged, the structure is layered. The surface structure of monomeric complexes is not uniform, which indicates the presence of agglomerated particles, and, as a consequence, an increase in the size of individual groups. In general, photomicrographs of test samples are similar to those previously described.

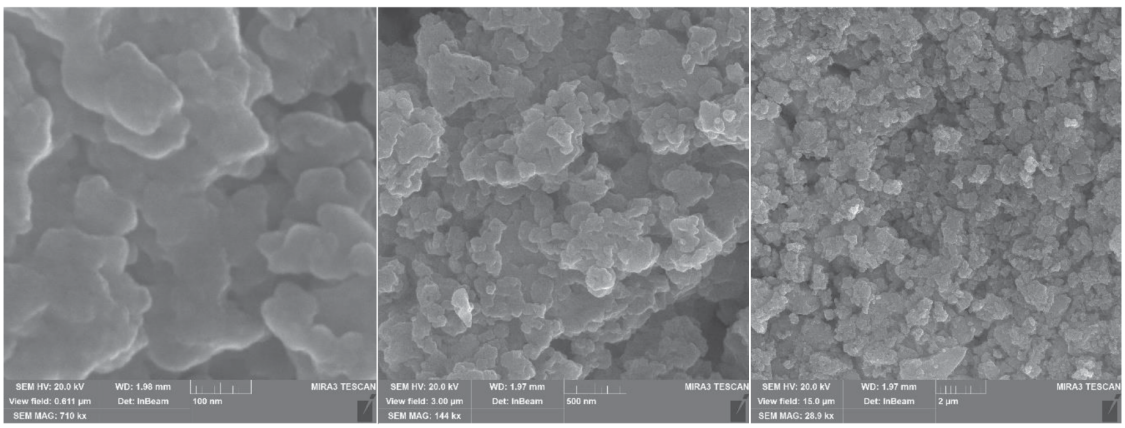

a

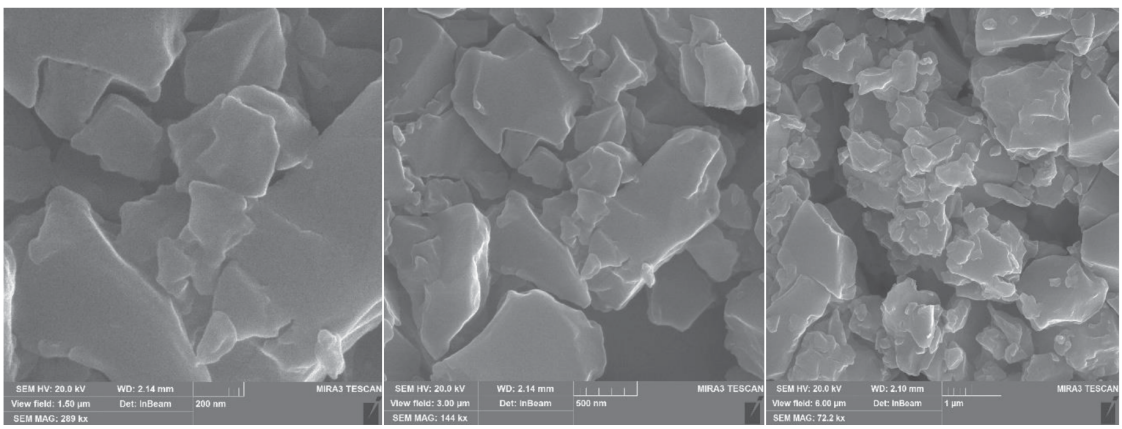

b

Fig. 9. SEM microphoto of the povders $Gd(mbphpd)_3$ (a), $[Gd(mbphpd)_3]_n$ (b) scale label 100nm, 500nm, 2 micron, 1 micron.

Conclusion

It was established the hydration composition, the structure and symmetry of the nearest coordination environment of the central atom in coordination compounds GD (III) and Dy(III) with β-diketones. The spectral-luminescent characteristics of obtained mono- and poly dysprosium complexes exhibit a low luminescence intensity in the visible region of the spectrum, connected with close energies the triplet level of the ligand, and the singlet level of the emitting ion. It is shown that at different excitation wavelengths presence different emission characteristics. The resulting systems are coarsely dispersed amorphous powders with a layered structure.

Acknowledgments

This work was supported by funding from the National Academy of Sciences of Ukraine (318 E – program), «Creation of new multifunctional nanomaterials based on coordination compounds of 3d-metals and lanthanides with O, N-donor ligands».

The authors are grateful to Professor Irina Savchenko of the Macromolecular Chemistry Department of the Faculty of Chemistry of the National Taras Shevchenko University of Kyiv for help in the synthesis of metal polymers.

КООРДИНАЦІЙНІ СПОЛУКИ GD^{3+} ТА DY^{3+} З ДЕЯКИМИ β-ДИКЕТОНАМИ

О. С. Бережницька, А. Е. Горбенко, О. О. Роговцов, С. С. Смола, Я. В. Федоров, О. Е. Чигиринець, О. К. Трунова

[1]Інститут загальної та неорганічної хімії ім. В. І. Вернадського НАН України, просп. Академіка Палладіна, 32/34, Київ 03142, Україна

[2]Національний технічний університет України "Київський політехнічний інститут імені Ігоря Сікорського", просп. Перемоги, 37, Київ 03056, Україна

[3]Фізико-хімічний Інститут імені О. В. Богатського НАН України, вул. Люстдорфська дорога, 86, Одеса 65080, Україна

Синтезовано нові комплекси Dy(III) та Gd(III) з β-дикетонами, що містять ненасичені та арильні замісники. Виконано квантово-хімічні розрахунки молекул лігандів і металокомплексів. Розраховано основні енергетичні характеристики молекул лігандів: ентальпія утворення, повна енергія молекули та довжини зв'язків, параметри електронної заселеності лігандів. Розраховані енергії вищої заповненої молекулярної орбіталі (E_{HOMO}) і нижчої вакантної молекулярної орбіталі (E_{LUMO}) свідчать про слабкі електроноакцепторні властивості комплексів.

Методом радикальної полімеризації отримано металополімери на основі синтезованих комплексів. Встановлено склад та будову синтезованих комплексів та металополімерів. Показано, що при полімеризації

координаційне оточення центрального іона залишається незмінним. Ліганди координуються до центральних іонів бідентатно-хелатно, утворюючи трис-комплекси. К.ч. іонів гадолінію (III) та диспрозію (III) дорівнює 8, координаційна сфера доповнюється двома молекулами води. Досліджено спектрально-люмінесцентні характеристики синтезованих сполук. Визначено енергії триплетного рівня мономерних та полімерних лігандів. Наявність молекул води в найближчому координаційному оточенні зумовлює низьку інтенсивність емісії мономерних комплексів диспрозію. В спектрах люмінесценції металополімерів присутні смуги magnetic dipole transition ($^4F_9 \rightarrow {}^6H_{15/2}$) and electric dipole transition ($^4F_9 \rightarrow {}^6H_{13/2}$). Близькі енергії триплетного рівня ліганду та резонансного рівня іона диспрозію зумовлюють невисокі емісійні характеристики синтезованих комплексів диспрозію. Дослідження морфології та дисперсності наносистемы, отриманих на основі синтезованих сполук, свідчить про великий розмір часток та полідисперсність, що зумовлено наявністю громіздких замісників та агломерації. Структура поверхні частинок є шаруватою.

Ключові слова: лантаніди, комплекси, люмінесцентні властивості, металополімери, гадоліній, диспрозій, β-дикетони.

REFERENCES

1. Santos P.R.S., Pereira D.K.S., Costa I.F., Silva I.F., Brito H.F., Faustino W.M., Carneiro Neto A.N., Moura Jr. R.T., Araújo M.H., Diniz R., Malta O.L., Teotonio E.E.S., Experimental and theoretical investigations of the [Ln(β-dik) $(NO_3)_2(phen)_2]\cdot H_2O$ luminescent complexes, *Journal of Luminescence*. 2020. doi: https://doi.org/10.1016/j.jlumin.2020.117455.
2. Mikhalyova E.A., Zeller M., Jasinski J.P. at all Combination of single-molecule magnet behaviour and luminescence properties in a new series of lanthanide complexes with tris(pyrazolyl)borate and oligo(β-diketonate) ligands. *Dalton Transactions*. 2020. **49**(23): 7774–7789.
3. Dascalu I.A, Mikhalyova E.A., Shova S., Lozan V., Roman G. at all. Synthesis, crystal structure and luminescent properties of isoreticular lanthanide–organic frameworks based on a tetramethyl-substituted terphenyldicarboxylic acid *Polyhedron*. 2021. **194:** 114929.
4. Sukhikh T.S., Kolybalov D.S., Pylova E.K., Bashirov D.A., Komarov V.Y., Kuratieva N.V., Smolentsev A.I.,Fitch A.N., Konchenko S.N. A fresh look at the structural diversity of dibenzoylmethanide complexes of lanthanides. *New J. Chem.* 2019. **43**: 9934–9942. doi: 10.1039/C9NJ02059D.
5. Abdallah. A., Freslon S., Fan X., Rojo A., Daiguebonne C., et al. Lanthanide-Based Coordination Polymers With 1,4-Carboxyphenylboronic Ligand: Multiemissive Compounds for Multisensitive Luminescent Thermometric Probes. Inorganic Chemistry, *American Chemical Society*.

2019. **58**(1): 462–475. ff10.1021/acs.inorgchem.8b02681.

6. Zhang J., Li J., Feng X., Kong M., Hu Z.-B., Zheng Y.-X., Song Y. Light-controlled efficient photoluminescence based on an europium b-diketonate complex with single-crystal-to-single-crystal [2+2] cycloaddition. *Chem. Commun.* 2019. **55:** 12873–12876. doi: 10.1039/c9cc05227e.
7. Kumar K., Stefańczyk O., Chorazy S., K. Nakabayashi, B. Sieklucka, S. Ohkoshi Effect of Noble Metals on Luminescence and Single-Molecule Magnet Behavior in the Cyanido-Bridged Ln–Ag and Ln–Au (Ln = Dy, Yb, Er). *Complexes Inorg. Chem.* 2019. **58**(9): 5677–5687. https://doi.org/10.1021/acs.inorgchem.8b03634.
8. Yao X., An G., Li Y., Yan P., Li W., Li G. Effect of nuclearity and symmetry on the single-molecule magnets behavior of seven-coordinated ***β***-diketonate Dy(III) complexes. *Journal of Solid State Chemistry.* **274:** 259–302. https://doi.org/10.1016/j.jssc.2019.03.044.
9. Shi, Q.-H.**,** Xue C.-L., Fan C.-J., Yan L.-L., Qiao N., Fang M., Wang S.-F., ***M***agnetic refrigeration property and slow magnetic relaxation behavior of five dinuclear Ln(III)-based compounds. *Polyhedron.* 2021. **194:** 114938. https://doi.org/10.1016/j.poly.2020.114938.
10. Fondo M., Corredoira-Vázquez J., Herrera-Lanzós A., García-Deibe A.M., Sanmartín-Matalobos J., Manuel Herrera J., Colacio E., Nuñeza C. Improving the SMM and luminescence properties of lanthanide complexes with LnO_9 ***cores in the presence of*** Zn^{II}: an emissive Zn_2Dy single ion magnet. *Dalton Trans.* 2017. **46**: 17000–17009.
11. Pavlishchuk V.V. Influence of Structure on Magnetic and Photoluminescent Properties of Coordination Compounds of 3d- and 4f-Metals and Nanocomposites Based on Them. *Theoretical and Experimental Chemistry*. 2017. 53(5): 296–304.
12. Eliseeva S.V., Bunzli J.C.G. Lanthanide luminescence for functional materials and bio-sciences. *Chemical Society Reviews*. **39**(1): 189–227.
13. Fouad R., El-Shafiy H.F., Photoluminescence and cytotoxicity properties of new quinolinone lanthanide nano-complexes, *Journal of Molecular Structure*. 2019. **1190:** 68–76. doi: https:// doi.org/10.1016/j.molstruc.2019.04.051.
14. Sato T., Higuchi M. Efficient white-light-emission from a heterometallo-supramolecular polymer with Eu(III) and Zn(II) ions introduced alternately. *Tetrahedron Letters.* **60**(13): 940–943. https://doi.org/10.1016/j.tetlet.2019.02.044
15. Shia Q., Liub J., Wanga J., Yanga X., Zhanga X., Lia S., Suna P., Chena J., Lia B., Lüb X., Color-tunable white-light of binary tris-***β***-diketonate-(Dy3+, Gd3+ x) complexes' blend under single wavelength excitation. *Inorganic Chemistry Communications*. 2020. **113:** 107814. https://doi.org/10.1016/j.inoche.2020.107814
16. Wang L.P., Du H.Y., Wang Y.X., Wang M., Tian Z.L., White-light-emitting single component metal-organic frameworks based on 2,3-pyridinedicarboxylic acid, *Integr. Ferroelectr*. 200 (2019): 199–227.
17. Wei C., Yao X., Sun B., Cai Z., Zhao Z., Chen M., Wei H., Liu Z., Bian Z., Huang C., Evaporable luminescent lanthanide complexes based on novel tridentate ligand. *Journal of Rare Earths*. 2021. **35**(1): 7–14. https://doi.org/10.1016/S1002-0721(16)60166-7.

18. Nikolaeva A., Nygaard R., Martynova I., Tsymbarenko D. Synthesis, structure and thermal behavior of volatile mononuclear mixed ligand complexes of rare-earth dipivaloylmethanates with diethylenetriamine. *Polyhedron*. 2020. **180:** 114373, https://doi.org/10.1016/j.poly.2020.114373.
19. Laura A. G., Wada, Lee S.C., Sobolev A.N., Hasegawa Yu., ,Eli Z.-C., Massi O. M., at all. Photophysical investigation of near infrared emitting lanthanoid complexes incorporating tris(2-naphthoyl)methane as a new antenna ligand. *Dalton Transactions*. 2019. 48: 3768–3776. 10.1039/C8DT04749A.
20. Meshkova S. B., The Dependence of the Luminescence Intensity of Lanthanide Complexes with β-Diketones on the Ligand Form, *J. of Fluorescence.* 2000. 10: 333–337. https://doi.org/10.1023/A:1009418227641/.
21. Gontcharenko V. E., Kiskin M.A., Dolzhenko V. D., Korshunov V.M., Taydakov I.V., Belousov Y.A. Mono- and Mixed Metal Complexes of Eu^{3+}, Gd^{3+}, and Tb^{3+} with a Diketone, Bearing Pyrazole Moiety and CHF2-Group: Structure, Color Tuning, and Kinetics of Energy Transfer between Lanthanide Ions. *Molecules*. 2021. **26**: 2655–2669. https://doi.org/10.3390/molecules26092655.
22. Pan M., Du B.B., Zhu Y.X., Yue M.Q., Wei Z.W., Su C.Y., Highly efficient visible-toNIR luminescence of lanthanide(III) complexes with zwitterionic ligands bearing charge-transfer character: beyond triplet sensitization. Chem. Eur. J. 2016. **22**: 2440–2451.
23. Olyshevets I., Kariaka N., Znovjyak K., Gerasimchuk N., Lindeman S., Smola S., Seredyuk M., Sliva T., Amirkhanov V., Synthesis and Characterization of Anionic Lanthanide(III) Complexes with a Bidentate Sulfonylamidophosphate (SAPh) Ligand, *Inorg. Chem*. 2020. **59**(1): 76–85. https://doi.org/10.1021/acs.inorgchem.8b02846.
24. Litsis O., Ovchynnikov V., Sliva T., Amirkhanov V., Sorokin V., Minyailo M., Kolomzarov Yu., Tytarenko P., Minakova I., Europium coordination compounds based on carbacylamidophosphate ligands for metal-organic light-emitting diodes (MOLEDs), *Semicond. Phys. Quantum Electron. Optoelectron*. 2013. **16**(2): 210–215. https://doi.org/10.15407/spqeo16.02.210.
25. Savchenko I.O., Berezhnytska O.S., Fedorov Ya., New polymer metal complexes based β-diketones and lanthanides for OLEDs In book: Chem. Engineering of Pol. Product. of Func. and Flexible Mater., Apple Academic Press.19. 2017. 40-51 https://doi.org/10.1201/9781315365985.
26. Berezhnytska O., Savchenko I., Denysova Z., Rusakova, N., Fedorov, Ya., Veligura, L., Rogovtsov, O.,Trunova, E. The new nanosized system on the basis Eu(III) complexes as precursors for organic electroluminescence diodes. *Molecular Crystals and Liquid Crystals*. 2014. **590:** 58–65. https://doi.org/10.1080/15421406.2013.873848.
27. Igoa F., Peinado G., Suescun L., Kremer C., Torres J., Design of a white-light material based on a mixed-lanthanide metal organic framework, *J. Solid State Chem*. 279 (2019): 120925.
28. Li J.J., Fan T.T., Qu X.L., Han H.L., Li X., Temperature-induced 1D lanthanide polymeric frameworks based Ln_n (n = 2, 2, 2, 6)

cores: synthesis, crystal structures and luminescent properties. *Dalton Trans.* 2016. **45:** 2924–2935.
29. Fan L.M., Fan W.L., Li B., Zhao X., Zhang X.T., W-shaped 1,3-di(2,4-dicarboxyphenyl)benzenebased lanthanide coordination polymers with tunable white light emission, *New J. Chem.* 2016. **40:** 10440–10446.
30. Dang S., Zhang J.H., Sun Z.M., Tunable emission based on lanthanide(III) metalorganic frameworks: an alternative approach to white light. 2012. *J. Mater. Chem.* **22:** 8868–8873.
31. Tweedle M.F. Physicochemical properties of gadoteridol and other magnetic resonance contrast agents. Invest Radiol. 1992. **27:** 2–6.
32. Runge V.M. A comparison of two MR hepatobiliary gadolinium chelates, Gd-BOPTA and Gd-EOB-DTPA. *Journal of Computer Assisted Tomography*. 1998. **22:** 643–650.
33. Tweedle M.F. The ProHance story: the making of a novel MRI contrast agent. *European Radiology*. 1997. **7:** 225–230.
34. Raymond K.N, Pierre V.C. Next generation, high relaxivity gadolinium MRI agents. *Bioconjug Chem.* 2005. **16:** 3–8.
35. Runge V.M, Dickey K.M, Williams N.M, Peng X. Local tissue toxicity in response to extravascular extravasation of magnetic resonance contrast media. *Invest Radiol.* 2002. **37:** 393–398.
36. Xu, Q. Gadolinium(III) chelated conjugated polymer as a potential MRI contrast agent / Q. Xu, L. Zhu, M. Yu, F. Feng, L. An, C. Xing, S. Wang Polymer. 2010. 51(6): 1336–1340.
37. Liu, Y. Gadolinium-loaded polymeric nanoparticles modified with Anti-VEGF as multifunctional MRI contrast agents for the diagnosis of liver cancer / Y. Liu, Z. Chen, C. Liu, D. Yu, Z. Lu, N. Zhang Biomaterials. 2011. 32(22): 5167–5176.
38. Savchenko I., Berezhnytska O.S., Fedorov Ya, Smola S., Trunova O. Luminescent properties of new polymer metal complexes based β-diketones and REE. *Molecular Crystals and Liquid Crystals*. 2018. **673**(1): 48–60. https://doi.org/10.1080/15421406.2019.1578493.
39. Berezhnytska O.S., Savchenko I.O., Ivakha N.B., Trunova O.K., Smola S.S., Zheleznova L.I. Near infrared electroluminescence polymeric systems containing β-diketones and lanthanides as emitters for organic light – emitting diodes. *Molecular Crystals and Liquid Crystals*, 2018. **670**(1): 48–60. https://doi.org/10.1080/15421406.2018.1542061.
40. Fedorov Ya.V., Berezhnytska O.S., Trunova O. K., Melnyk O.V., Synthes and study of europium complexes and metalopolymers based on. *Ukr. Khim. Journal.* 2013. **79**(3): 25–31.
41. Mishchenko A.M., Trunova O.K., Semiempirical calculation of the structure of tautomeric forms of aliphatic β-ketoesters. Ukr. Khim. J. 81(10): 73–80.
42. Mishchenko A.M., Trunova, E.K., Berezhnytska A.S., Lanthanide complexes with allyl acetoacetate in mixed water-organic media: Formation, stability and bonding. *Journal of Solution Chemistry*. 2015. **44**(11): 2117–2128. https://doi.org/10.1007/s10953-015-0396-z.
43. Movchan, T.I., Solovyov, T.I., Petrova, L.A., Voloshanovsky, I.S., Belov, G.P., Pomoghailo A.D. *Izv. AN, Ser. Chem*. 1994. 1: 43–47.

44. I. Savchenko, A. Berezhnytska, E. Trunova, N. Rusakova, Ya. Fedorov, G. Grozduyk Poly complexes based unsaturated ***β***-diketones and rare earth elements for optoelectronics. *Molec. Crys. Liqud.* 2016. **640**. http://dx.doi.org/10.1080/15421406.2016.1257311.
45. Nakamoto K., Infrared spectroscopy of inorganic and coordination compounds. Mir. Moscow. 1991.
46. Nekhoroshkov V.P., Kamalov G.L., Zheltvay I.I., Ososkov A.K., Berestetskaya E.D., On the interaction between the IR spectral properties of 3d-transition metal β-diketonates and their structure. *Russ. J.Coord. Chim*. 1984. **10**(4): 459–465.
47. Nakamoto K., McCarthy P. J., Martell A. E., Infrared Spectra of Metal Chelate Compounds. III. Infrared Spectra of Acetylacetonates of Divalent Metals. *J. Am. Chem. Soc.* 1961. **83**(6): 1272–1276. https://doi.org/10.1021/ja01467a003

Стаття надійшла 01.07.2021.